Band Gap and Symmetry of Wurtzite GaAs

A Resonant Raman Study

Im Fachbereich Physik der
Freien Universität Berlin
eingereichte

Dissertation

von

Patryk Kusch

Berlin, im April 2014

1. Gutachter: Prof. Dr. Stephanie Reich

2. Gutachter: Prof. Dr. Katharina Franke

Tag der Einreichung: 01.04.2014

Tag der Disputation: 08.05.2014

Für meine geliebte Frau
und meine beiden wundervollen Kinder.
Ohne Euch würde es diese Arbeit nicht geben

"Ein Gelehrter in seinem Laboratorium ist nicht nur ein Techniker;
er steht auch vor den Naturgesetzen wie ein Kind vor der
Märchenwelt." (Marie Curie)
Oder mit meinen Worten:
Ein Wissenschaftler im Labor
ist wie ein Kind im Spielwarenladen:
Er blickt zum Tellerrand
und geht einfach einen Schritt weiter.

Eidesstattliche Erklärung

Hiermit versichere ich, die vorliegende Arbeit selbstständig und unter ausschlielicher Verwendung der angegebenen Literatur und Hilfsmittel erstellt zu haben.

Die Arbeit wurde bisher in gleicher oder ähnlicher Form zu keinem anderem Promotionsverfahren vorgelegt und auch nicht veröffentlicht.

Berlin, May 13, 2014 .....

Patryk Kusch

Abstract

III-V nanowires are fascinating quasi one-dimensional crystals, which have a huge potential as optoelectronic devices. Typically they grew in the zincblende structure. But a peculiarity of these nanowires is that they exhibit, depending of the growth conditions, also the wurtzite structure. For wurtzite GaAs up to date the optical gap is a topic of discussion. We perform polarization and position dependent as well as resonant Raman scattering on GaAs nanowires in order to investigate the optical gap of wurtzite GaAs. Resonant Raman scattering is non-destructive. It is directly related to the electronic transitions; thus it is a good alternative to photoluminescence to investigate the optical gap of wurtzite GaAs. Additionally, the comparison of Raman resonance and photoluminescence peaks allows to differentiate between direct and indirect band transitions. The measurements were performed on pure wurtzite, pure zincblende and on wurtzite nanowires with isolated zincblende insertions. The resonances of the TO, LO and 2LO phonon modes show consistently that the optical gap of wurtzite GaAs is $E_0^{WZ} = 1.460\,\mathrm{eV} \pm 3\,\mathrm{meV}$ at room-temperature, $35 \pm 3\,\mathrm{meV}$ larger than the GaAs zincblende band gap. Due to different scattering geometries (parallel and perpendicular to wire axis), we were able to show, that the uppermost valence band has Γ_9 and the lowest conduction band Γ_7 symmetry in wurtzite GaAs. In the wurtzite structure, GaAs exhibits a splitting between the heavy and light hole band at the Γ point. The splitting between both bands is 65 meV. The resonance measurements on wurtzite GaAs with zincblende insertion point out that the wurtzite/zincblende heterostructure has a type-II band alignment. Thus, the zincblende insertions form quantum wells for electrons in the conduction band. This explains the observation of different

transition energies energies in optical measurements.
The E_2^h phonon, which is usually used as a fingerprint of the wurtzite structure, is almost complete quenched at excitation wavelengths above 600 nm. The dielectric polarization contrast for the coupling of light into the wire explains this observation and demonstrates the limits of Raman scattering.
The polarization dependent measurements show that the nanowire do not follow the calculated Raman selection rules. This is a result of the nanowire geometry, especially the wire diameter, and of the dielectric mismatch with the environment.

Zusammenfassung

III-V Nanodrähte sind faszinierende quasi ein dimensionale Krystalle, welche besonders für die Optoelektronik interessant sind. Die Drähte haben normalerweise eine zinkblende Struktur. Jedoch können diese, abhängig von den Wachstumsbedingungen auch eine wurzit Struktur aufweisen. Bei GaAs, welches eine wurzit Struktur zeigt, wird die Energie der Badlücke bis heute diskutiert. In dieser Arbeit wurde polarisations- und positionsabhängige, sowie resonante Raman Streuung gemessen. Die Messungen wurden an reinem zinkblende, reinem wurzit, sowie an wurzit Nanodrähten mit zinkblende Einschlüssen durchgefürt, um die Bandlücke von GaAs in der wurzit Struktur zu bestimmen. Die Resonanzen der TO, LO und 2LO Phononen zeigen klar, dass die Bandlücke von wurzit GaAs $E_0^{WZ} = 1.460\,\text{eV} \pm 3\,\text{meV}$ bei Raumtemperatur ist. Damit ist die Bandlücke von wurzit GaAs $35 \pm 3\,\text{meV}$ größer als die Bandlücke von GaAs in der zinkblende Strukutur. Durch die Wahl einer bestimmten Streugeometrie wird gezeigen, dass das oberste Valenzband eine Γ_9 und das unterste Leitungsband eine Γ_7 Symmetrie hat. Außerdem haben die Messungen ergeben, dass sich das oberste Valenzband in ein Γ_9 und ein Γ_7 aufspaltet. Der Energieunterschied zwischen beiden Bändern ist 65 meV.

Die Resonanzen, gemessen an den wurzit Drähten mit zinkblende Einschlüssen, weisen darauf hin, dass die wurzit/zinkblende Heterostruktur ein Typ-II Heteroübergang bildet. Damit bilden die zinkblende Einschlüsse Quantentöpfe für Elektronen im Leitungsband. Dies erklärt die Beobachtung von verschiedenen Bandlücken bei optischen Messungen an GaAs Nanodrähten. Die Messungen an dem für wurzit GaAs charachteristischem E_2^h Phonon haben gezeigt, dass es ab

einer Anregungswellenlänge von 600 nm, fast völlig verschwunden ist. Dies lässt sich durch den dielektrischen Kontrast und damit durch die Einkopplung von Licht in den Draht erklären und zeigt zusätzlich die Grenzen der Raman Spektroskopie. Die polarisationsabhängigen Messungen haben ergeben, dass die Nanodrähte nicht den Raman Auswahlregeln folgen. Dies ergibt sich aus dem kleinen ($50 - 200$ nm) Durchmesser der Drähte und dem verändertem dielektrischen Verhältnis zwischen Draht und Umgebung.

Abbreviations

AFM	Atomic force microscopy
BS	beam splitter
CCD	Charged coupled device
cw	continuous wave
FR	Fresnel rhomb
GaAs	Gallium arsenide
LBO	Lithium Triborate
LO	longitudinal optical
MBE	Molecular beam epitaxy
NW	Nanowire
PL	Photoluminescence
QW	Quantum well
RRS	Resonant Raman scattering
SEM	Scanning electron microscopy
SF	Stacking fault
SHG	Second harmonic generation
SO	Spin orbit
TE	transverse electric
TEM	Transmission electron microscopy
Ti:Sa	Titan : Sapphire
TM	transverse magnetic
TO	transversal optical
VLS	Vapour-liquid-solid
WZ	Wurtzite
ZB	Zincblende

Contents

1 | Introduction

In the recent years semiconducting nanowires have become highly interesting in the field of nanotechnology [1–5]. Nanowires are quasi-one-dimensional crystals with well defined diameters. Depending on the growth conditions [6] the diameters can vary from a few to several tens of nanometers. Nanowires have a huge potential for many different applications. They can be used as light emitting diodes, photodetectors and other optoelectronic devices [7–9]. Moreover, the low electron mass in GaAs and the high-quality GaAs/(Al,Ga)As interface allow to produce high performance electronic devices, e.g. high electron mobility transistor (HEMT) [10].
Another very interesting point is that nanowires are promising candidates to replace Silicon (Si) in integrated circuits. To this day integrated circuits, solar cells and diodes are mainly based on Si. Si crystals have a lot of advantages; they can be produced with high purity, in very large diameter boules and at low cost. However, silicon has one main disadvantage its indirect bandgap, which results in very weak light emission. In addition the miniaturization of Si-based integrated circuits leads to problems with heat transportation, which prevent the production of smaller and faster electronic devices.
Nanowires may posses varying crystal phase along the wire axis. Such semiconductors as GaAs, Si, InAs, GaP, AlAs etc. typically crystallize in the zincblende structure. Due to the lower surface energy of the wurtzite phase and the large surface-to-volume ratio of nanostructures, nanowires may show a pure wurtzite, a pure zincblende, or a mixture of zincblende and wurtzite phase [11–13]. Changing the crystal structure from cubic (zincblende) to hexagonal (wurtzite) along the wire axis gives the possibility of band structure engineering. As wurtzite nanowires show

a different band gap than zincblende nanowires, an island of zincblende (wurtzite) in a wurtzite (zincblende) nanowire, will enable the longtime storage of electrons (holes). In order to realize such nanowire-based devices, we have to understand the electronic properties of the nanowires, in particular the size and nature of the band gap, which depends on the crystal structure. In this work we concentrate on the investigation of GaAs nanowires.

GaAs crystallize in the zincblende structure. The band gap of zincblende GaAs is 1.425 eV at room-temperature. The optical gap of wurtzite GaAs is controversial and a topic of discussion. Only the knowledge of the optical gap and the band structure of wurtzite nanowires allows to progress new nanowire-based devices in the field of optics, electronics and biological sensing [14]. Currently a large fraction of available studies place the wurtzite gap up to 20 meV below the gap of zincblende GaAs [15–18], while another fraction reported the wurtzite gap up to 55 meV larger than the gap in the zincblende structure [19–25]. The published findings observed in various experiments together with theoretical predictions from ab-initio and semiempirical calculations are summarized in Tab. 1.1.

We use resonant Raman scattering applied with photoluminescence experiments on pure wurtzite and zincblende GaAs nanowires to determine the optical gap of wurtzite GaAs. Resonant Raman scattering is a non-destructive tool, directly related to the electronic states and allows to derive the band gap energy of wurtzite GaAs. Choosing appropriate polarization conditions and excitation energies allows a consistent assignment of the optically active transitions in wurtzite GaAs. Additionally, resonant Raman experiments with incoming light polarized perpendicular and parallel to the wire axis enables to study the splitting between the heavy and light hole band at the Γ point of wurtzite GaAs [26].

In order to find an explanation for the varying gap energies in wurtzite GaAs obtained by optical experiments, e.g. photoluminescence and resonant Raman scattering, we perform resonant Raman scattering and photoluminescence experiments on wurtzite GaAs nanowires with zincblende insertions. The combination of PL and position dependent resonant Raman scattering allow us to investigate the type of the band alignment for a wurtzite/zincblende heterostructure. In a type II band alignment for example, luminescence originates mainly from indirect band-to-band transitions. Raman resonances, in contrast, occur only for direct

Table 1.1 Experimental and theoretical reported bandgap energies of wurtzite GaAs by different authors. For comparison: the bandgap of zincblende GaAs is 1.519 eV at 0 K and 1.425 eV at room temperature

YEAR	**EXPERIMENTAL**	**LARGER GAP**	**WURTZITE GAP (eV)**	**TEMP. (K)**
2013	Kim *et al.* [25]	*equal*	1.451	5
2013	Kim *et al.* [25]	*wurtzite*	1.44	300
2012	Jahn *et al.* [29]	*wurtzite*	1.47	300
2011	Ketterer *et al.* [26]	*equal*	1.51	5
2011	Heiss *et al.* [15]	*zincblend*	1.50	4.2
2009	Spirkoska *et al.* [19]	*wurtzite*	1.54	10
2009	Moewe *et al.* [16]	*zincblend*	1.51	4
2009	Hoang *et al.* [20]	*wurtzite*	1.54	4
2007	Martelli *et al.* [21]	*(wurtzite)*	1.52	10
2007	Zanolli *et al.* [18]	*zincblend*	1.47	10
	THEORY			
2012	Belabbes *et al.* [30]	*wurtzite*	1.46	
2011	Heiss *et al.* [15]	*zincblend*	1.49	
2010	De *et al.* [17]	*zincblend*	1.50	
2007	Zanolli *et al.* [18]	*wurtzite*	1.57	
1993	Murayama *et al.* [22]	*wurtzite*		

band transitions [27].

With polarization-dependent measurements we study the Raman selection rules of thin zincblende nanowires. Additionally, we investigated the E_2^H phonon and its intensity as a function of the excitation wavelength. In comparison with zincblende GaAs, wurtzite GaAs exhibit an E_2^H phonon [27, 28] Thus, it can be used as a fingerprint of the wurtzite phase in nanowires.

2 | GaAs: From Zincblende to Wurtzite

To determine the band gap of wurtzite GaAs, one has to understand the main differences between the zincblende and wurtzite crystal structure and the resulting differences in the band structure and thus in the electronic properties.

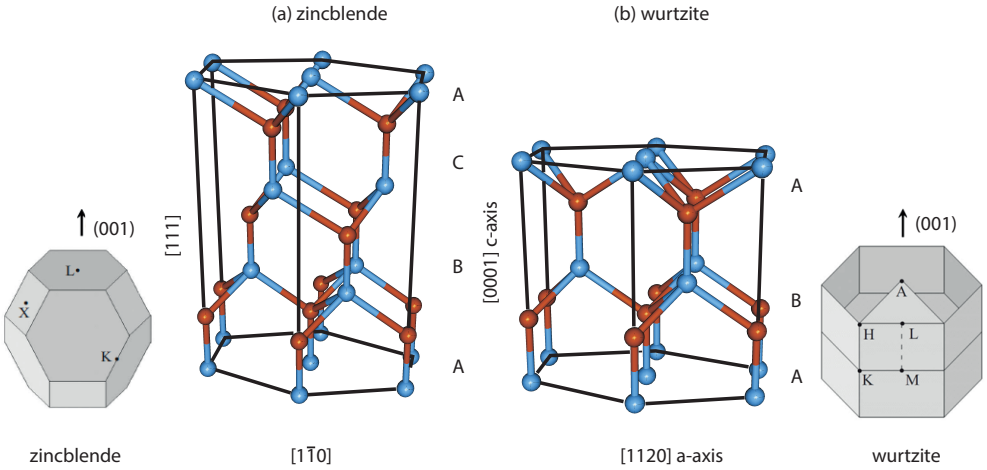

Figure 2.1 Different GaAs crystal structures: (a) 4-fold coordinated zincblende and (b) wurtzite stacking sequence. For clarity the Brillouin zones of the wurtzite and zincblende structure are shown (adapted from Ref. [17]).

GaAs in the zincblende structure is very well known [27, 31]. It is a III-V semiconductor, consisting of gallium (Ga) and arsenic (As). Figure 2.1a show a scheme of zincblende GaAs. The zincblende lattice has two face centered cubic sublattices with the lattice parameter $a = 5.6539\,\text{Å}$ [32, 33]. In bulk form GaAs has a direct bandgap at the Γ point. The bandgap energy is 1.424 eV at room-temperature and 1.519 eV at low-temperature. The valence band has Γ_{15} and the conduction band Γ_1 symmetry [31].
As mentioned before, III-V semiconducting nanowires often crystallize in the wurtzite structure, which is metastable in bulk material [11,32]. Because of the lower surface energy of the wurtzite phase and the large surface-to-volume ratio of nanostructures, GaAs nanowires can show a pure wurtzite, a pure zincblende or a mixture of zincblende and wurtzite phase [11].
The lattice of wurtzite GaAs consists of two hexagonal sublattices with lattice parameters $a = 3.989\,\text{Å}$ and $c = 6.564\,\text{Å}$ [32, 33]. Both crystal structures (zincblende and wurtzite) are displayed in Fig. 2.1. The wurtzite and zincblende structures are 4-fold coordinated. They differ only in their stacking sequence: While zincblende GaAs has an $ABCABC...$ stacking sequence along the cubic [111] axis, wurtzite GaAs has an $ABABAB...$ stacking sequence along the hexagonal [111] axis. Their close similarity results from their geometry, which differs only in the bonding of their third nearest neighbor. Wurtzite GaAs has as zincblende GaAs, a direct bandgap, but its value and the band symmetry at room-temperature are controversially discussed. It is clear that the change of the crystal structure from cubic to hexagonal means a modification in the band symmetry. In the zincblende and wurtzite structure many high-symmetry points in the Brillouin zone are related to each other, because of the similarities of the two crystals. But the wurtzite structure has one main difference: The unit cell in (0001) in wurtzite GaAs is twice the length of the unit cell in the zincblende structure in the equivalent (111) direction. As a result the L point in zincblende is zone-folded to the Γ point in wurtzite in the empty lattice approximation [17].

2.1 Electronic Properties of GaAs

We will now demonstrate the influence of a large unit cell in real space on a band structure in the zone folding approximation. A simple but impressive example is shown for a superlattice consisting of a direct and indirect semiconductor in Fig. 2.2. For simplicity both semiconductors have similar electronic properties and the superlattice consists of monoatomic layers, which are grown layer by layer. In this case the energy band structure is zone-folded at the point $2\Pi/2a$, as shown in Fig. 2.2 (dotted curves). For the indirect semiconductor, the zone folding causes the conduction band minimum of the superlattice to be located at $K = 0$ and therefore to a quasi direct transition [34].

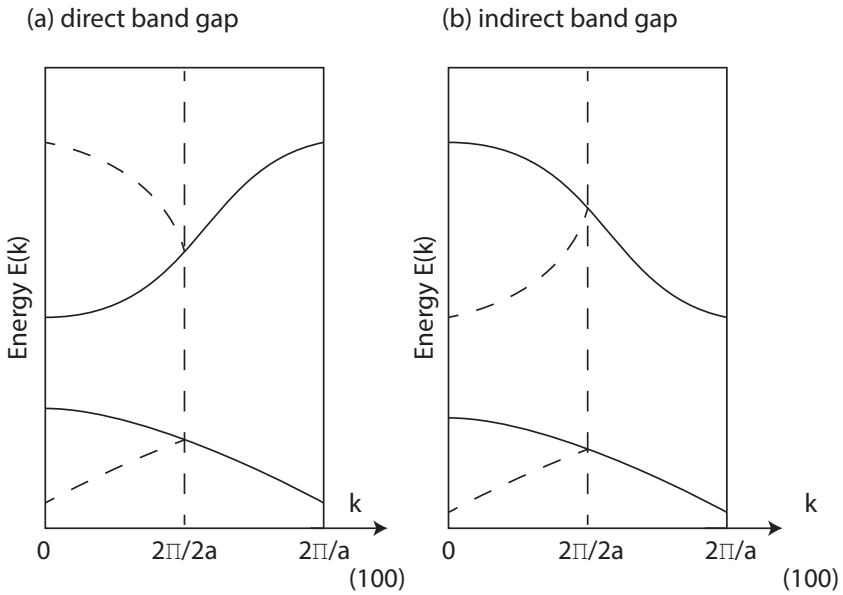

Figure 2.2 Brillouin zone-folding effect in superlattice for a direct (a) and indirect (b) band gap semiconductor, where the dotted curves show zone-folded bands schematically, adapted from Ref. [34]

A prominent example for a superlattice consisting of direct and indirect band gap semiconductors are GaAs and AlAs. AlAs is an indirect band gap semiconductor. Therefore for a GaAs/AlAs supperlatitice, one may expect a quasi direct transition in the superlattice due to zone-folding effect in which the X point of AlAs is folded to the Γ point [34].

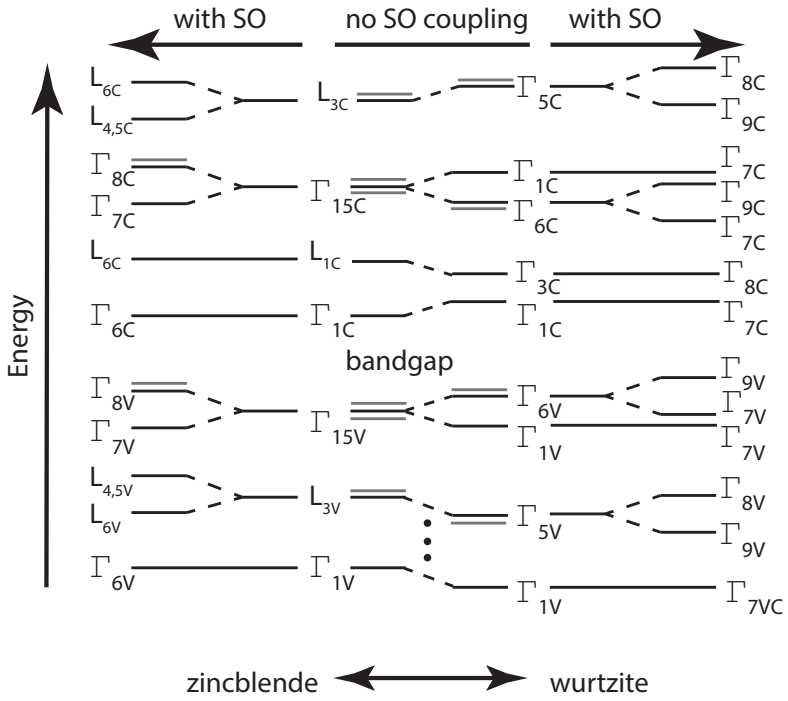

Figure 2.3 Scheme of the predicted correspondence between energy levels at the L and Γ points in zincblende and the Γ point in wurtzite GaAs with and without spin orbit coupling as shown in Ref. [17, 22]. The gray lines represents the degenerated levels.

Coming back to wurtzite GaAs. Here the L point is folded to the Γ point. Additionally, one needs to consider the spin-orbit coupling. The electron spin can be

coupled to the orbital angular momentum via the spin-orbit interaction [31]. Spin-orbit coupling scales with the atomic number and is a relativistic effect. For semiconductor with heavier elements, such as Ga, As, Sb and Ge spin-orbit coupling is significant and has to be included into the calculations of the band structure [31]. As example we use zincblende and wurtzite crystals. For certain individual states in crystal the lacking inversion symmetry, spin-orbit coupling causes a splitting of spin-up and spin-down states. This leads to $E_{\uparrow}(-\boldsymbol{k}) \neq E_{\uparrow}(\boldsymbol{k})$ [17].
The spin splitting for zincblende and wurtzite crystals exist in a particular direction (k_x, k_y or k_z) and can be determined by symmetry considerations [35]. The spin splitting effect is much more prominent in wurtzite than in zincblende crystals, due to the lower wurtzite crystal symmetry [17,36–42], although both crystals lack inversion symmetry. In order to understand the trend of the band structure of both crystal, Fig. 2.3 shows the relationship between the zone-center states for the Γ and L point in wurtzite and zincblende structure with and without spin-orbit coupling [17, 22].

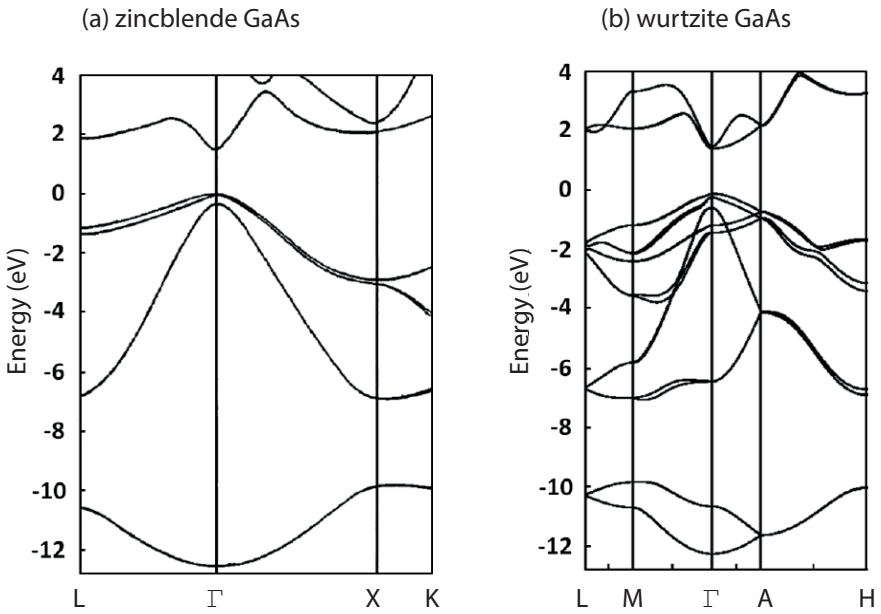

Figure 2.4 Band structure near the Γ point for (a) zincblende (adapted from Ref. [43]) and (b) for wurtzite GaAs (adapted from Ref. [17]).

The comparison of both crystal structures show that Γ_1, L_1 and L_3 states in the zincblende structure corresponds to Γ_1,Γ_3 and Γ_5 in wurtzite. At the top of the valence band in wurtzite GaAs, the hexagonal crystal field splits the p-like Γ_{15} state of zincblende into a fourfolded degenerate Γ_6 and a doubly degenerate Γ_1 state [17]. Taking into account spin-orbit coupling the Γ_{6v} state splits into the Γ_{9v} heavy hole and Γ_{7v} light hole state. As a result all zone-center valence bands in wurtzite belong to either Γ_7, Γ_8 or Γ_9 symmetry [17,44]. Due to zone folding, the conduction band of wurtzite GaAs have besides the Γ_7 state from zincblende a supplementary Γ_8 band [17]. Theoretical predicted values for the splitting energy of both bands are $\Delta_{CB} = -23\,\text{meV}$ [22], $\Delta_{CB} = 87\,\text{meV}$ [15] and $\Delta_{CB} = 85\,\text{meV}$ [17]. The symmetry line $\Lambda(\Gamma \rightarrow L)$ in zincblende is transformed into $\Delta(\Gamma \rightarrow A)$ in wurtzite [17, 45]. The predicted band structure of wurtzite GaAs calculated by De *et al.* is shown in Fig. 2.4(b) [17]. For comparison, Fig. 2.4(a) shows the experimental bandstructure of zincblende GaAs [43]. In Tab. 2.1 the predicted values for the effective masses parallel and perpendicular to the wire c-axis and band energy are given.

Table 2.1 Effective Masses, zone-center states and calculated band energies of wurtzite GaAs (from Ref. [17])

BAND SYMMETRY	**ENERGY (eV)**	$m_\parallel$	$m_\perp$
Γ_9 (heavy hole band)	0.000	0.134	1.026
Γ_7 (light hole band)	-0.120	0.200	0.197
Γ_7 (crystal field split-off band)	-0.475	0.434	0.118
Γ_7 (conduction band)	1.588	0.082	0.090
Γ_8 (conduction band)	1.503	0.125	1.050

2.2 Photoluminescence Experiments

A versatile tool to study the electronic properties of GaAs nanowires are Photoluminescence experiments. Photoluminescence allows to determine directly the band-to-band transition energy. The photoluminescence process is described by three steps (Fig. 2.5):

- **Excitation**: An incident photon excites an electron-hole pair.
- **Thermalization**: The excited electron-hole pair relaxes non-radiative, towards quasi-thermal equilibrium distributions.
- **Recombination**: The electron-hole pair recombines radiatively.

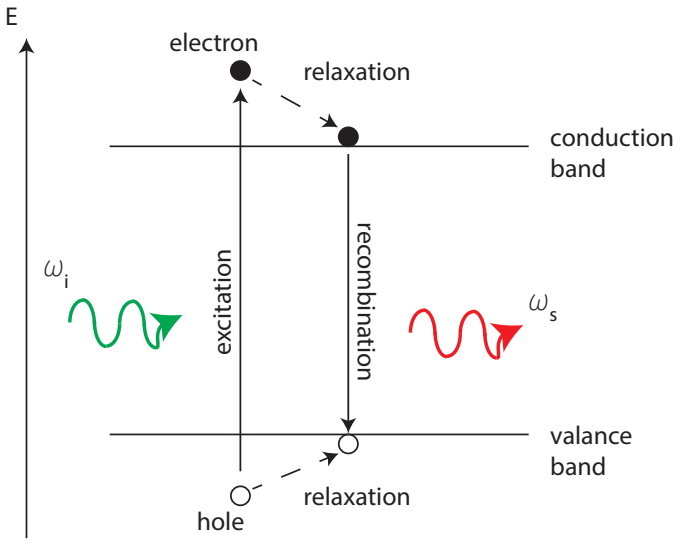

Figure 2.5 Scheme of the photoluminescence process in a semiconductor

Taking into account a perfect semiconductor the electron-hole pairs will thermalize and accumulate at the valence and conduction band extrema. There they recombine radiatively [31]. The probability for the radiatively recombination is very high for direct bandgap semiconductors with allowed dipole transitions. A prominent direct bandgap semiconductor is GaAs. It is a strong emitter of bandgap radiation

and thus it can be used as light emitting diode.
In a band-to-band transition electrons recombine with holes. Therefore τ_r is defined as the radiative recombination time of one electron and one hole. The rate of emission of photons by the recombination of electrons and holes is dependent of their concentration n_e and n_h and is given by $n_e n_h/\tau_r$. The radiative recombination time is dependent of the electron and hole energies and therefore of the excitation (photon) energy. Thus, τ_r is replaced by an averaged radiative recombination time $\langle\tau_r\rangle$. In a PL experiment always an equal number of electrons and holes are excited. Typically, the intrinsic carrier concentration n_i and p_i is very low, thus it is easy to excite optically in an intrinsic semiconductor enough carriers that $n_i = n_h >> n_i p_i$ [31]. Therefore n_i and p_i are negligible. The radiative recombination rate is given by $1/\tau_{rad} = n/\langle\tau_r\rangle$, where $n = n_e = n_h$. Additionally the electron-hole pairs can also recombine nonradiative. The total decay rate $(1/\tau_{tot})$ is then:

$$1/\tau_{tot} = 1/\tau_{rad} + 1/\tau_{nonrad}, \tag{2.1}$$

with $1/\tau_{nonrad}$ the nonradiative recombination rate. The energy of electron-hole pairs dissipates as heat via excitation of phonons in nonradiative processes [31].
To calculate the shape of a band-to-band PL spectra we use a direct bandgap semiconductor with the gap E_g and joint density of states

$$D_j \propto (E - E_g)^{1/2} \tag{2.2}$$

The quasi-equilibrium distributions f_e and f_h can be approximated by Boltzman distribution for low photoexcited density f_e and f_h:

$$f_h \text{ or } f_e \propto exp[-E/(k_B T)]. \tag{2.3}$$

The PL spectral shape is then given by substituting Eq. (2.1) and Eq. (2.2) into the emission rate for the transition from conduction band to valence band [31]

$$R_{cv} = A_{cv} f_c (1 - f_v), \tag{2.4}$$

where f_c and f_v are the electronic occupancies in the conduction and valence band, respectively. A_{cv} is the Einstein coefficient for two nondegenerated levels in a

medium with refractive index n_r [31, 46, 47].
The PL spectra shape is then:

$$I_{PL}(\hbar\omega) = \begin{cases} (\hbar\omega - E_g)^{1/2} exp[-(\hbar\omega - E_g)/(k_B T), & \text{for} \hbar > E_g \\ 0, & \text{otherwise} \end{cases} \tag{2.5}$$

$\hbar\omega$ is the emitted photon energy.
As an example we show in Fig. 2.6 the experimental PL spectra of GaAs measured under a pressure of 29.4 kbar and at room temperature [31, 48]. For the plot of the PL spectra (Fig. 2.6) Eq. (2.5) was used with a temperature of 373 K, because of laser heating.

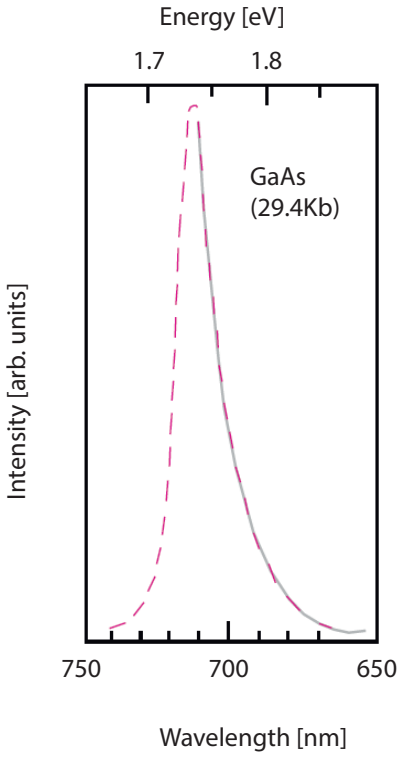

Figure 2.6 Photoluminescence spectrum of GaAs at a pressure of 29.4 kbar and at room temperature, adapted from Ref. [31, 48]. The dashed line are the measurements. The solid line was plotted using Eq. (2.5)

2.3 Band Lineup in Heterostructures

Combining different bandgaps in a artificial material is called heterostructure. In this work wurtzite nanowires with zincblende insertion are used. Due to the different bandgaps of wurtzite and zincblende GaAs, they form a heterostructure. The electron affinities determine the relative position of conduction and valence band (band alignment) [49]. The relative positions of the bands lead to different types of heterostructures. Type-I and type-II heterostructures are shown in Fig. 2.7.

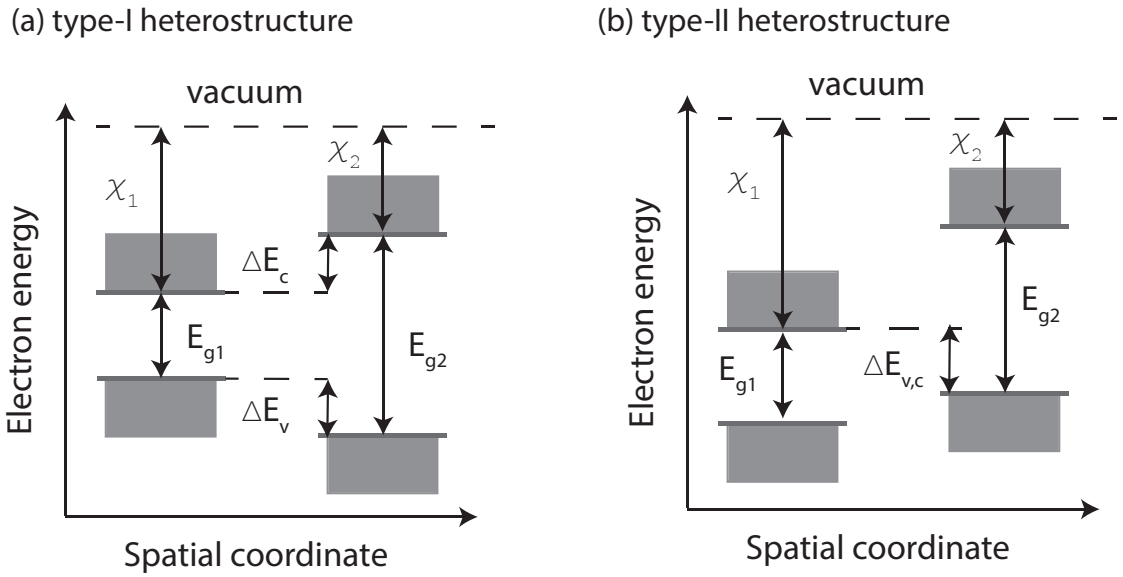

Figure 2.7 (a) type-I band alignment (b) type-II band alignment adapted from Ref. [49]

In a type-I heterostructure (straddled band lineup, Fig. 2.7(a)) the higher valence band and lower conduction band edge belongs to the material with smaller bandgap. Electron and holes will localize there. A type-II heterostructure has a staggered lineup and thus electrons and holes will localize in different materials [Fig. 2.7(b)].

There are special names for various layer sequences of high and low bandgap materials, such as single heterointerface, quantum well (Fig. 2.8(a)), multiple quantum well [Fig. 2.8(b)] and superlattice [Fig. 2.8(c)]. Nowadays such atomically precise layer sequences are grown for different material systems as AlGaAs/GaAs/InAs, InP/InGaAs or Si/SiGe [49]. The knowledge of the type of a wurtzite/zincblende

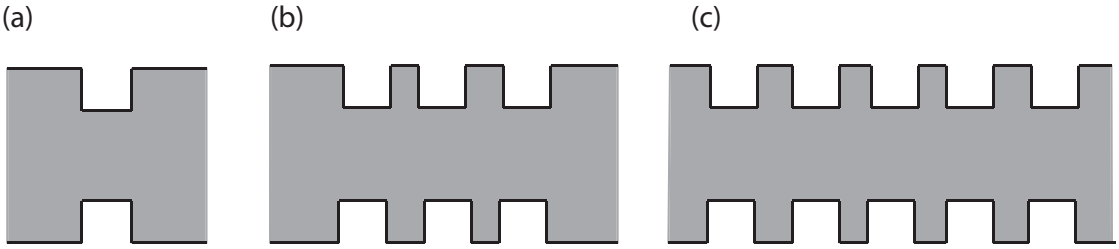

Figure 2.8 Heterostructures with different layer sequence. (a) quantum well, (b) multiple quantum well and (c) superlattice

GaAs heterostructure allows to design different heterostructures based only on one semiconductor.

It is very interesting to study how type-I and a type-II band alignment affect resonant Raman and photoluminescence experiments, which are described in detail below. To do so we assume a wurtzite nanowire with exactly one zincblende segment. For further considerations we use the calculated bandgap of wurtzite GaAs by Belabbes *et al.* [30]. $E_{WZ} = 1.46\,\mathrm{eV}$ at room temperature [30]. The zincblende bandgap at room temperature is $E_{ZB} = 1.425\,\mathrm{eV}$ [31]. At first we consider a type-I band alignment as shown in Fig. 2.7(a). As the zincblende bandgap is smaller then the wurtzite GaAs bandgap, in a type-I band alignment the zincblende structure forms a quantum well for electron and holes. In this situation the electrons in the conduction band recombine with holes from the valence band, which are located in the quantum well. This is called a direct transition. It means for the PL and resonant Raman experiments that all transition are direct [see Fig. 2.9(a)]. The transition energy is dependent of the width of the quantum well [50]

$$\hbar\omega = E_{ZB} + \frac{\hbar^2\pi^2}{2d^2}\left(\frac{1}{m_e} - \frac{1}{m_h}\right), \tag{2.6}$$

where d is the width of the quantum well, $m_e = 0.067 \cdot m_0$ the mass of the electrons in the conduction band and $m_h = -0.082 \cdot m_0$ the mass of the holes in the valence band [51]. From Eq. (2.6) we are able to calculate the transition energies dependent of the width d of the quantum well. The results are shown in Fig. 2.9(b). As can be seen the expected measurable transition energies are larger than the zincblende bandgap and smaller than the wurtzite bandgap for a type-I band-alignment.

In a type-II band alignment [Fig. 2.7(b) and 2.10(a)], we have a different situation. In the conduction band the electrons located in the zincblende quantum well have the possibility to recombine with holes, which are located in the neighboring wurtzite structure. This is called an indirect transition. The holes in the zincblende segment and in the wurtzite valence band in a type-II band alignment are not confined in the heterostructure. Therefore we have to rewrite Eq. (2.6) in order to calculate the direct and indirect transition energy. It is for direct transition

$$\hbar\omega = E_{ZB} + \frac{\hbar^2\pi^2}{2d^2}\left(\frac{1}{m_e}\right), \tag{2.7}$$

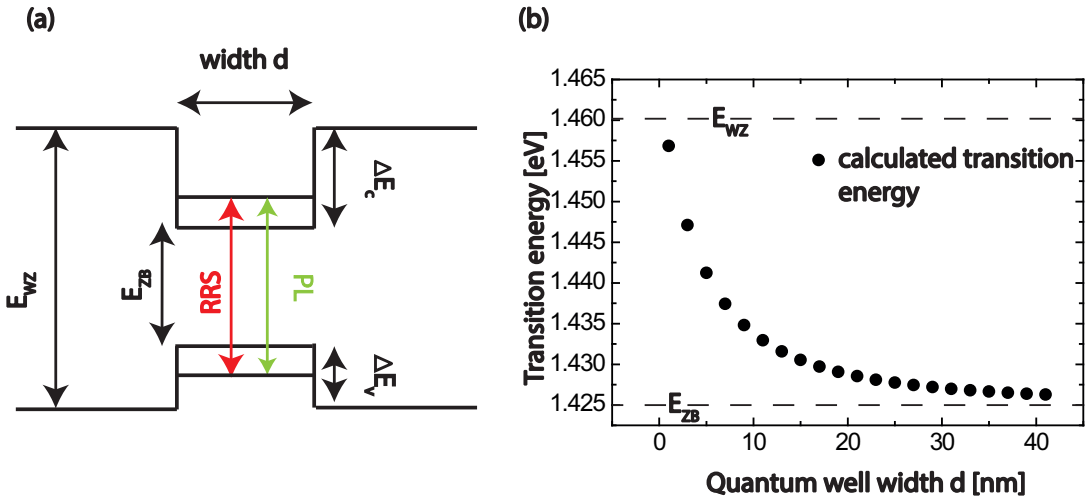

Figure 2.9 (a) type-I band alignment for a WZ/ZB heterostructure with possible transitions (b) calculated transition energies in dependence of the quantum well width d. The dashed line shows the zincblende bandgap energy and the wurtzite bandgap energy calculated by Ref. [30]

and for indirect transition

$$\hbar\omega = E_{ZB} - \Delta E_v + \frac{\hbar^2\pi^2}{2d^2}\left(\frac{1}{m_e}\right), \tag{2.8}$$

where $\Delta E_v = 0.117\,\text{eV}$ is the band offset between wurtzite and zincblende GaAs valence band edge position, taken from Ref. [30]. The results are shown in Fig. 2.10. As can be seen in Fig. 2.10 for the direct transitions the energy is for a wide quantum width slightly above the zincblende bandgap and for small quantum well width even higher then the calculated bandgap of wurtzite GaAs by Ref. [30]. For indirect transition, in contrast, the transition energies for wide quantum wells is even below the bandgap energy of zincblende GaAs.

The particularity of resonant Raman scattering is that all measured resonances are due to direct transitions [31, 52]. PL experiments, in contrast, show mainly indirect transition [Fig. 2.10(a)] [29]. The combination of both techniques is an ideal way to distinguish between direct and indirect transition [Fig. 2.10(a)] [52].

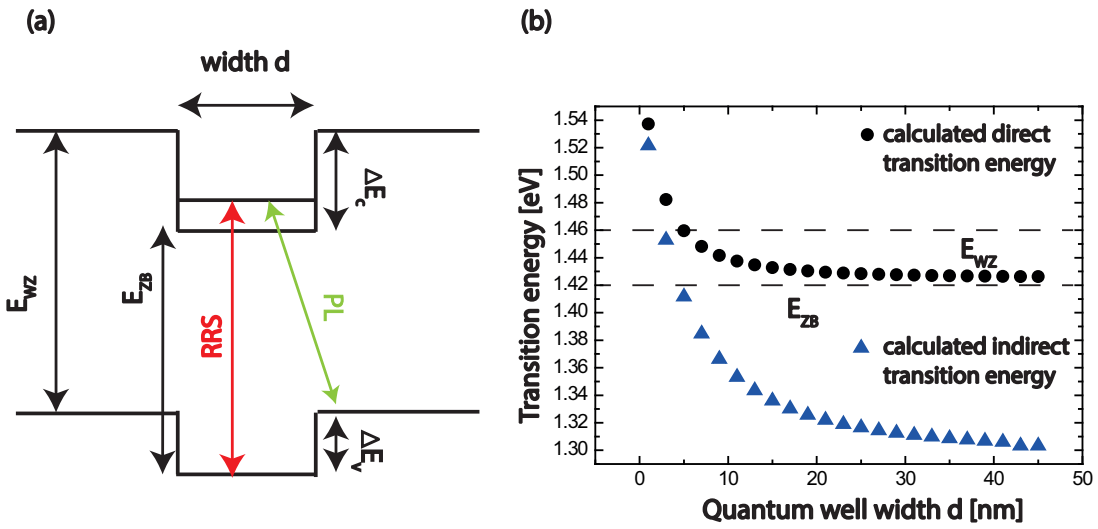

Figure 2.10 (a) type-II band alignment for a WZ/ZB heterostructure with possible transitions (b) calculated transition energies in dependence of the quantum well width d. The dashed line shows the zincblende bandgap energy and the wurtzite bandgap energy calculated by Ref. [30]

3 | The Resonant Raman Process

3.1 Vibrational Properties of GaAs

A solid consists of atoms, which have an average position. Since the atoms are elastically bonded they can deviate from their average position. This means that atoms in a crystal or solid vibrate at finite temperature around the equilibrium position because of their thermal motion. If the atoms vibrates randomly, each atom suffers random forces and the vibration immediately damps [34]. When each atom vibrates with a small relative displacement from the neighboring atoms, the vibration will continue. These modes are called lattice vibration. The quantized mode of a lattice vibration is called phonon. The lattice vibrations depends on the mass of the atoms and the symmetry of the crystal. The essential physics of lattice vibrations can be best explained by a linear chain, see Fig.3.1. We consider a one-dimensional chain, with two types of atoms as a model for semiconductors with a diatomic base, such as zincblende GaAs. In this model the lattice have alternating atoms A and B with a relative distance of $a/2$ (a is the lattice parameter). Depending of the displacement of the atoms, different waves exist, which are displayed in Fig. 3.1. For displacement vectors of each atom along the direction of the wave vector, we have longitudinal acoustic (LA) and longitudinal optical (LO) modes. Transversally polarized modes are modes with atoms moving with the planes normal to the wave vector, called transversal acoustic (TA) and transversal

optical (TO) modes. We differentiate between transversal and longitudinal, as wells as optical and acoustic waves.

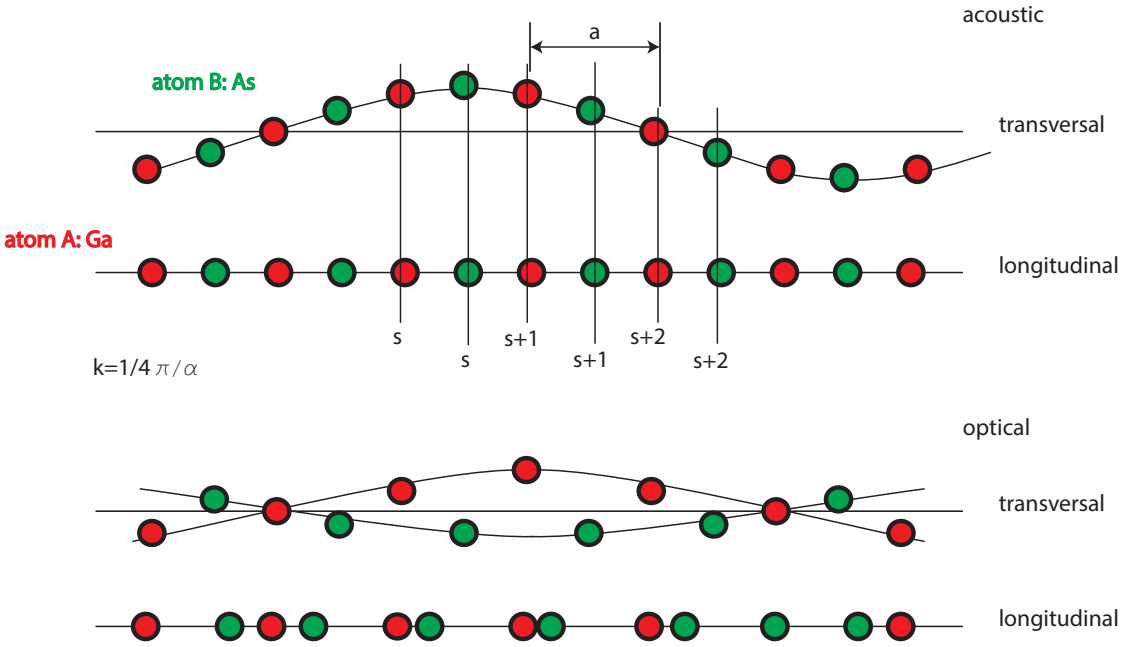

Figure 3.1 Visualization of optical and acoustic waves in a diatomical linear chain as GaAs. The position of the atoms is marked with s,$s+1$ and $s+2$. For acoustic waves the neighboring atoms move in the same direction; For optical waves the neighboring atoms move in the opposite direction.

In a diatomic linear chain the atom A (B) with its mass M_1 (M_2) are connected to each other by a spring constant (force constant) C. The distance between the nearest neighbor atoms at equilibrium is $a/2$. Defining the displacement of the atoms from their equilibrium positions by $u_0, u_1, u_2, u_3, ..., u_s, u_{s+1}, ...$, for atom A and $v_0, v_1, v_2, v_3, ..., v_s, v_{s+1}, ...$, the equation of motion of sth atom are:

$$M_1 \frac{d^2 u_s}{dt^2} = C(v_s + v_{s-1} - 2u_s) \tag{3.1}$$

$$M_2 \frac{d^2 v_s}{dt^2} = C(u_s + u_{s+1} - 2v_s) \tag{3.2}$$

For the solution the plane-wave ansatz with different amplitudes U and V for atom A and B is used:

$$u_s = U e^{-i(qsa-\omega t)} \tag{3.3}$$

and

$$v_s = V e^{-i(qsa-\omega t)} \tag{3.4}$$

which yields the solution

$$\omega^2(q)_{a,o} = C\left(\frac{1}{M_1} + \frac{1}{M_2}\right) \mp C\sqrt{\left(\frac{1}{M_1} + \frac{1}{M_2}\right)^2 - \frac{4}{M_1 M_2} sin^2\left(\frac{qa}{2}\right)}. \tag{3.5}$$

The indices a (o) belong to the $-$ $(+)$. Solution a(o) stands for acoustic (optical) branch. ω is dependent of the wave vector k, so the equation gives the dispersion relation for a diatomic linear chain which is shown in Fig. 3.2.

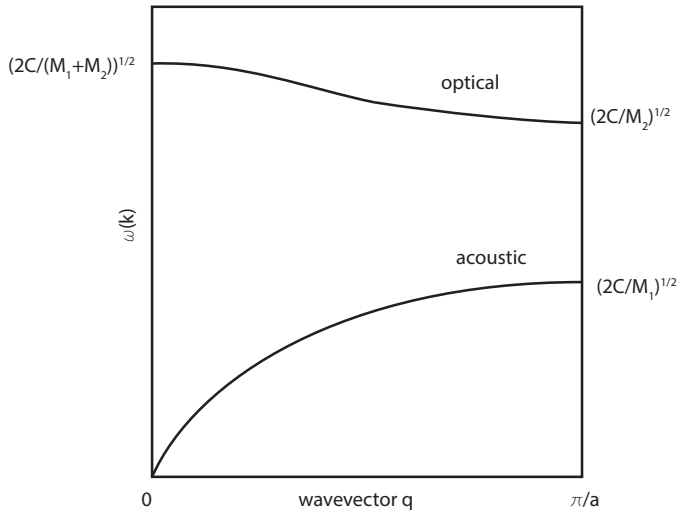

Figure 3.2 Dispersion relation for a diatomic linear chain. The optical branch is over the acoustic branch. At the zone boundary a frequency gap exists, where phonons are forbidden. The maximum frequency for the optical branch is given by $\omega_{max} = \sqrt{2C/(M_1 + M_2)}$

The dispersion relation has (for each longitudinal and transverse mode) two branches. The lower branch ["-" sign in Eq. (3.5)] is related to the acoustic mode. For the acoustic mode $\omega = 0$ at the Γ point and increase towards the zone boundary. At zone boundary the frequency is $\omega_{acoustic}(\pi/a) = \sqrt{2C/M_1}$. The upper branch ["+" sign in Eq. (3.5)] is related to the optical mode and has at zone center the largest phonon frequency $\omega_{max} = \sqrt{2C/(M_1 + M_2)}$. The dispersion is parabolic with negative curvature in the vicinity of the Γ point. At the zone boundary $\omega_{optical}(\pi/a) = \sqrt{2C/M_2}$. A detail description of the calculation can be found in Ref. [49, 53, 54] A three-dimensional crystal with p atoms in the basis, has $3p$ phonon branches, three acoustic and $(3p - 3)$ optical brunches [53].

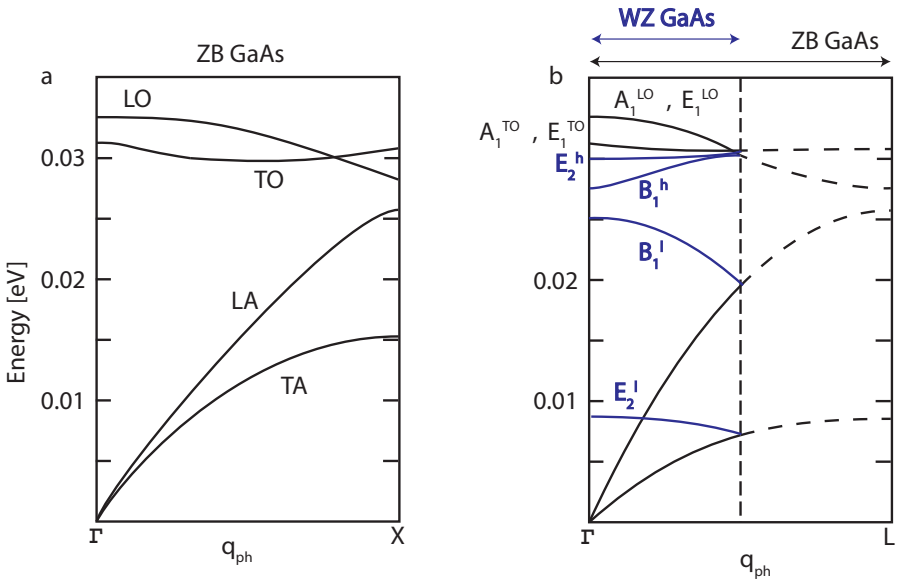

Figure 3.3 (a) Schematic dispersion relation of zincblende GaAs along $\Gamma \rightarrow X$. (b) Schematic dispersion relation of wurtzite GaAs along $\Gamma \rightarrow L$ as a result of the zone folding of the zincblende dispersion.

Phonons are the quantized quasi particles of the lattice vibrations. Applying quantum mechanics the lattice vibration (phonons) can be described by the harmonic

oscillator. The discrete energy of the phonons are given by

$$E_{Ph} = \left(n + \frac{1}{2}\right)\hbar\omega, \tag{3.6}$$

where n denotes the quantum number of the state, which corresponds to the number of quanta $\hbar\omega$ in the vibration. Applying the considerations to zincblende GaAs with its diatomic base we expect three acoustic and three optical phonon (one LO phonon mode and two TO phonon modes) branches. A schematic dispersion relation of zincblende GaAs is shown in Fig. 3.3(a). At the Γ point zincblende GaAs has two degenerated TO phonons modes and one LO phonon mode. The TO-LO splitting, which results in a higher LO energy at the Γ point is due to the long range electric fields for the long-wave LO [31]. As we showed above in wurtzite GaAs the L point is zone folded onto the Γ point. This affects not only the electronic band structure, but also the dispersion relation of wurtzite GaAs. The zincblende dispersion relation is folded along $\Gamma \rightarrow L$ and the L point appears at the Γ point in wurtzite GaAs [see Fig. 3.3(b)] [55]. Additionally wurtzite GaAs has four atoms per unit cell, so it exhibits nine optical phonon modes. Following Ref. [56], group theory predicts an A_1 phonon mode polarized along z (z is equal to the growth axis c), an E_1 phonon mode polarized in the xy plane, two E_2 and two B_1. The A_1 and E_1 splits again into TO and LO phonon modes, as can be seen in Fig. 3.3(b).

3.2 Macroscopic Theory of Raman Scattering

Raman scattering is the inelastic light scattering on optical phonons. In simple terms Raman scattering can be described as the absorption of a photon, the emission of a photon and the creation (Stokes) or the absorption (Anti-Stokes) of a phonon (see Fig. 3.4). Sir Chandrasekhara Venkata Raman observed the inelastic light scattering and published it in 1928 [57, 58]. For his work Sir Raman was awarded with the Nobel price in 1930 and the effect was named after him.

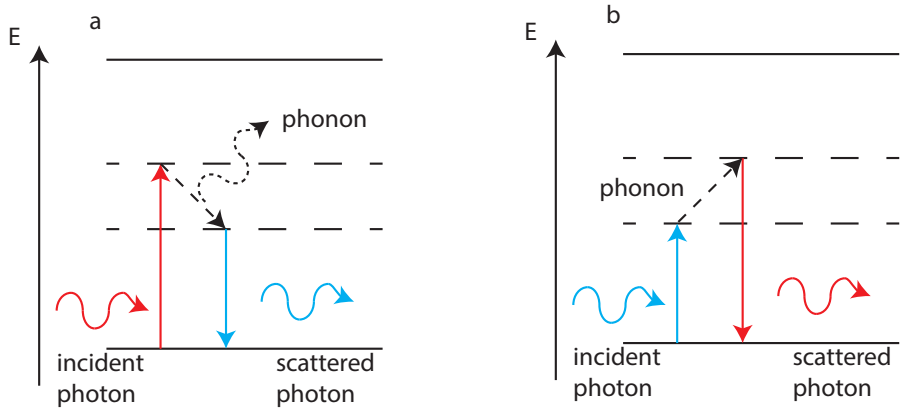

Figure 3.4 Scheme of the Raman scattering process. An incident photon is absorbed. The excited electron exchange energy with the lattice by creating (Stokes) (a) or annihilating (Anti-Stokes) (b) a phonon and emitting a photon with lower (Stokes) (a) or higher (Anti-Stokes) (b) energy. Dashed lines represent virtual states, solid lines correspond to real states.

Raman scattering has many advantages. It is non-destructive, the light does not have to be absorbed by the sample (as in fluorescence or photoluminescence experiments) and it can be used for the investigation of molecules and crystalline solids.

Table 3.1 Optical Raman-active phonon modes in zincblende and wurtzite GaAs after Ref. [31]

CRYSTAL STRUCTURE	**PHONON MODE**	**POSITION** $[cm^{-1}]$
zincblende	TO	267
	LO	291
wurtzite	E_1 (TO)	267
	E_1 (LO)	291
	A_1 (TO)	267
	A_1 (LO)	291
	E_2^h	259
	E_2^l	unknown

As we have shown above, wurtzite GaAs exhibits additional phonon modes. Using group theory [27], one is able to determine Raman-active phonons. They are summarized in Tab. 3.1 for the zincblende and wurtzite crystal structure.
We describe the Raman process by the macroscopic theory of light scattering at this point. An electric field $\boldsymbol{E}$ that is applied to a medium with a polarization $\boldsymbol{P}$ related to the field by

$$\boldsymbol{P} = \epsilon_0 \boldsymbol{\chi}_{jk} \boldsymbol{E}. \tag{3.7}$$

The components of $\boldsymbol{P}$ are given by

$$P_j = \epsilon_0 \chi_{jk} E_k. \tag{3.8}$$

Here χ_{jk} is the electric susceptibility, a second-rank tensor. Considering an electromagnetic field with a frequency ω that incidents the medium and is described by the plane wave

$$\boldsymbol{E}(\boldsymbol{r}, t) = \boldsymbol{E}(\boldsymbol{k}_i, \omega_i) cos(\boldsymbol{k}_i \cdot \boldsymbol{r} - \omega_i t). \tag{3.9}$$

The polarization can be then written as

$$\boldsymbol{P}(\boldsymbol{k}, t) = \boldsymbol{P}(\boldsymbol{k}_i, \omega_i) cos(\boldsymbol{k}_i \cdot \boldsymbol{r} - \omega_i t). \tag{3.10}$$

This results in the following relation between the amplitudes of the polarization and the electric field:

$$\boldsymbol{P}(\boldsymbol{k}_i, \omega_i) = \epsilon_0 \chi(\boldsymbol{k}_i, \omega_i) \boldsymbol{E}(\boldsymbol{k}_i, \omega_i). \tag{3.11}$$

The light scattering is induced by a local change of the susceptibility χ. In the Raman process the light is scattered by lattice vibrations, so we describe the atomic displacement by

$$\boldsymbol{u}(\boldsymbol{r}, t) = \boldsymbol{u}(\boldsymbol{q}, \omega_q) cos(\boldsymbol{q} \cdot \boldsymbol{r} - \omega_q t), \tag{3.12}$$

where ω_q and $\boldsymbol{q}$ are the angular frequency of the lattice vibrations and the wavevector. For small amplitudes of the lattice vibrations compared to the lattice constant, the change of χ can be expanded in a Taylor series as

$$\chi(\boldsymbol{k}_i, \omega_i, \boldsymbol{u}) = \chi^{(0)}(\boldsymbol{k}_i, \omega_i) + \left(\frac{\delta \chi}{\delta \boldsymbol{u}}\right)_{\boldsymbol{u}=0} \boldsymbol{u}(\boldsymbol{r}, t) + ... \tag{3.13}$$

The susceptibilityχ is then expressed by

$$\chi_{jk} = \chi_{jk}^{(0)} + \chi_{jk,l} u_l + \chi_{jk,lm} u_l u_m + ..., \tag{3.14}$$

with

$$\chi_{jk,l} = \left(\frac{\delta \chi_{jk}}{\delta u_l}\right)_{\boldsymbol{u}=0} \text{ and } \chi_{jk,lm} = \left(\frac{\delta^2 \chi_{jk}}{\delta u_l \delta u_m}\right)_{\boldsymbol{u}=0}. \tag{3.15}$$

It is clear that $\chi_{jk,l}$ and $\chi_{jk,lm}$ are third-rank and fourth-rank tensors. Inserting Eq. (3.14) in Eq. (3.11) the polarization can be written as

$$\boldsymbol{P}(\boldsymbol{r}, t, \boldsymbol{u}) = \boldsymbol{P}^{(0)}(\boldsymbol{r}, t) + \boldsymbol{P}^{(ind)}(\boldsymbol{r}, t, \boldsymbol{u}), \tag{3.16}$$

with

$$\boldsymbol{P}^{(0)}(\boldsymbol{r}, t) = \chi^{(0)}(\boldsymbol{k}_i, \omega_i) \epsilon_0 \boldsymbol{E}(\boldsymbol{k}_i, \omega_i) cos(\boldsymbol{k}_i \cdot \boldsymbol{r} - \omega_i t) \tag{3.17}$$

and

$$\boldsymbol{P}^{(ind)}(\boldsymbol{r}, t, \boldsymbol{u}) = \left(\frac{\delta \chi}{\delta \boldsymbol{u}}\right)_{\boldsymbol{u}=0} \boldsymbol{u}(\boldsymbol{r}, t) \epsilon_0 \boldsymbol{E}(\boldsymbol{k}_i \omega_i) cos(\boldsymbol{k}_i \cdot \boldsymbol{r} - \omega_i t). \tag{3.18}$$

The term $\boldsymbol{P}^{(ind)}$ can be rewritten using lattice vibration and it is related to Raman scattering [34]

$$\begin{aligned}\boldsymbol{P}^{(ind)}(\boldsymbol{r},t,\boldsymbol{u}) = \frac{1}{2}\epsilon_0 \left(\frac{\delta\chi}{\delta\boldsymbol{u}}\right)_{\boldsymbol{u}=0} \boldsymbol{u}(\boldsymbol{q},\boldsymbol{\omega_q})\boldsymbol{E}(\boldsymbol{k}_i,\omega_i) \\ \times[cos(\boldsymbol{k}_i+\boldsymbol{q}\cdot\boldsymbol{r}-(\omega_i+\omega_q)t + cos(\boldsymbol{k}_i-\boldsymbol{q}\cdot\boldsymbol{r}-(\omega_i-\omega_q)t]\end{aligned} \tag{3.19}$$

Eq. (3.19) shows that $P^{(ind)}$ consists of the Stoke shift wave with wave vectors $\boldsymbol{k}_s = (\boldsymbol{k}_i - \boldsymbol{q})$ and angular frequency $\omega_s = (\omega_i - \omega_q)$ and of the anti-Stokes wave with wave vector $\boldsymbol{k}_{as} = (\boldsymbol{k}_i + \boldsymbol{q})$ and angular frequency $\omega_{as} = (\omega_i + \omega_q)$ [34]. In simple terms, in a Raman experiment different scattered lines appear on both sides of the laser line shifted by the phonon frequency. The shift is called Raman shift. During the scattering the energy conservation law and momentum conservation law hold:

$$\omega_i = \omega_s \pm \omega_q \tag{3.20}$$

and

$$\boldsymbol{k}_i = \boldsymbol{k}_s \pm \boldsymbol{q} \tag{3.21}$$

where + represents Stokes and − anti-Stokes scattering.
The intensity of the Raman scattered light is determined by $P^{(ind)}$ [34]. As the scattering intensity is defined by the Raman tensors [31, 34], we discuss Raman tensors first. One is able to describe the polarization due to the lattice vibrations χ_{ij} by

$$\chi_{ij} = \chi_{ij}^{(0)} + \sum_k \chi_{ij,k}u_k + \sum_{k,l}\chi_{ij,kl}u_k u_l + 0(u^3), \tag{3.22}$$

where

$$\chi_{ij,k} = \left(\frac{\delta\chi_{ij}}{\delta u_k}\right)_{\boldsymbol{u}=0}, \ \chi_{ij,kl} = \left(\frac{\delta^2\chi_{ij}}{\delta u_k \delta u_l}\right)_{\boldsymbol{u}=0} \tag{3.23}$$

χ is the first-order Raman tensor and the term proportional to $\boldsymbol{u}$ represents the first-order Raman scattering. The second derivative of χ gives the second-order Raman scattering. $\chi_{ij,k}$ is a third-rank tensor. Its non-zero components are determined from the crystal symmetry [31, 34]. For unpolarized light the Raman

intensity for can be calculated following Ref. [59]:

$$I_s = \frac{3\hbar_s^4 L d\Omega}{\rho c^4 \omega_q} |\chi_{zy,x}|^2 (n_q + 1), \tag{3.24}$$

where ρ is the crystal density, n_q is the occupation number of phonons (given by Bose-Einstein statistics), $d\Omega$ is the detector solid angle and L is the sample length along the light wave vector $\boldsymbol{k}_i$. Typically in Raman experiments the measurements are performed using polarized light. In this case the electric polarization, which causes the scattering is given by

$$\boldsymbol{P}^{(ind)} \propto \left(\frac{\delta\chi}{\delta \boldsymbol{u}}\right) \boldsymbol{u}(\boldsymbol{q}, \omega_q) \boldsymbol{e}^i = \left(\frac{\delta\chi_{ij}}{\delta \boldsymbol{u}_k}\right) \boldsymbol{u}_k(\boldsymbol{q}, \omega_q) \boldsymbol{e}_i = (\chi_{ij,k}) u_k \cdot e_j^i \sim R_{ji}^k \cdot e_j^i. \tag{3.25}$$

$\boldsymbol{e}^i$ is the unit polarization vector of incident light. R is the Raman tensor. The term $\boldsymbol{e}^s \cdot \boldsymbol{P}^{(ind)}$ gives the scattered light intensity of the polarization direction $\boldsymbol{e}^s$ and the intensity in a Raman process is then

$$I_s \propto \left| \boldsymbol{e}^i \cdot R_{ji}^k \cdot \boldsymbol{e}^s \right|^2 \tag{3.26}$$

The non-zero components are determined by the crystal symmetry. The Raman selection rules are determined by the Raman tensor and it reflects the crystal symmetry. In our case we deal with zincblende and wurtzite GaAs of the Γ_{15} phonons. For zincblende GaAs the Raman tensor has the following form [31]:

$$R(x) = \begin{pmatrix} 0 & 0 & 0 \\ 0 & 0 & d \\ 0 & d & 0 \end{pmatrix}, \; R(y) = \begin{pmatrix} 0 & 0 & d \\ 0 & 0 & 0 \\ d & 0 & 0 \end{pmatrix}, \; R(z) = \begin{pmatrix} 0 & d & 0 \\ d & 0 & 0 \\ 0 & 0 & 0 \end{pmatrix} \tag{3.27}$$

The Raman tensors are referred to the crystal axes x [100], y [010] and z [001]. These matrices describe the deformation potential scattering. As in this work the Fröhlich coupling is very important (see Chapter 3), the Raman tensor for the

forbidden Fröhlich coupling is shown below:

$$R_{Fröhlich} = \begin{pmatrix} d_F & 0 & 0 \\ 0 & d_F & 0 \\ 0 & 0 & d_F \end{pmatrix}. \tag{3.28}$$

It can be easily seen that Fröhlich coupling is only allowed for parallel polarization of incident and scattered light $(e_i||e_s)$.
For wurtzite GaAs the Raman tensors are [56]

$$\begin{gathered} A_1(z) = \begin{pmatrix} a & 0 & 0 \\ 0 & a & 0 \\ 0 & 0 & b \end{pmatrix}, E_1(x) = \begin{pmatrix} 0 & 0 & c \\ 0 & 0 & 0 \\ c & 0 & 0 \end{pmatrix} \\ E_1(y) = \begin{pmatrix} 0 & 0 & 0 \\ 0 & 0 & c \\ 0 & c & 0 \end{pmatrix}, E_2 = \begin{pmatrix} 0 & d & 0 \\ d & 0 & 0 \\ 0 & 0 & 0 \end{pmatrix}, E_2 = \begin{pmatrix} d & 0 & 0 \\ 0 & -d & 0 \\ 0 & 0 & 0 \end{pmatrix} \end{gathered} \tag{3.29}$$

Table 3.2 Raman selection rules for zincblende and wurtzite GaAs nanowires for different scattering configurations. Note: The selection rules were calculated with respect to nanowire axis, but they reflect the selection rules for bulk GaAs

CRYSTAL STRUCTURE	**CONFIGURATION**	**ALLOWED PHONON MODES**
zincblende	$x(-,-)\overline{x}$	$T_2(TO)\ T_2(LO)$
wurtzite	$x(z,z)\overline{x}$	$A_1(TO)\ E_2$
	$x(y,y)\overline{x}$	$E_1(TO)$
	$x(z,y)\overline{x}$	$A_1(TO)$

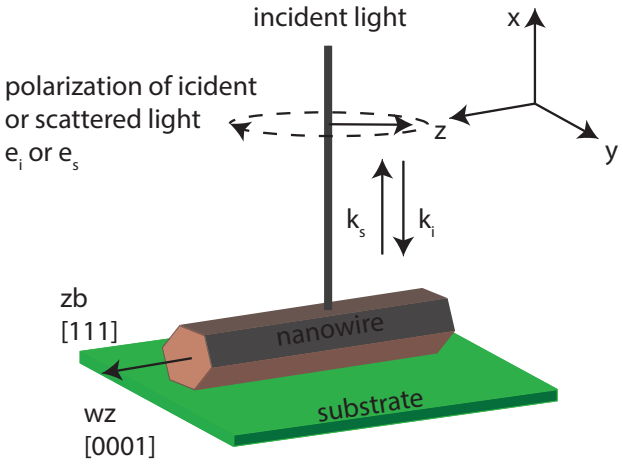

Figure 3.5 Scheme of the backscattering configuration used for Raman experiments in this work

Using Eq. (3.26) allows to determine the allowed phonon modes of the wurtzite and zincblende nanowires for the backscattering configuration (Fig. 3.5). For the Raman experiments the nanowire is excited with polarized light along and perpendicular to the nanowire c-axis. The incident and scattered light is directed along x. The observable phonon modes, depending on the scattering configuration, are summarized in Tab. 3.2. The scattering geometry is described in the Porto notation: $\underline{k}_i(\underline{e}_i, \underline{e}_s)\underline{k}_s$, where $\underline{e}_{i,s}$ are the polarization and $\underline{k}_{i,s}$ the direction of the incident and scattered light.

3.3 Microscopic Theory of Raman Scattering

To describe the resonant Raman scattering in detail we have to consider the quantum mechanical theory. Therefore we now study the microscopic interpretation of Raman scattering and use the results to describe the resonant Raman process.
The Raman process can be described microscopically as followed: An incident photon excites an electron from its ground state. A new exited state is created by the interaction of the electron with a phonon. The electron then recombines with a hole and a photon is emitted. When the incident photon energy is near to the fundamental absorption edge, one my expect that the scattering intensity increases. This process is called *resonance Raman scattering* and is displayed in Fig. 3.6.

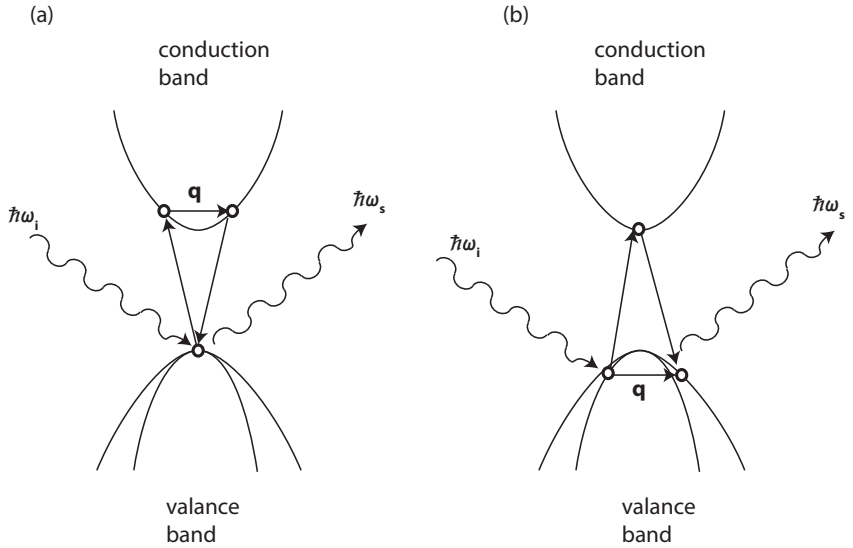

Figure 3.6 Quantum mechanical representation of Raman scattering adapted from Ref. [34]. An incident photon induces interband transition, electron (a) or hole (b) scattering via a phonon, emission of a scattered photon

The Raman process shown in Fig. 3.6 can be simply described in three steps:

- an incident photon excites the semiconductor on an intermediate state by creation an electron-hole pair. The process is due to the electron-radiation Hamiltonian
- via electron-phonon interaction Hamiltonian, the electron-hole pair is scattered into a second intermediate state by emitting a phonon
- the electron-hole pair recombines radiatively

The three steps are transferred into a Feynman diagram. Fig. 3.7 shows an example of a Feynman diagram for the one phonon (Stokes) Raman process, adapted from Ref. [31].

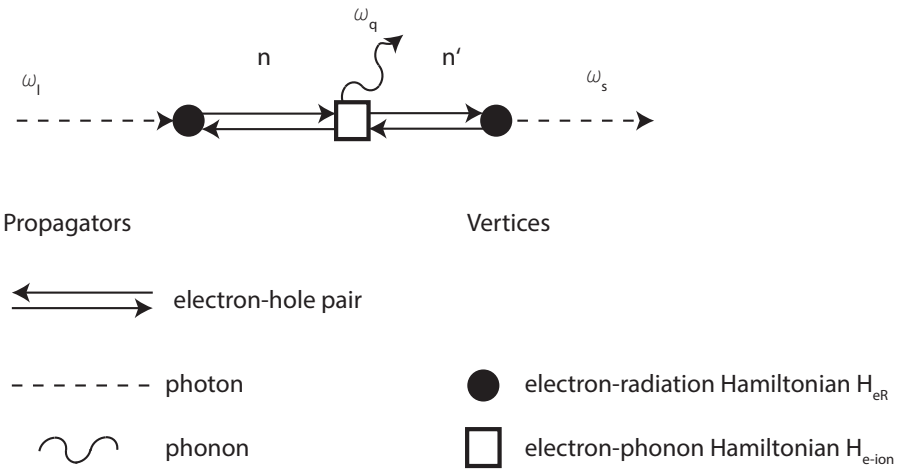

Figure 3.7 Feynman diagram for the one phonon (Stokes) Raman process.

There are several rules for the drawing of the Feynman diagrams:

- Excitations (photon, electron-hole pair and phonon) are drawn by dotted, solid and dashed lines and are called propagators

- The interaction between these excitations is called vertex. It is indicated by an intersection connecting two propagators. The • is used for the electron-photon interaction and a □ for the electron-phonon interaction.

- Propagators are drawn with arrows, which represents the creation or annihilation at the interaction. An arrow leaving the vertex indicates creation and an arrow towards a vertex indicates annihilation.

- The sequential progress of the interactions are from left to right.

- From one diagram, the remaining diagrams are drawn by changing the order of the vertices.

Applying these rules on Fig. 3.7 the remaining diagrams can be easily obtained and they are shown in Fig. 3.8.

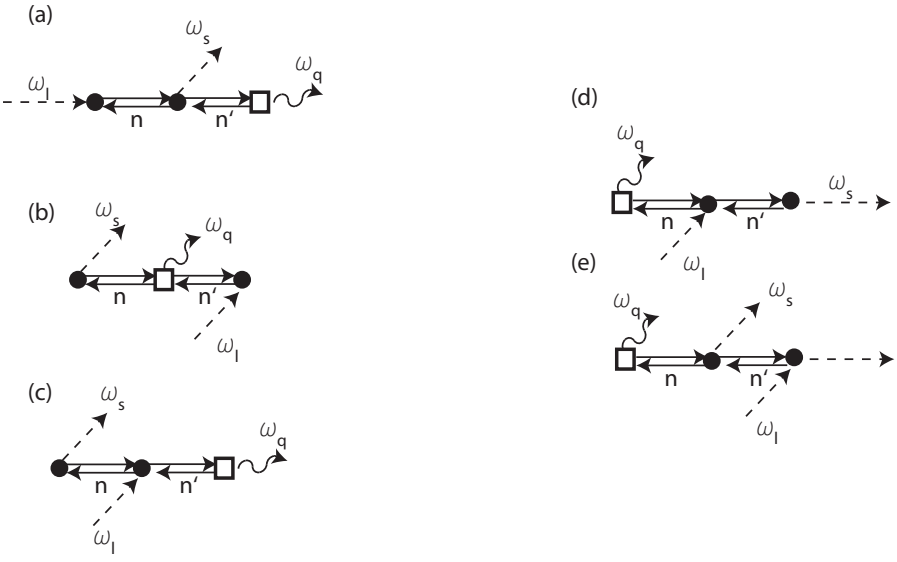

Figure 3.8 Remaining five Feynman diagrams for the (Stokes) Raman process.

The calculation to transform the Feynman diagram into terms in the perturbation expansion of the scattering probability is shown in Ref. [31] and Ref. [60] and can be done as follows: An initial state $\big|i\big\rangle$ and a final state $\big|f\big\rangle$ is defined and the scattering rate is calculated using Fermi Golden Rule. For simplicity we consider as an example the case in Fig. 3.7. The Hamiltonian is given by

$$H = H_0 + H_{er} + H_{el}.$$

H_{el} is the interaction Hamiltonian for electron-lattice vibrations, which is describe in detail below. H_{er} is the interaction Hamiltonian of electron-photon pair and $H_0 = H_e + H_l$ is the sum of the electron and lattice vibration Hamiltonians. To calculate the perturbation of the scattering probability from the diagrams, we obtain from the first vertex

$$\sum_n \frac{\big\langle n\big|H_{er}(\omega_i)\big|i\big\rangle}{[\hbar\omega_i - (E_n - E_i)]} \tag{3.30}$$

$\big|n\big\rangle$ is the intermediate state with the energy E_n and $\big|i\big\rangle$ is the initial state with the energy E_i For absorption the term $\hbar\omega_i$ of the energy denominator has + sign and − sign for emission of the quanta. Using the second vertex leads to

$$\sum_{n,n'} \frac{\big\langle n'\big|H_{el}(\omega_q)\big|n\big\rangle\big\langle n\big|H_{er}(\omega_i)\big|i\big\rangle}{[\hbar\omega_i - (E_n - E_i) - \hbar\omega_q - (E_{n'} - E_n)][\hbar\omega_i - (E_n - E_i)]} \tag{3.31}$$

where $\big|n'\big\rangle$ is a second intermediate state. The term $-\hbar\omega_q$ corresponds to the emission of a phonon. The equation can be rewritten and we obtain

$$\sum_{n,n'} \frac{\big\langle n'\big|H_{el}(\omega_q)\big|n\big\rangle\big\langle n\big|H_{er}(\omega_i)\big|i\big\rangle}{[\hbar\omega_i - \hbar\omega_q - (E_{n'} - E_n)][\hbar\omega_i - (E_n - E_i)]} \tag{3.32}$$

By calculating the final (third) vertex term the total energy have to be conserved. Therefore the energy denominator is given by

$$[\hbar\omega_i - (E_n - E_i) - \hbar\omega_q - (E_{n'} - E_n) - \hbar\omega_s - (E_f - E_i)] = [\hbar\omega_i - \hbar\omega_q - \hbar\omega_s - (E_i - E_f)]. \tag{3.33}$$

As the electron returns to the ground state after Raman scattering, the final state and the initial state are the same. This leads to

$$[\hbar\omega_i - \hbar\omega_q - \hbar\omega_s].$$

From the energy conservation rule, one knows that the term have to be zero and in the calculation of the scattering probability the term is replaced by the Dirac delta function $\delta[\hbar\omega_i - \hbar\omega_q - \hbar\omega_s]$. The scattering probability is then given by

$$w(-\omega_i, \omega_s, \omega_q) = \frac{2\pi}{\hbar} \left| \sum_{n,n'} \frac{\langle 0|H_{er}(\omega_s)|n'\rangle\langle n'|H_{el}(\omega_q)|n\rangle\langle n|H_{er}(\omega_i)|i\rangle}{[\hbar\omega_i - \hbar\omega_q - (E_{n'} - E_i)][\hbar\omega_i - (E_n - E_i)]} \right|^2 \times\delta[\hbar\omega_i - \hbar\omega_q - \hbar\omega_s]. \tag{3.34}$$

For completeness the calculation have to be done for all diagrams. Therefore all contributions are summed up. The initial state is $|i\rangle = |f\rangle = |0\rangle$, the ground state. The result is then

$$\begin{aligned} w(-\omega_i, \omega_s, \omega_q) = \frac{2\pi}{\hbar} \Big| \sum_{n,n'} & \frac{\langle 0|H_{er}(\omega_s)|n'\rangle\langle n'|H_{el}(\omega_q)|n\rangle\langle n|H_{er}(\omega_i)|0\rangle}{[\hbar\omega_i - \hbar\omega_q - (E_{n'} - E_0)][\hbar\omega_i - (E_n - E_0)]} \\ & + \frac{\langle 0|H_{er}(\omega_s)|n'\rangle\langle n'|H_{er}(\omega_q)|n\rangle\langle n|H_{el}(\omega_i)|0\rangle}{[\hbar\omega_i - \hbar\omega_s - (E_{n'} - E_0)][-\hbar\omega_s - (E_n - E_0)]} \\ & + \frac{\langle 0|H_{er}(\omega_s)|n'\rangle\langle n'|H_{el}(\omega_q)|n\rangle\langle n|H_{er}(\omega_i)|0\rangle}{[-\hbar\omega_s - \hbar\omega_q - (E_{n'} - E_0)][-\hbar\omega_s - (E_n - E_0)]} \\ & + \frac{\langle 0|H_{er}(\omega_s)|n'\rangle\langle n'|H_{er}(\omega_q)|n\rangle\langle n|H_{el}(\omega_i)|0\rangle}{[-\hbar\omega_q - \hbar\omega_i - (E_{n'} - E_0)][-\hbar\omega_s - (E_n - E_0)]} \\ & + \frac{\langle 0|H_{er}(\omega_s)|n'\rangle\langle n'|H_{el}(\omega_q)|n\rangle\langle n|H_{er}(\omega_i)|0\rangle}{[-\hbar\omega_q - \hbar\omega_i - (E_{n'} - E_0)][-\hbar\omega_q - (E_n - E_0)]} \\ & + \frac{\langle 0|H_{er}(\omega_s)|n'\rangle\langle n'|H_{el}(\omega_q)|n\rangle\langle n|H_{er}(\omega_i)|0\rangle}{[-\hbar\omega_q - \hbar\omega_s - (E_{n'} - E_0)][-\hbar\omega_q - (E_n - E_0)]} \Big|^2 \\ & \times\delta[\hbar\omega_i - \hbar\omega_q - \hbar\omega_s] \end{aligned} \tag{3.35}$$

Following Loudon [61] the Raman intensity can be deduced using the same scattering geometry as in the classical theory by Smith [59] (Eq. (3.24)):

$$I = \frac{e^4 \omega_s V (n_q + 1) L d\Omega}{4\hbar^3 m^4 d^2 M c^4 \omega_q \omega_i} \left[|R^x_{yz}|^2 + |R^y_{zx}|^2 + |R^z_{xy}|^2 \right]. \tag{3.36}$$

m and e are the effective mass of an electron and the magnitude of the electronic charge. V is the volume of the crystal M $(1/M = 1/M_1 + 1/M_2)$ is the reduced mass of the lattice atoms and d is the lattice constant. n_q is the phonon occupation number. R^x_{yz} is the Raman tensor defined before. For zincblende type crystals it is:

$$\begin{aligned} & R^x_{yz}(-\omega_i, \omega_s, \omega_q) \\ &= \frac{1}{V} \sum_{\alpha,\beta} \left[\frac{p^z_{0\beta} \Xi^x_{\beta\alpha} p^y_{\alpha 0}}{(\omega_i - \omega_q - \omega_\beta)(\omega_i - \omega_\alpha)} + 5\text{other terms} \right]. \end{aligned} \tag{3.37}$$

$p^y_{\alpha 0} = \langle \alpha | H_{el} | 0 \rangle$ is the momentum matrix element for the light polarization y.
$\hbar\omega_\alpha = E_\alpha - E_0$ and $\hbar\omega_\beta = E_\beta - E_0$
$\Xi^i_{\beta\alpha}$ is defined by

$$\langle \alpha | H_{el} | \beta \rangle = \Xi^i_{\beta\alpha} \frac{\overline{u}_i}{d},$$

$\Xi^i_{\beta\alpha}$ represents the deformation constant and is defined in Ref. [62]. $\overline{u}_i$ is the amplitude of the phonon in x direction. From Eq. (3.36) and following Loudon [61] the scattering efficiency is about 10^{-6}. The discussion above shows the relation between the macroscopic theory of Raman scattering and the quantum mechanical results of the Raman tensor.

3.4 The Electron-Phonon Interaction

Before we treat the resonant Raman scattering we want to show different coupling mechanism between electrons and phonons that were represent in Eq. (3.35) by the Hamiltonian H_{el}. In polar materials as GaAs there are two types of electron-phonon interaction. Due to the relative displacement of atoms the optical phonons results in a microscopic distortion of the crystal. This leads to a change in the electronic energy. This interaction between electron and phonon is called **deformation potential**. H_{el} is given by

$$H_{el} = D_{n,\boldsymbol{k}}(u/a_0), \tag{3.38}$$

where $D_{n,\boldsymbol{k}}$ is the optical phonon deformation potential for the energy band indexed by n and $\boldsymbol{k}$ [31]. a_0 is the distance between two neighboring atoms and u is the relative displacement between these atoms, associated with a zone-center optical phonon. The deformation potential is a short-range interaction, because it is independent of the phonon wave vector [31]. The Raman scattering intensity, which is due to deformation potential, can be calculated by using the Raman tensors, which are defined in above (Eq. (3.26)).
The second mechanism is the Fröhlich coupling. In a polar lattice an LO phonon (longitudinal displacement of ions) generates a macroscopic field. Electrons interact with the electric field. The electric field is described by

$$\boldsymbol{E}_{LO} = -F\boldsymbol{u}_{LO} \tag{3.39}$$

with

$$F = -\left[4\pi N\mu\omega_{LO}^2(\epsilon_\infty^{-1} - \epsilon_0^{-1})\right]^{1/2}(4\pi\epsilon_0)^{-1/2}, \tag{3.40}$$

where ω_{LO} is the LO frequency and ϵ_∞^{-1} and ϵ_0^{-1} are the high- and low-frequency dielectric constants [31]. N is the number of unit cells per volume of the crystal and $\boldsymbol{u}_{LO}$ is the displacement of the positive ion relative to the negative ion. μ is the reduced mass

$$\mu^1{-}1 = M_1^{-1} + M_2^{-1}.$$

M_1^{-1} and M_2^{-1} are the masses of the two atoms inside the primitive cell. The longitudinal field in Eq. (3.39) can be expressed as a scalar potential

$$\Phi_{LO} = (F/iq)u_{LO} \tag{3.41}$$

The interaction of this macroscopic Coulomb potential and an electron of charge e is the *Fröhlich coupling*. The Hamiltonian is given by

$$H_{Fr} = (-e)\Phi_{LO} = (ieF/q)u_{LO}. \tag{3.42}$$

When the displacement u_{LO} is given by [31]

$$u_{LO} = (\hbar/2N\mu\omega_{LO})^{1/2}\left(c_q^+ exp[i(\boldsymbol{q}\cdot\boldsymbol{r} - \omega_{LO}t)] - c.c.\right) \tag{3.43}$$

and the resulting Hamiltonian is

$$H_{Fr} = \sum_{\boldsymbol{q}}(iC_F/q)\left(c_q^+ exp[i(\boldsymbol{q}\cdot\boldsymbol{r} - \omega_{LO}t)] - c.c.\right), \tag{3.44}$$

where the coefficient C_F is

$$C_F = \left[\frac{2\pi\hbar\omega_{LO}}{nV}(\epsilon_\infty^{-1} - \epsilon_0^{-1})\right]^{1/2}(4\pi\epsilon_0)^{-1/2} \tag{3.45}$$

The Fröhlich interaction can be calculated using macroscopic parameters such as the dielectric constants.

Fröhlich coupling is divided into *allowed* and *forbidden* scattering. The allowed scattering is also called electro-optic (or interband) scattering. It follows the same selection rules as the deformation potential scattering by LO phonons. Fröhlich interaction leads to the forbidden scattering. When the incident or scattered light is near to a band to band transition the forbidden scattering makes a strong contribution to the measured Raman scattering and have a very strong resonance behavior [63, 64].

3.5 Resonant Raman Scattering

To describe resonant Raman scattering we use perturbation theory, see Eq. (3.35).Because of the uncertainty of the coefficients involved in Eq. (3.35), it is impossible to determine the scattering efficiency. To analyze and to describe the resonant Raman process, the term of the most important contribution is used in the following and the other terms are treated as background and replaced by a constant, as was done in Ref. [31, 34]. From the six Feynman diagrams, gives the one shown in Fig. 3.7 the strongest contribution [31, 34]. We assume that the initial state is the ground state $\big|0\big\rangle$ of the semiconductor with no electron-hole pairs excited. Its energy is zero. The resonant intermediate state is denoted as $\big|a\big\rangle$ with the energy E_a. The scattering probability in the vicinity of E_a for a given phonon mode is then (after summing over ω_s to remove the delta function)

$$w(\omega_i) \approx \frac{2\pi}{\hbar} \left| \frac{\big\langle 0\big|H_{er}(\omega_i)\big|a\big\rangle\big\langle a\big|H_{el}\big|a\big\rangle\big\langle a\big|H_{er}(\omega_s)\big|0\big\rangle}{(E_a - \hbar\omega_i)(E_a - \hbar\omega_s)} + C \right|^2 , \tag{3.46}$$

where C is the constant background. It can be seen, that whenever the denominators $E_a - \hbar\omega_i$ or $E_a - \hbar\omega_s$ in Eq. (3.46) become small, the scattering probability is drastically enhanced. The case $E_a = \hbar\omega_i$ is named ingoing resonance and the case $E_a = \hbar\omega_S$ is named outgoing resonance. Both resonance processes are displayed in Fig. 3.9. For the resonance case (ingoing or outgoing) Eq. (3.46) diverges. This is an unphysical situation, which can be avoided by assuming that the state $\big|a\big\rangle$ has a finite lifetime τ_a, due to non-radiative and radiative decay processes. Therefore E_a is replaced by a complex energy $E_a - i\Gamma_a$ [65]. Γ_a is the damping constant and it is defined by $\Gamma_a = \hbar/\tau_a$ [31]. The Raman scattering probability can then be rewritten as

$$w(\omega_i) \approx \frac{2\pi}{\hbar} \left| \frac{\big\langle 0\big|H_{er}(\omega_i)\big|a\big\rangle\big\langle a\big|H_{el}\big|a\big\rangle\big\langle a\big|H_{er}(\omega_s)\big|0\big\rangle}{(E_a - \hbar\omega_i - i\Gamma_a)(E_a - \hbar\omega_s - i\Gamma_a)} + C \right|^2 . \tag{3.47}$$

As in this work the resonant Raman scattering in the vicinity of absorption continua is very interesting, we consider a direct bandgap semiconductor with parabolic conduction and valance bands. For simplicity we assume that the three matrix ele-

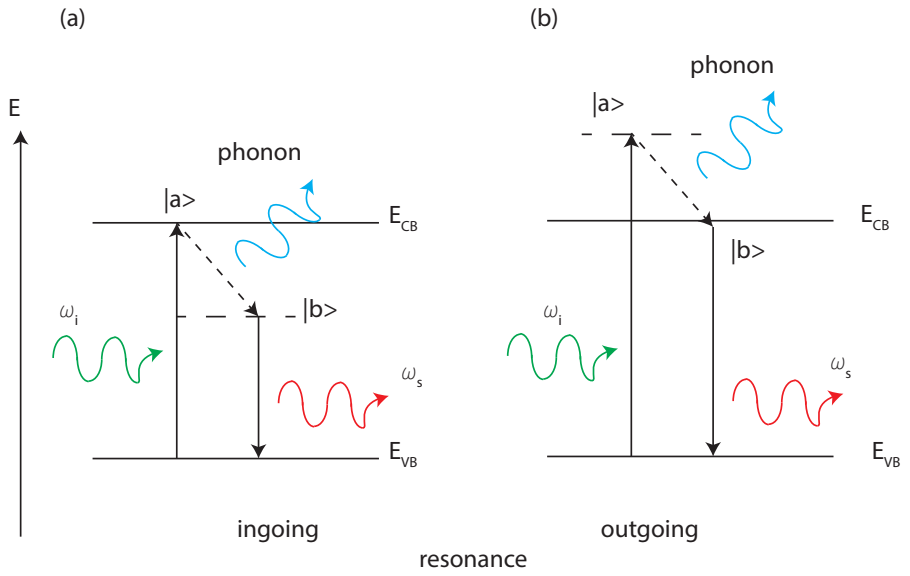

Figure 3.9 Scheme of resonant Raman process. (a) ingoing resonance (b) outgoing resonance

ments in Eq. (3.47) are constant and the wavevectors of the incident and scattered photon and of the phonon are negligible. The simplifications allow to write the dependence of the Raman scattering probability on the incident photon energy $\hbar\omega_i$ as [31]

$$w \propto \left(\frac{1}{\hbar\omega_0}\right)^2 \left|\frac{1}{E_a - \hbar\omega_i - i\Gamma_a} - \frac{1}{E_a - \hbar\omega_s - i\Gamma_a}\right|^2 . \tag{3.48}$$

Next we show, that resonant Raman scattering is interpreted as a modulation of the dielectric function with respect to the phonon energy. Therefore we use the the Dirac delta function

$$\delta(\omega) = \frac{1}{2\pi}\int_{-\infty}^{+\infty} e^{i\omega t} dt$$

and we get the following relation from Eq. (3.47):

$$\frac{1}{E_a(\boldsymbol{k}) - \hbar\omega_i - i\Gamma_a} = \frac{1}{E_a(\boldsymbol{k}) - \hbar\omega_i} + i\pi\delta[E_a(\boldsymbol{k}) - \hbar\omega_i] \tag{3.49}$$

Following Ref. [31] and Ref. [34] the dielectric function is given by:

$$\epsilon_i(\omega) = \frac{1}{4\pi\epsilon_0}\left(\frac{2\pi e}{m\omega}\right)^2 \sum_{\boldsymbol{k}} |P_{cv}|^2 \delta(E_{cv}(\boldsymbol{k}) - \hbar\omega) \tag{3.50}$$

$$\epsilon_r(\omega) = 1 + \frac{4\pi e^2}{4\pi\epsilon_0 m}\left[\sum_{\boldsymbol{k}}\left(\frac{2}{m\hbar E_{cv}}\right)\frac{|P_{cv}|^2}{E_{cv}^2 - \omega^2}\right], \tag{3.51}$$

where P_{cv} is a constant and ϵ_0 the dielectric constant. By comparing Eq. (3.49), Eq. (3.50) and Eq. (3.51) one can see that the imaginary part of Eq. (3.49) corresponds to the imaginary part of ϵ_i in Eq. (3.50). Assuming that the photon energy is close to the fundamental absorption edges ($E_{cv} = E_g + \hbar^2 k^2/2\mu$) we obtain the following relation:

$$w_{ph} \propto \left(\frac{1}{\hbar\omega_q}\right)^2 [\epsilon(\omega_i) - \epsilon(\omega_s)]^2 \tag{3.52}$$

If the phonon energy $\hbar\omega_q$ is much smaller then ω_i and ω_s then Eq. (3.52) can be rewritten as the first derivative of the dielectric function with respect to the energy:

$$w_{ph} \propto \left|\frac{\delta\epsilon}{\delta E}\right|^2 \tag{3.53}$$

This result shows that the resonant Raman scattering can be seen as a form of modulation spectroscopy. By using the macroscopic theory of Raman scattering, one can reach the same result. In the macroscopic picture the atomic vibrations modulate the electric susceptibility and thus the dielectric function at the phonon frequency. Assuming that the phonon frequency is smaller than the damping constant of the electrons the resulting oscillation at the phonon frequency is overdamped [31]. For this case $(\delta\chi_{ij}/\delta u)_0$ from the Raman tensor R can be regarded as a derivative of χ with respect to a static modulation u [31]. The Raman tensor R is proportional to $(\delta\chi/E_g)$ if an optical phonon of amplitude u changes the bandgap energy by δE_g. The dispersion of the Raman intensity is then proportional to $|\delta\chi/\delta E_g|^2$ or $|\delta\epsilon/\delta E_g|^2$ [31].

A further advantage of resonant Raman scattering on polar semiconductors such as GaAs is that not only the one LO phonon mode is enhanced, but also higher-order phonon modes shows a strong enhancement. An example for multi-phonon scattering in GaAs is shown in Fig. 3.10. The Raman spectra shows the 1LO phonon mode as well as higher order phonon modes. Leite *et al.* [66] demonstrate that under resonance conditions up to nine LO phonons appear in CdS. To describe the process we focus on a two-LO phonon excitonic scattering model, which has been established by Garciá-Cristóbal *et al.* [67]. In simple terms a photon excites

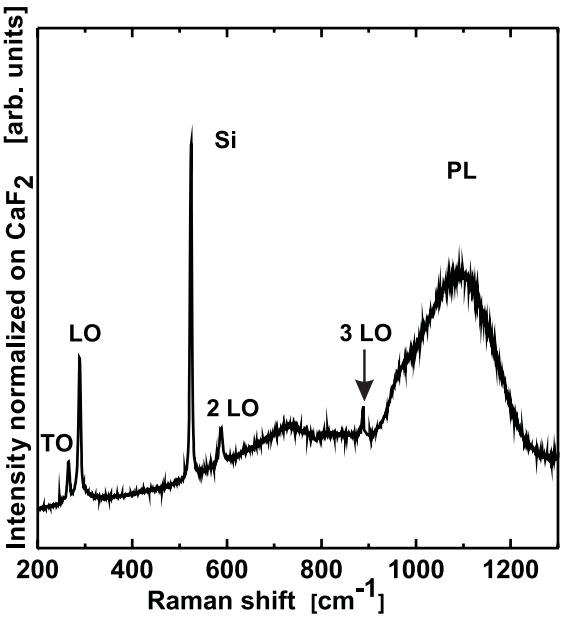

Figure 3.10 Exemplary Raman spectra of a wurtzite GaAs nanowire in resonance conditions. The phonon modes and the PL are marked.

an exciton on state $|\alpha\rangle$. The exciton relaxes then via two intermediate states ($|\beta\rangle$ and $|\gamma\rangle$), creating a LO phonon at each step [68]. The intermediate states can be continuous unbound (c) or discrete bound (d) excitonic states (see Fig. 3.11) [67,68]. The exciton recombines under emission of a scattered photon. The process is shown in Fig. 3.11. Note that all the states in the process in Fig. 3.11 are real except for the first and last one away from resonance.
Due to energy conservation within the process, the incident photon can be written as

$$E_{photon} = E_{exciton} + E_{2LO} \tag{3.54}$$

To give the scattering probability the intermediate state are considered as hydrogenic Wannier excitons and the dipole approximation is used [69]:

$$\begin{aligned} w_{fi} = \sum_{\alpha,\beta,\gamma} & \frac{\langle f|H_{er}|\gamma, K=0\rangle\langle\gamma, K=0|H_{el}|\beta, K=K_1\rangle}{(\hbar\omega_l - \hbar\omega_{2LO} - E_\gamma + i\Gamma_\gamma)} \\ & \times \frac{\langle\beta, K=K_1|H_{el}|\alpha, K=0\rangle\langle\alpha, K=0|H_{er}|i\rangle}{(\hbar\omega_l - \hbar\omega_{LO} - E_\beta + i\Gamma_\beta)(\hbar\omega_l - E_a + i\Gamma_\alpha)}, \end{aligned} \tag{3.55}$$

where $\hbar\omega_l$ is the laser energy and $E_{\alpha,\beta,\gamma}$ and $\Gamma_{\alpha,\beta,\gamma}$ are the energy and width of the corresponding states. The scattering intensity is given by

$$I_{2LO} \propto \sum_f |w_{fi}|^2 \tag{3.56}$$

For example the scattering efficiency for resonant Raman scattering from 2LO phonons at $E_0 + \Delta_0$ at 100 K for zincblende GaAs is shown in Fig. 3.12. As can be seen the above theoretical model for excitonic intermediate states describes the experimental data very well. In contrast using free electron-hole pairs (Fig. 3.12; dashed line) for the calculation, the theory does not describe the measurements. The above considerations show that resonant Raman scattering is a suitable method to determine the bandgap not only of wurtzite GaAs but also of

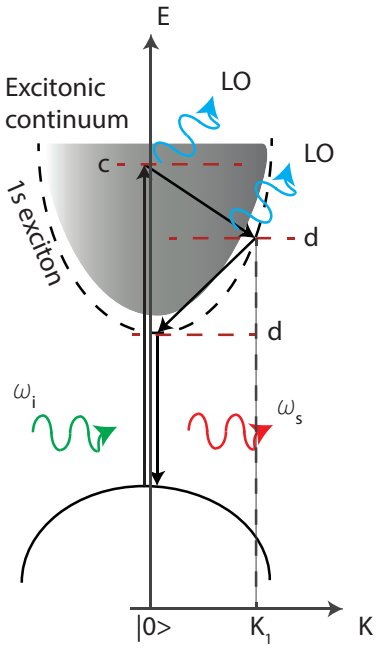

Figure 3.11 Scheme of a multiphonon resonant Raman process for a two LO phonon after Ref. [67]. 1. absorption of a photon and creation of an exciton. 2. subsequent emission of two LO phonons and relaxation of the exciton on the 1s excitonic state via two intermediate states. 3. emission of a Raman scattered photon by relaxation of the exciton on the ground state. Note: $E = \hbar^2 K^2((2M)$ with $M = m_e + m_h$ and K is the center-of-mass wavevector

novel materials or structures. By tuning the excitation energy, we can use the LO, TO and 2LO resonant Raman profiles to find the bandgap energy. Additionally we are able to gain information on the band structure by measuring the polarization dependence of the resonances.

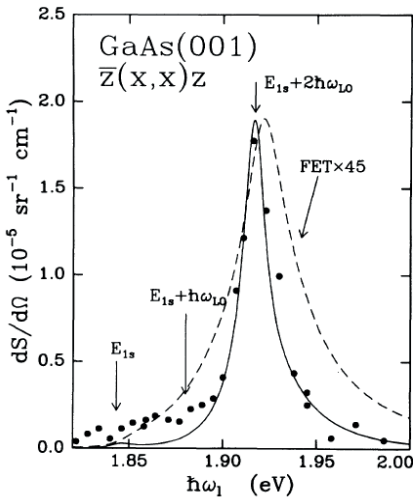

Figure 3.12 Resonant Raman profile for 2LO phonons at the $E_0 + \Delta_0$ band gap of zincblende GaAs adapted from Ref. [67]. The solid line is calculated taking into account excitonic effects. The dashed line is calculated using free electron-hole pairs as intermediate states.

4 | Experimental Requirements

4.1 Preparation of Zincblende GaAs Nanowires

The zincblende nanowires were grown by Steffen Breuer at the *Paul-Drude-Institut*, Berlin. Typically, nanowires are grown on a substrate by molecular beam epitaxy (MBE) using the vapor-liquid-solid (VLS) process. For the process one can use the Au-assisted or self-assisted VLS. Here the self-assisted VLS process is used to grow pure zincblende nanowires. A liquid Ga droplet, which act as a sink, was deposited on a Si waver. The growth species from the vapour phase is than collected by the Ga droplet [70]. The advantage of this method is that extrinsic defects from catalyst droplets are avoided [70, 71]. Additionally, instead of Au deposition and removing oxide the native oxide was left on the Si substrates to enable the formation of Ga droplets with appropriate dimensions [72]. A scheme of the self assisted VLS process is displayed in Fig. 4.1. A Si substrate with a thin SiO_x film is produced. While As is desorbed, Ga forms liquid droplets (see Fig. 4.1(b)), which are immobilized by existing or etched pinholes in the SiO_x film. The formed Ga droplets supersaturates with As and GaAs crystallize at the liquid solid interface, Fig. 4.1c [70]. In zincblende structure the nanowires grow along the [111] direction normal to the substrate. Depending on the growth condition, e.g. the beam flux of Ga and As and the growth temperature and time, the resulting wires vary in diameter and length.

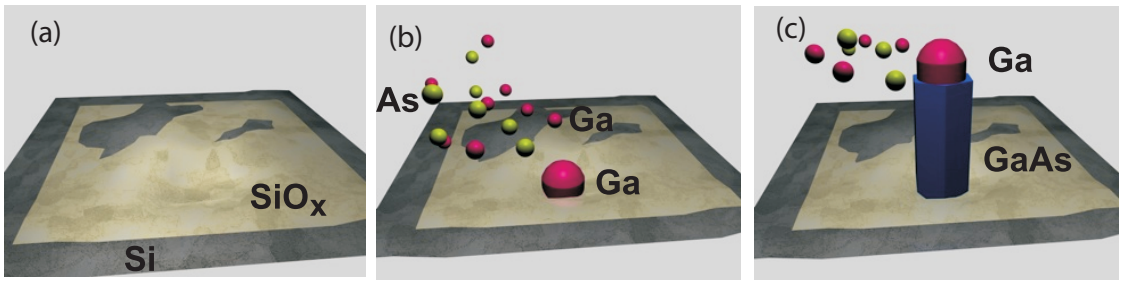

Figure 4.1 Scheme of the self-assisted VLS Growth of GaAs Nanowires: (a) Creation of the Ga droplets. (b) Collection of Ga and As at the Ga droplets. (c) Crystallization of Ga and As at the liquid solid interface.

The growth temperature was $580° C$. (for details, see Ref. [72]). The resulting nanowires have a high phase purity and average diameters of 60 nm. In Fig. 4.2 we show scanning electron microscopy (SEM) micrographs of the zincblende nanowires used in this work as a reference sample. The nanowires were grown vertically to the substrate and, in contrast to the Au-assisted grown nanowires, they have a Ga droplet at the top. The SEM images shows parasitic islands and tilted structures between the bottom ends of nanowires

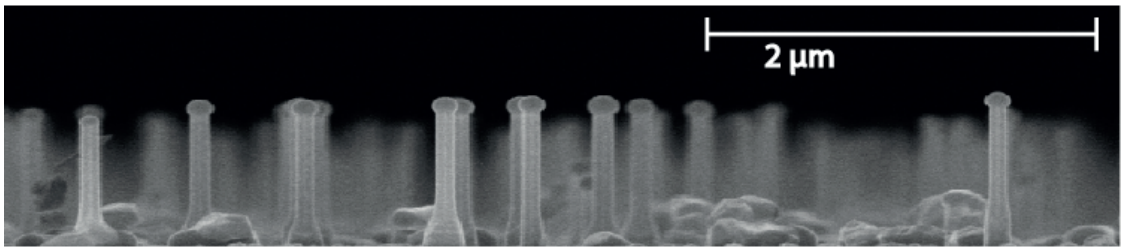

Figure 4.2 SEM micrograph of zincblende GaAs nanowires as-grown on Si substrate with 60 nm diameter.

For the Raman experiments on single GaAs nanowires, we used a micro-Raman setup. In order to measure single wires we had to remove the wires form the growth substrate and deposited them on a Si substrate with markers (markers

allow to identify the wire at different optical experimental setups). To remove the wires from the growth substrate, the substrate was ultrasonicated in 400 μl ethanol and then the solution was dispersed on the Si substrate. In order to realize separated nanowires on the substrate for single-nanowire experiments, the solution was diluted.

4.2 Preparation of Wurtzite GaAs Nanowires

The wurtzite GaAs nanowires were also grown at the *Paul-Drude Institut* by S. Breuer and C. Somaschini on Si(111) by MBE using the VLS process. For wurtzite GaAs nanowire with a high phase purity the Au-assisted VLS process is used. Simplified, a liquid metal droplet, which act as a sink, was grown on a Si waver. The growth species from the vapour phase is then collected by the metal droplet [70]. The process is schematically displayed in Fig. 4.3. As can be seen in the first step an Au droplets are created by deposition of a thin Au film on a Si waver and subsequent annealing. The Au droplets collect the Ga and As, which are supplied from the vapour phase [see, Fig. 4.3(b)]. Due to the supersaturation of the Au droplets, the growth species (Ga and As) crystallize at the liquid solid interface.

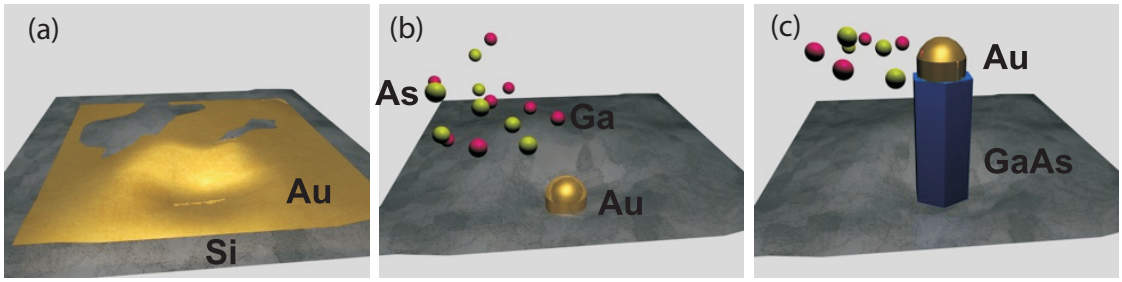

Figure 4.3 Scheme of the Au-assisted VLS Growth of GaAs Nanowires: (a) Creation of the Au droplets. (b) Collection of Ga and As at the Au droplets. (c) Crystallization of Ga and As at the liquid solid interface.

An oxide-free Si (111) wafer was loaded into the MBE and anealed at $500° C$ for the growth of wurtzite GaAs nanowires. They grew along the [0001] direction and normal to the substrate. A detailed description is given in Ref. [73]. On average, the nanowires have a diameter of 50 nm and a length of $2.2\,\mu$m as can be seen in Fig. 4.4. Wurtzite nanowires taken from the identical sample were already analyzed by photoluminescence, X-ray diffraction, and cathodoluminescence [29].

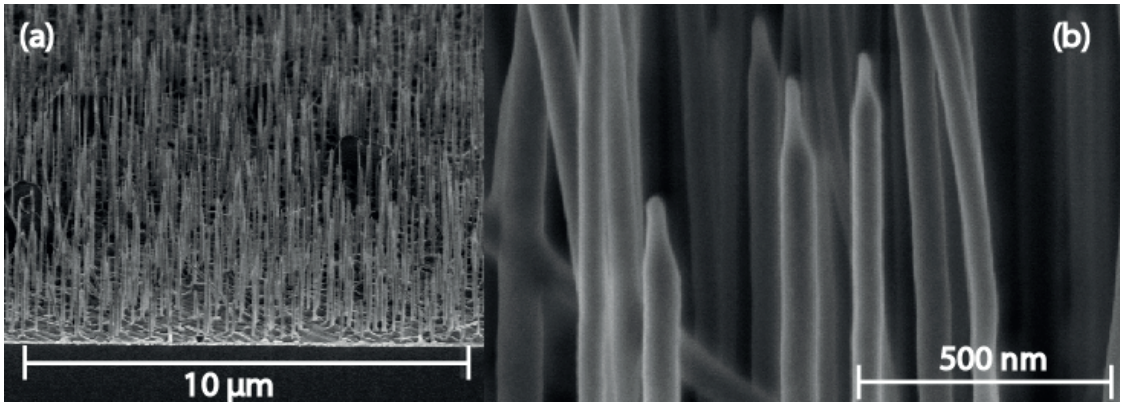

Figure 4.4 (a) SEM micrograph of wurtzite GaAs nanowires as-grown on Si substrate with 50 nm diameter in side view. (b) Magnification of the top region, which indicates a tapering of the tip. Kindly provided by the *Paul-Drude-Institut*

As mentioned in the introduction the influence of zincblende insertions and stacking faults are an explanation for the observation of different bandgap energies for wurtzite GaAs, especially measured by photoluminescene (PL) experiments. Therefore we study wurtzite GaAs nanowires with isolated zincblende insertions and stacking faults. In Fig. 4.5 we show SEM micrographs of the "thicker" wurtzite nanowires with zincblende insertions. The nanowires grow vertically to the substrate and are tapered in the top region. They are pencil-shaped at their very top and have an average diameter of around 200 nm in the middle part. At the bottom the nanowires have a diameter of around 100 nm and they exhibit a length of 10 μm. However, shape and size of the nanowires were found to vary; mainly, we observed a maximum of 220 nm and a minimum of 120 nm for the diameter in the middle part of the wire, but some wires also show diameters below 50 nm. These nanowires were also grown by molecular beam epitaxy (MBE) directly on a Si (111) substrate, using the Au-assisted VLS process. They were annealed at around 630 °C for 20 minutes before the Au deposition. A 0.6 nm thick layer of Au was deposited in the growth chamber at 500 °C and annealed for 10 minutes under As flux at the same temperature. By opening the Ga shutter the growth process was started, with a beam flux of 400 nm/h for planar GaAs growth on GaAs (001) substrates.

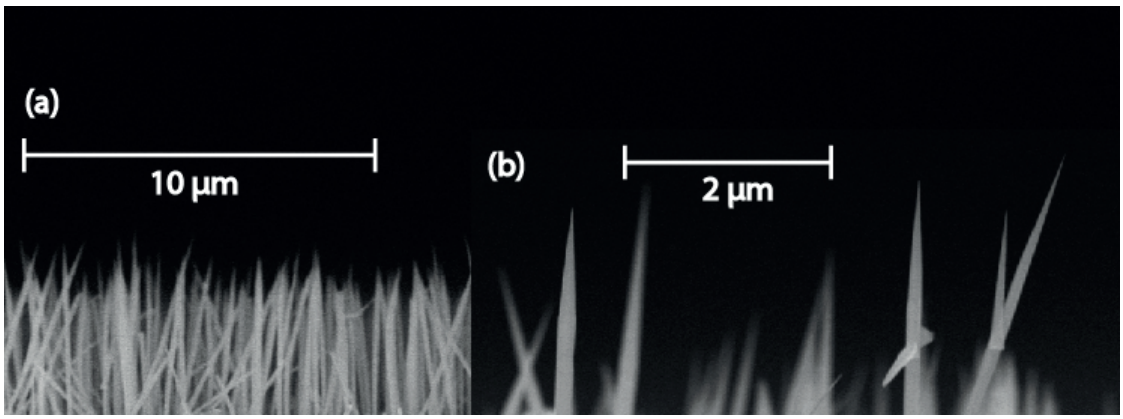

Figure 4.5 (a) SEM micrograph of wurtzite GaAs nanowires as-grown on Si substrate with 200 nm diameter in side view. (b) Magnification of the top region, which indicates a tapering of the tip. Kindly provided by the *Paul-Drude-Institut*

The growth time was two hours, the V/III ratio is two. Similar growth conditions lead to high quality GaAs NWs with predominant wurtzite crystal phase. [29,73,74]. The growth temperature of 500°C was kept for one hour. Then it was reduced to 360 °C without any growth disruption. Ramping down the temperature and the growth at lower temperatures increase the radial growth rate and produce nanowires with larger diameters, which enable an easier spectroscopic investigations on single, dispersed nanowires.

For the Raman experiments the nanowires have to be removed from the growth substrate. To remove the wires from the growth substrate and for deposition on a substrate, we use the same technique as described before for the zincblende nanowires. After deposition we performed position dependent Raman experiments and took AFM images of nanowires for a first characterization. The AFM images were taken by a Park AFM. The position dependent Raman experiments were performed on a Horiba XploRar with piezo XYZ stage. The AFM measurements of the wurtzite nanowires used for the resonant Raman and PL experiments are shown in Fig. 4.6(a) and (c). From the linescan along the wire axis [Fig. 4.6(b)]

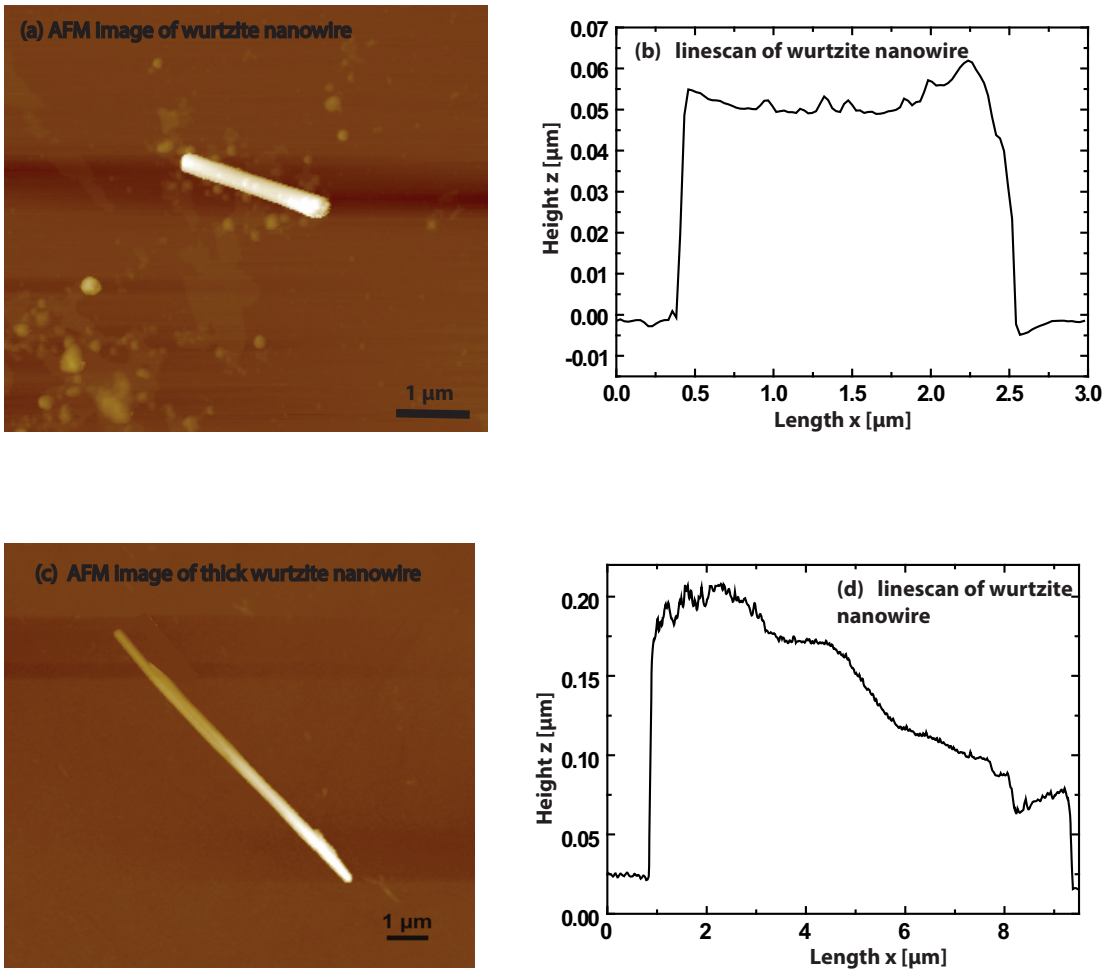

Figure 4.6 (a) AFM image of a wurtzite GaAs nanowire with a diameter of around 60 nm. (b) linescan of the wurtzite GaAs nanowire. (c) AFM image of a wurtzite GaAs nanowire with a diameter of around 150 nm in the middle part. (d) linescan of the "thicker" wurtzite GaAs nanowire.

we obtain for the wire length 2.2 μm. and for the diameter 55 nm. The linescan of the "thicker" wire [Fig. 4.6(d)] shows that the nanowire has an average diameter of 200 nm at the bottom, of around 150 nm at the middle part and is pencil-shaped at their very top and exhibit a length of 8.5 μm.

4.3 Experimental Setup

The intensity of Raman scattered light is very low compared to the intensity of incident light. It is crucial to fulfill several experimental requirements in order to receive suitable Raman spectra:. The light source has to be bright and monochromatic with a narrow linewidth, else the elastically scattered light (10^6 times stronger than the inelastic scattered light) outshines the Raman scattered light. Additionally, the light source needs to be tunable in order to excite the wires at different energies. A tunable continuous-wave laser with a narrow linewidth fulfill these conditions. Here a Ti:sapphire-ring-laser system was used (*Coherent MBR-110*). To suppress the Rayleigh scattered light and the detection two monochromators in subtractive mode, that act as a bandpass for the Raman signal, and a Si charged coupled device (CCD) were used. A scheme of the setup is shown in Fig. 4.7.

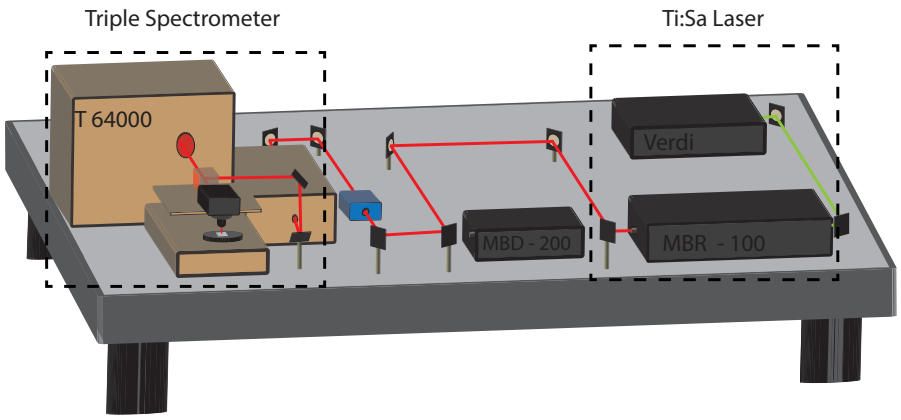

Figure 4.7 Setup for resonance Raman experiments on single GaAs nanowires.

The setup consists of a fully tunable Ti:sapphire laser with an emission range form 690 nm to 1050 nm. The laser is pumped by a 18 W Verdi V-18 diode neodymium-vanadate laser. Additionally, we have the possibility to double the frequency with

the MBD-200 using a nonlinear crystal. [75]. For the nonlinear optical process, called second harmonic generation (SHG), the laser beam was focused on the SHG crystal (here: Lithium Triborate; LBO). The laser beam travelled through the nonlinear medium and its frequency was doubled (for details see Ref. [75]). Thus a second emission range from 425 nm to 480 nm is available for excitation. The peculiarity in this setup is that the frequency doubler is pumped by a continuous wave (cw) laser. Typically pulsed lasers are used.
A small premonochromator in the setup cuts off possible plasma lines.
A Horiba T64000 triple monochromator system with a motorized XY stage was used as Raman system. A scheme is displayed in Fig. 4.8.

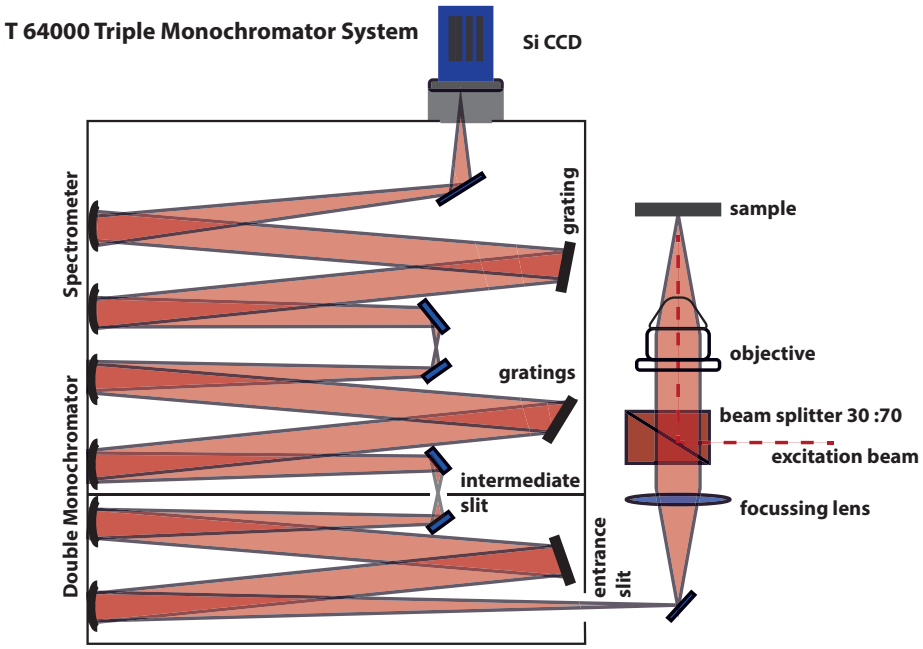

Figure 4.8 Scheme of a triple monochromator system for Raman experiments

The laser light enters the system and is guided through a beamsplitter and an 100x objective onto the sample. The backscattered light is collected by the objective

and directed towards the triple monochromator. The double monochromator acts as band-pass for the inelastic scattered light and cuts off the Rayleigh scattered light. The third monochromator is the spectrometer and images the Raman spectrum on the Si CCD. The stray light rejection of 10^{-14} allows to measure Raman peaks very close to the Rayleigh scattered light. All measurements were performed in backscattering configuration and at a constant laserpower of 3.5 mW. The position of the laser spot on the nanowire was controlled by a motorized XY stage.

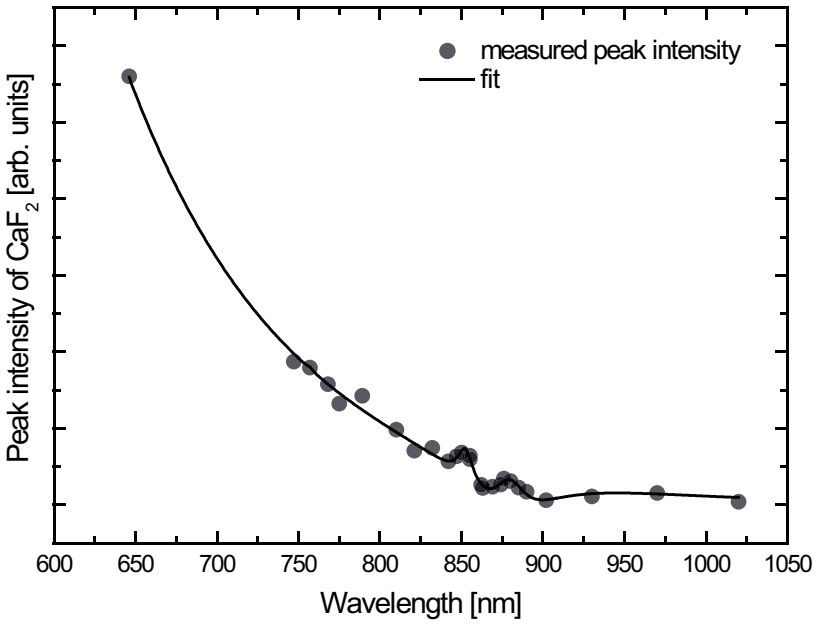

Figure 4.9 Calibration curve for the T64000. Measured phonon mode intensity of a CaF_2 crystal depending of emission wavelength. Note, the intensity of the phonon mode is independent of excitation wavelength for CaF_2

In the resonance experiments the peak intensity depending of excitation wavelength (energy) was measured. Therefore we had to tune the excitation wavelength. The T64000 consists of different optical elements and of gratings which

are optimized for a certain wavelength. Thus, the sensitivity (and consequently the measured intensity) of the system is strongly dependent of the wavelength of the incident light and scattered light (see Fig. 4.9). By that the intensity of the measured phonon modes was calibrated using a CaF_2 crystal. CaF_2 has the advantage that the intensity of its Raman active phonon (at $322\,cm^{-1}$) is independent of excitation wavelength. The Raman peaks were fitted by Lorentzians and the intensities were determined by peak area integration.
For measurements in the visible range an Ar^+-laser as excitation with various lines between 454 nm and 657 nm and a Dilor-XY triple-monochromator as Raman system were used. Its operation is very similar to the T64000.

5 | Polarization-Dependent Raman Experiments on GaAs Nanowires

5.1 Raman Selection Rules of Zincblende Nanowires

For the polarization-dependent measurements a Fresnel rhomb (FR), a half-wave plate ($\lambda/2$) and an analyzer (A) were installed in the laser path, Fig. 5.1. The incoming light with polarization direction e_i passes a Fresnel rhomb rotating the light to parallel $e_\parallel$ or to perpendicular $e_\perp$ polarization. The light passes a beam splitter (BS) (70 : 30). Because the transmission of the beam splitter is polarization dependent, we determined the laser power after rotating the light from $e_\parallel$ to $e_\perp$. The half-wave plate rotates the incoming light e_i' by an angle Φ. The scattered light e_s passes again the half-wave plate, which rotates the polarization back. In front of the monochromator entrance is an analyzer, which selects the vertical component of the scattered light. The advantage of the setup is that it allows selecting any scattering geometry without putting or removing elements in the light path or rotating the sample. To confirm that the setup works properly, we start with polarization dependent experiments on bulk GaAs[100]. The selection rules for bulk GaAs[100] are calculated by Eq. (3.26), using the Raman tensor

from Eq. (3.27) and are summarized in Tab. 5.1. As the TO phonon is completely forbidden we measure the angular variation of the intensity of the LO phonon mode (Fig. 5.2).

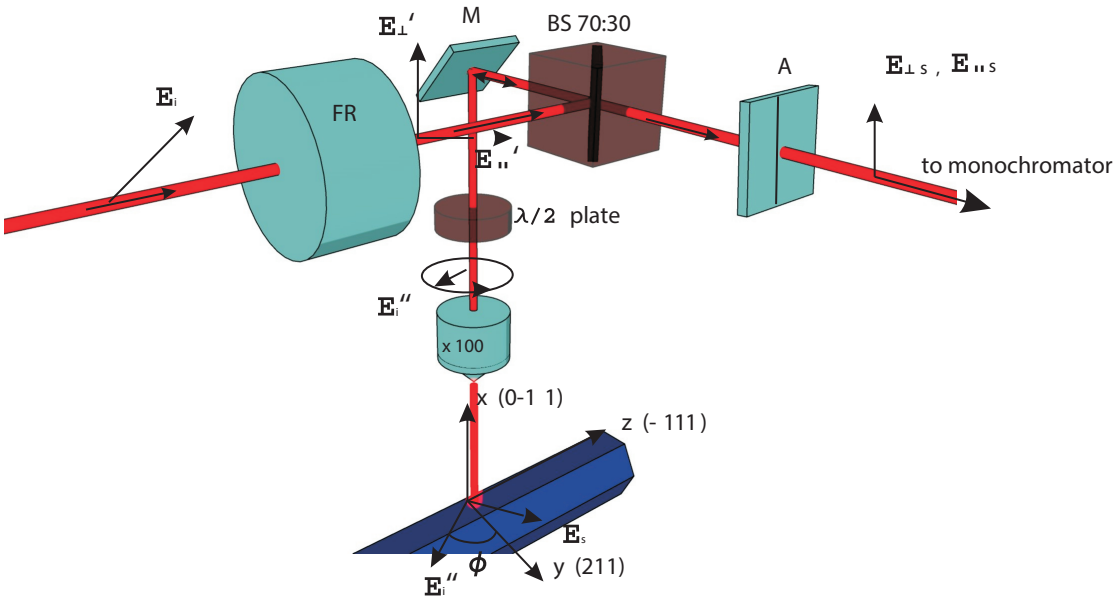

Figure 5.1 Scheme of the setup for polarization dependent Raman experiments.

To calculate the theoretical azimuthal dependence of the LO mode we use Eq. (3.26). For the parallel configuration we use

$$e_i = e_s = \begin{pmatrix} 0 \\ cos[a] \\ sin[a] \end{pmatrix} \tag{5.1}$$

and for perpendicular configuration

$$e_i = \begin{pmatrix} 0 \\ cos[a] \\ sin[a] \end{pmatrix}, \; e_s = \begin{pmatrix} 0 \\ -sin[a] \\ cos[a]. \end{pmatrix} \tag{5.2}$$

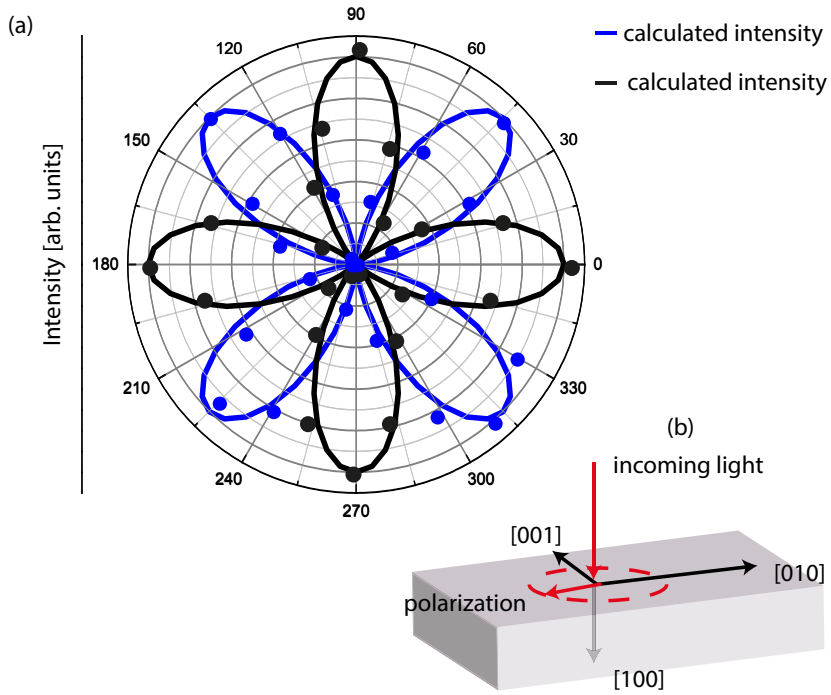

Figure 5.2 (a) Calculated (solid lines) and measured (dots) Azimuthal dependence of the LO phonon intensity for $e_i \| e_s$ (blue) and $e_i \perp e_s$ (black). (b) Scheme of the scattering configuration.

Figure 5.2 shows the comparison of measured (dots) and calculated (solid lines) azimuthal dependance of the LO phonon intensity. The measurements and the calculations are in excellent agreement verifying that the setup is working properly. The nanowires have a different set of axis. Therefore we calculated the selection rules with respect to the wire axis following Eq. (3.26). The Raman selection rules for zincblende GaAs nanowires are shown in Tab. 5.2. In order to calculate the azimuthal dependence of the LO and TO phonon we have to take into account, that each Raman tensor in Eq. (3.27) represents one coordinate axis, namely $x = [100]$, $y = [010]$ and $z = [001]$. Thus we have to transform the Raman tensors with respect to the wire axis: $x' := [0\bar{1}1]$, the y-axis is $y' := [211]$ and $z' := [\bar{1}11]$. For

Table 5.1 Raman selection rules for backscattering geometries in zincblende bulk GaAs on the [100] surface . d_{LO} denotes the non-zero Raman tensor elements for the LO phonon. Note: the TO phonon is forbidden.

INCIDENT POLARIZATION e_i	SCATTERED POLARIZATION e_s	RAMAN INTENSITY
[001]	[001]	0
[001]	[010]	$d^2(LO)$
[010]	[010]	0
[01$\bar{1}$]	[01$\bar{1}$]	$d^2(LO)$
[01$\bar{1}$]	[0$\bar{1}$1]	0

the transformation we use the following rotation matrix:

$$T = \begin{pmatrix} 0 & \frac{-1}{\sqrt{2}} & \frac{1}{\sqrt{2}} \\ \frac{2}{\sqrt{6}} & \frac{1}{\sqrt{6}} & \frac{1}{\sqrt{6}} \\ \frac{-1}{\sqrt{3}} & \frac{1}{\sqrt{3}} & \frac{1}{\sqrt{3}} \end{pmatrix}. \tag{5.3}$$

Then we calculate the transformed rotation tensors with

$$R'(x,y,z) = TR(x,y,z)T^{-1}. \tag{5.4}$$

The transformed Raman tensors are:

$$R'(X) = \frac{1}{3\sqrt{2}} \begin{pmatrix} -4d & d & d \\ d & 2d & 2d \\ d & 2d & 2d \end{pmatrix}, \; R'(Y) = \frac{1}{\sqrt{6}} \begin{pmatrix} 0 & d & -d \\ d & -2d & 0 \\ -d & 0 & 2d \end{pmatrix},$$

$$R'(Z) = \frac{1}{\sqrt{3}} \begin{pmatrix} 0 & -d & d \\ -d & -d & 0 \\ d & 0 & d \end{pmatrix}$$

In order to compare the measured and calculated LO and TO intensities for different scattering configuration, we take Raman spectra in the same scattering

Table 5.2 Raman selection rules for backscattering geometries for zincblende nanowires . d_{LO} denotes the non-zero Raman tensor elements for the LO phonon. Note: the TO phonon is forbidden.

SCATTERING CONFIGURATION	ALLOWED PHONON MODES
$x(z,z)\overline{x}$	$8/9d^2(TO) + 2/9d^2(LO)$
$x(y,y)\overline{x}$	$8/9d^2(TO) + 2/9d^2(LO)$
$x(z,y)\overline{x}$	$2/9d^2(LO)$
$x(y,z)\overline{x}$	$2/9d^2(LO)$

geometry as shown in Tab. 5.2. The spectra are displayed in Fig. 5.3. As can be seen in Fig. 5.3 the measurements do not correspond with the selection rules shown in Tab. 5.2.

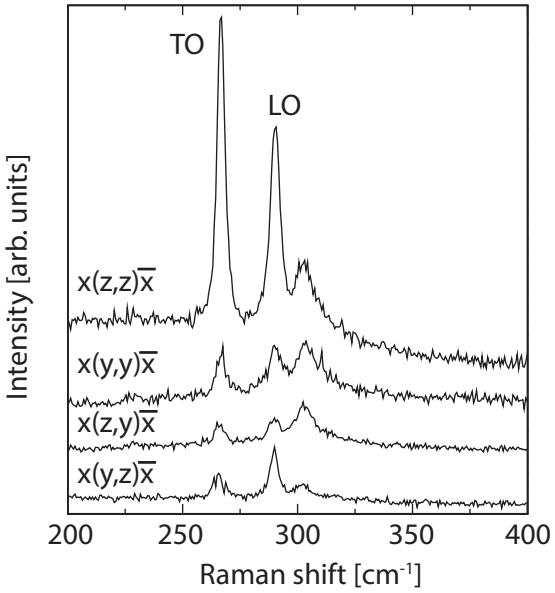

Figure 5.3 Raman spectra of a single GaAs nanowires at different scattering configurations at 1.722 eV excitation

The main differences are:

- for $x(z,z)\overline{x}$ the TO phonon mode intensity is not stronger than the LO phonon intensity
- for $x(y,y)\overline{x}$ configuration we do observe a very weak TO phonon mode
- for $x(y,z)\overline{x}$ and $x,(z,y)\overline{x}$ configuration the LO phonon intensity should be the same.

Applying Eq. (3.26) on the transformed Raman tensors we calculate the azimuthal dependance of the zincblende GaAs nanowire, with respect to wire axis, in the same way as have been done for bulk GaAs before. Figure 5.4 shows the calculated intensity of the TO [Fig. 5.4(a)] and the LO [Fig. 5.4(b)]as a function of the angle Φ from Fig. 5.1. To be able to compare the calculated azimuthal dependance shown in Fig. 5.4 we measure the azimuthal dependance of the LO and TO phonon in parallel and perpendicular configuration. The measurements are shown in Fig. 5.5. The polarization dependent measurements show that the measured azimuthal dependance of the TO and LO intensity is in clear disagreement with the calculated azimuthal dependance of the TO (LO) phonon intensity in Fig. 5.4. These effect has been measured in a lot of different studies [76–84]. It has been found, that nanowires with diameters $d < \lambda$, where λ is the excitation wavelength, show a dipolar anisotropy [76,84]. This means that the Raman intensity is only enhanced along the wire c-axis in parallel configuration (Fig. 5.5). Additionally in $x(y,y)\overline{x}$ configuration (incident light is perpendicular to the wire axis) the Raman intensity is suppressed. The transmission of the electric field, at air/wire interface, is strongly dependent of the angle between incident light and wire c-axis [76]. The resulting effect is: when the light is neither polarized along nor perpendicular to the wire axis, the angle Φ (Fig. 5.1) is not preserved during transmission at the interface [76].

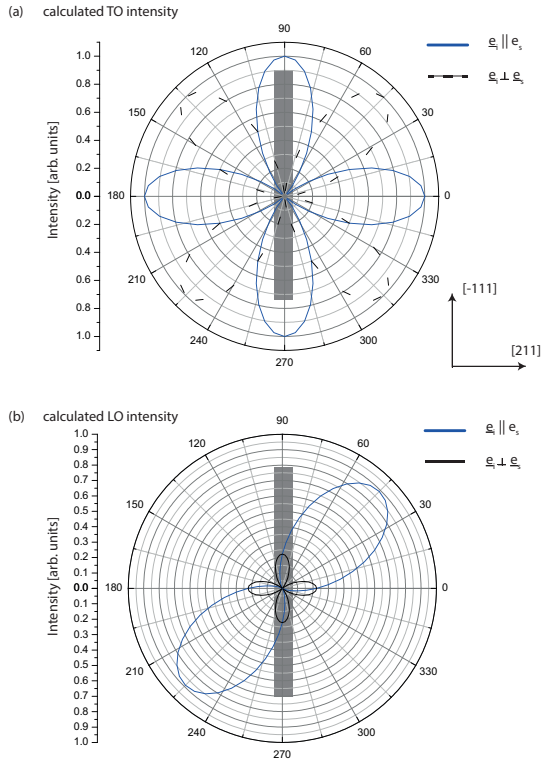

Figure 5.4 Calculated Azimuthal dependence of the TO (a) and LO (b) phonon for $e_i \| e_s$ and $e_i \perp e_s$. The wire position is indicated as gray rectangle.

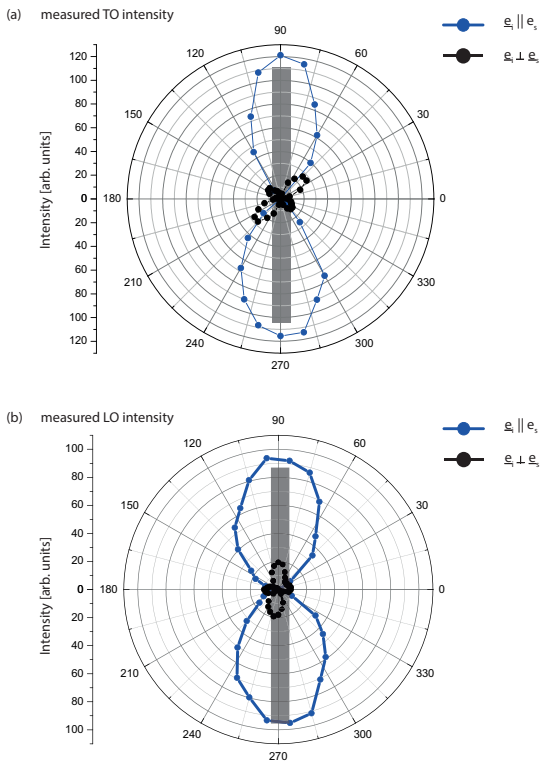

Figure 5.5 Measured Azimuthal dependence of the TO (a) and LO (b) phonon for $e_i \| e_s$ and $e_i \perp e_s$. The wire position is indicated as gray rectangle.

Following Ramsteiner *et al.* [28] the ratio between the Raman intensity measured with light polarized perpendicular and parallel to the wire axis is 1 to 10 at an excitation energy of 1.7 eV. To consider this behaviour in our calculations of the azimuthal dependence of the TO and LO phonon we set

$$e_i = e_s = \begin{pmatrix} 0 \\ cos[a] \\ 0.1sin[a]. \end{pmatrix} \tag{5.5}$$

Figure 5.6 shows the measured azimuthal dependence of the TO and LO phonon, as well as, the calculated dependence by using Eq. (3.26), scaled by a factor. The measurements and the calculation are in great agreement.

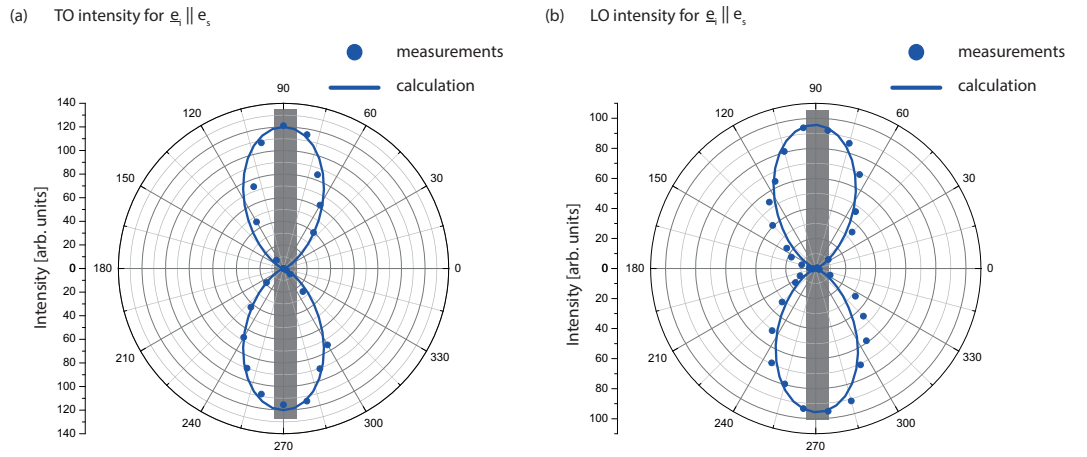

Figure 5.6 Measured and calculated Azimuthal dependence of the TO (a) and LO (b) phonon for $e_i \| e_s$. The wire position is indicated as gray rectangle.

In contrast looking at the measurements for crossed polarization ($e_i \perp e_s$), see Fig. 5.7, the measured azimuthal dependence of the LO and TO phonon is still in disagreement with the calculation (compare Fig.5.4 and Fig. 5.7).

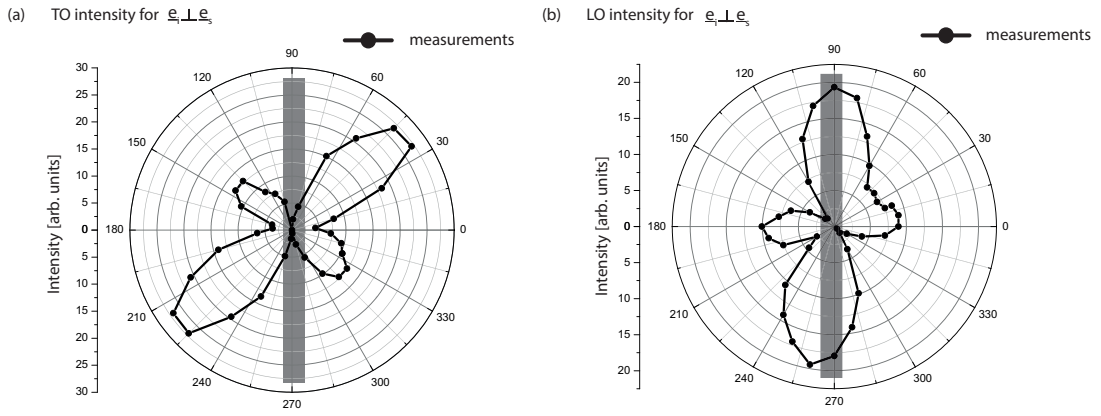

Figure 5.7 Measured Azimuthal dependence of the TO (a) and LO (b) phonon for $e_i \perp e_s$. The wire position is indicated as gray rectangle.

The effect of the dipolar anisotropy causes that the angle between wire and incident light outside of the wire is no longer preserved inside the wire for $e_i \perp e_s$ configuration [76]. Thus, the Raman intensity of the TO and LO phonon is strongly decreased [76]. But the shape of the azimuthal dependence should be symmetric for the TO and LO phonon. This is not the case, see Fig.5.7. In literature there are some studies, which try to explain this behaviour by the fact that incident light and scattered light are not parallel, see Fig. 5.8 [85, 86]. The measurements were performed on InAs [86] and GaP [85] nanowires. To describe their results they introduce a rotation matrix S.

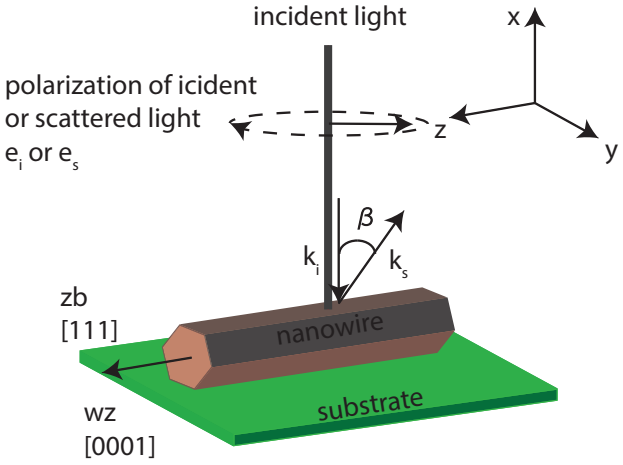

Figure 5.8 Scheme of the backscattering configuration used for polarization dependent Raman experiments. The arrows indicates the incident and scattered light.

The matrix S represents the rotation about the nanowire axis z by an angle β.

$$S = \begin{pmatrix} cos(\beta) & -sin(\beta) & 0 \\ sin(\beta) & cos(\beta) & 0 \\ 0 & 0 & 1 \end{pmatrix} \tag{5.6}$$

The matrix S is multiplied by the transformed Raman tensors R'. As result, dependent of the angle β, it is possible to calculated different patterns, see Fig. 5.9.

Applying these consideration on our measurements it is possible to to calculate the asymmetric shape of the azimuthal dependence by using Eq. (3.26) and an angle β. The angle β should be the same for $e_i \perp e_s$ and for $e_i \| e_s$ configuration. This is not the case. To reproduce our measurements we found for $e_i \perp e_s$ configuration an angle of $\beta = 16$ and for $e_i \| e_s$ configuration an angle of $\beta = 87$. Thus the explanation is not satisfying and should not be used to describe the asymmetric shape in $e_i \perp e_s$ configuration. Unfortunately we do not find any plausible explanation for the

measured azimuthal dependence. In our opinion it is necessary to perform further polarization-dependent measurements, to understand and explain the observation for the TO and LO phonon. To study the effect of the dipolar anisotropy the measurement should be performed with nanowires with larger diameters and at different excitation wavelengths. Additionally our experiments show that Raman, especially polarized Raman experiments on nanowires, have to be performed with great care.

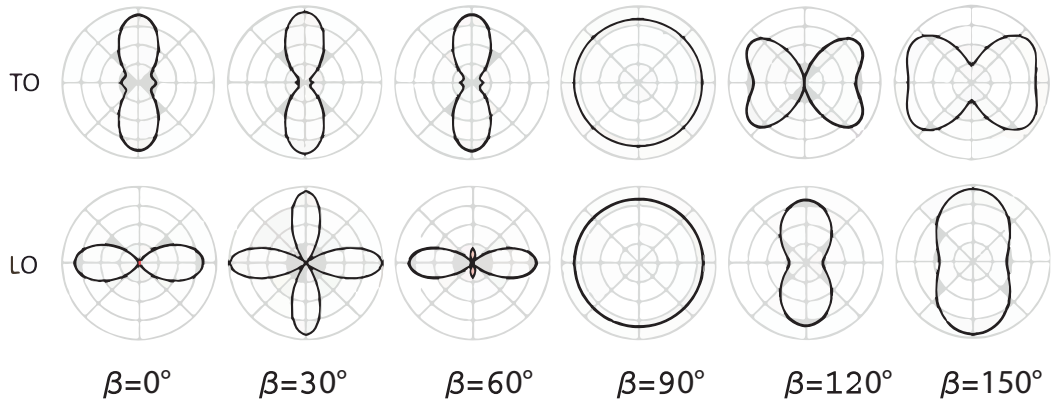

Figure 5.9 Calculated β dependence of the contribution to the backscattered Raman intensity for a (110) GaP nanowire according to Eq. (3.26), adapted from Ref. [85]

5.2 The E_2^H Phonon Mode in Wurtzite GaAs Nanowires

The wurtzite structure of GaAs shows, additionally to the TO and LO phonon modes, the E_2^H phonon mode. Thus Raman scattering on wurtzite GaAs nanowires can be used as an fingerprint of wurtzite crystal structure [87]. However, the observation of the E_2^H phonon line is strongly dependent of the polarization of the incident laser light. It is only observable for incoming light polarized perpendicular to the wire axis [87], for nanowires grown along the *c*-direction. Beside that when the nanowire radius-to-wavelength ratio decreases below a certain value, the optical transmission through the nanowire side facets is vanished and the E_2^H phonon line is not measurable [88, 89].
In order to study this behaviour we performed energy (wavelength) dependent Raman scattering on single wurtzite and as-grown GaAs nanowires with diameters around 50 nm. Figure 5.10 shows Raman spectra at different excitation wavelengths taken on as-grown GaAs nanowires. The spectra show the TO and LO phonon modes. Additionally, at an excitation of 439 nm, a strong E_2^H phonon mode is observable. However, when the excitation wavelength is increased to 461 nm or 568 nm the E_2^H phonon mode is quenched.
Taking Raman spectra on single GaAs nanowires, with light polarized perpendicular to the wire c-axis (TE polarization) and at an excitation wavelength of 568 nm, the quenching of the E_2^H phonon mode is complete (Fig. 5.11). As shown by Ramsteiner *et al.* [28], light enters and leaves the nanowire mainly through its side facets with wavevectors perpendicular to the nanowire's c-axis [90, 91]. Thus, the scattering geometry is similar for the measurements on the nanowire ensemble. In order to measure the E_2^H phonon mode the incoming light have to be polarized perpendicular to the wire axis. Moreover, depending of the wavelength of incident light, the transmission through the side facets of the nanowire decrease or increase [28]. This leads to the quenching of the E_2^H phonon mode above a certain excitation wavelength [28].

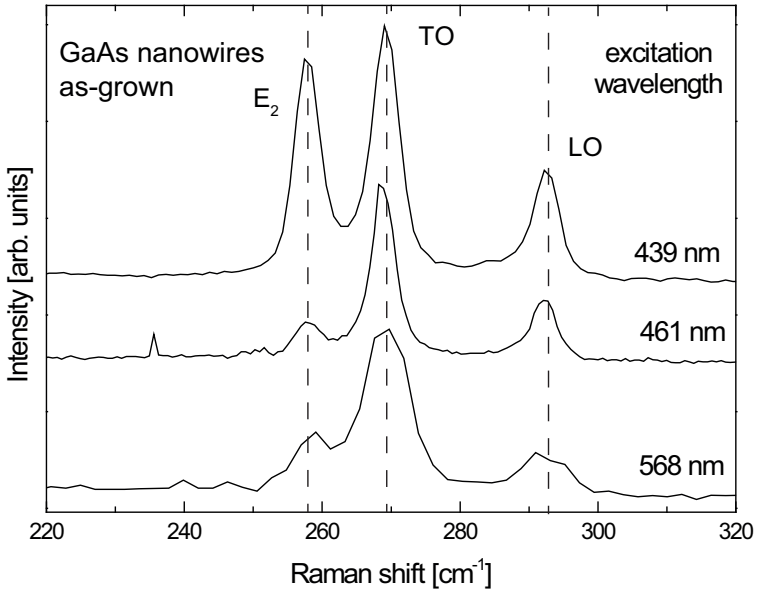

Figure 5.10 Raman spectra of an ensemble of GaAs nanowires as-grown at different excitation wavelengths with 50 nm diameter and 2.2 μm length.

To demonstrate this behaviour we perform Raman experiments at different excitation wavelengths on the nanowire ensemble. Following the selection rules for Raman scattering [27], for light polarized along the wire c-axis and backscattering through the side facets of the wire (TM polarization), only scattering by TO phonons is allowed [Fig. 5.11(b)] [28]. Thus, the ratio between the TO and E_2^H intensity reflects the TE/TM ratio and hence the optical extinction in nanowires. The E_2^H/TO intensity ratio is shown in Fig 5.12. Additionally, we show the ratio between the TE and TM, calculated by Ramsteiner *et al.* [28] (Fig. 5.12 solid line) for nanowires with a radii of 22 nm. As can be easily seen, the calculated curve is in great agreement with the measured data. Hence, the quenching of the E_2^H phonon is due to the vanishing optical transmission of TE polarized light near 650 nm excitation wavelength.

A second explanation is an antiresonance in the scattering efficiency observed for bulk wurtzite CdS reported in Ref. [92]. But this explanation can not be used for our observation, because measurements on wurtzite GaAs nanoneedles with radii of 500 nm exhibits an E_2^H phonon peak up to an excitation wavelength of 825 nm. In contrast we do not observe an E_2^H phonon mode between 700 and 900 nm for

wurtzite GaAs nanowires with radii of 25 nm in the Raman spectra. The transmission of TE polarized light is suppressed by the strong dielectric contrast, as shown in Ref. [28].

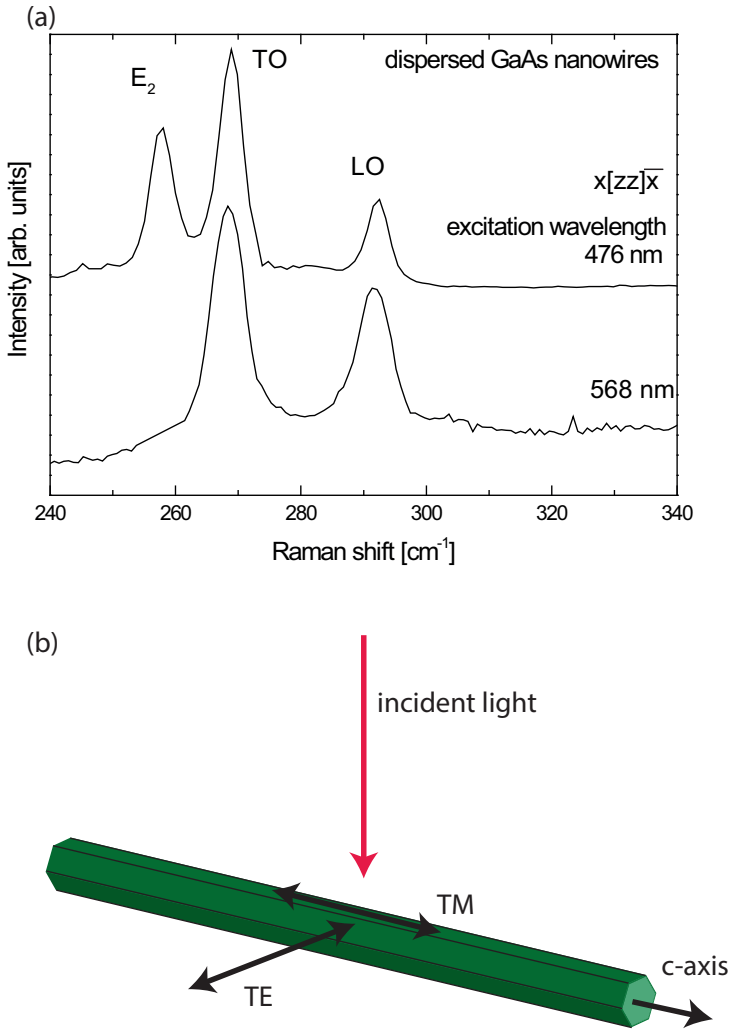

Figure 5.11 (a) Raman spectra of a single wurtzite GaAs nanowire dispersed on a Si substrate at different excitation wavelengths and light polarized perpendicular to the wire c-axis. (b) Scheme of the scattering geometry.

As a result the possibility of using Raman scattering to detect wurtzite GaAs by the E_2^H phonon strongly depend of the radii of the nanowires and the excitation wavelengths.

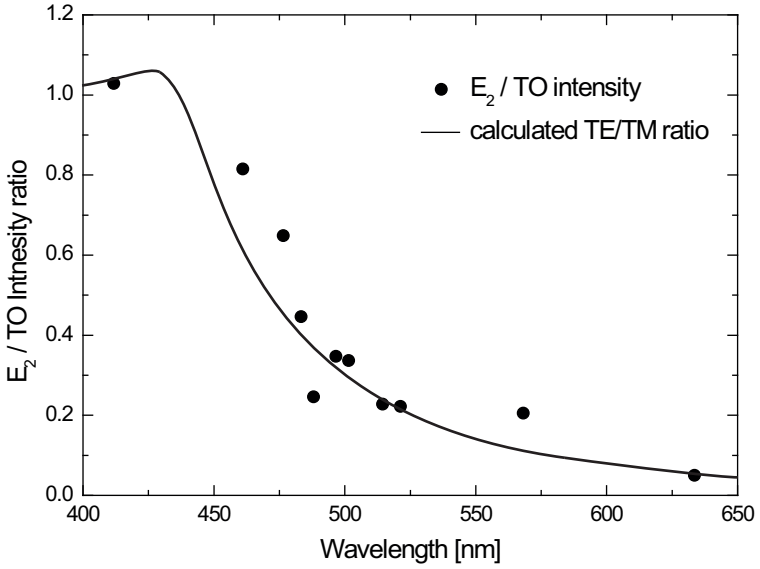

Figure 5.12 Intensity of the E_2^H phonon mode normalized on the TO phonon mode intensity. The calculated curve for the ratio between TE and TM is taken form ref. [28] and scaled by a factor of 1.85 to take into account the different scattering efficiencies for E_2^H and TO phonons

6 | Resonant Raman Experiments on GaAs Nanowires

6.1 Resonant Raman Experiments on Zincblende Nanowires

Before we start to investigate the bandgap of wurtzite GaAs nanowires, we have to characterize the zincblende nanowire, which we use as a reference sample. As the nanowires have a diameter of 60 nm, we have to confirm that the small diameter do not influence the resonant Raman experiments. Therefore we start with resonant Raman experiments on the zincblende nanowires. In the resonant Raman experiments we measure the TO and LO phonon mode intensity as a function of the excitation wavelength. The resonant Raman profiles are shown in Fig. 6.1. The TO phonon is due to deformation potential interaction. Its resonant Raman profile shows only an ingoing resonance [31, 68]. The resonance maximum is at 1.425 eV, exactly at the value of bulk GaAs. The LO phonon mode exhibits ingoing and outgoing resonances, due to Fröhlich coupling, at 1.425 eV and 1.46 eV. The separation between ingoing and outgoing resonance is one LO phonon energy (35 meV). This is in excellent agreement with measurement on bulk GaAs [27, 31]. Our measurements show, that the small diameter does not affect the bandgap energy of the wires.

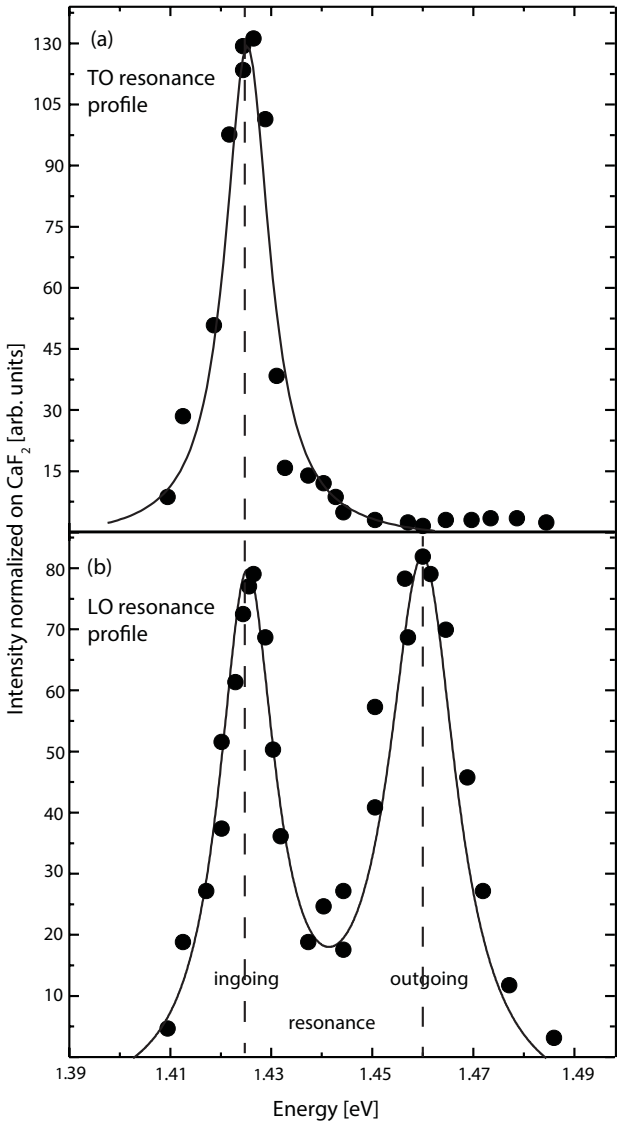

Figure 6.1 Resonant Raman profiles of the TO (upper panel) and LO (lower panel) phonon for zincblende nanowires at room-temperature.

6.2 Resonant Raman Scattering on Wurtzite GaAs Nanowires[1]

In Fig. 6.2 a near resonant Raman spectrum of the single wurtzite GaAs NW is shown with the typical Raman modes for GaAs, a transversal optical (TO) phonon mode at 267 cm^{-1} and a longitudinal optical (LO) phonon mode at 293 cm^{-1}. The frequencies of the phonons are at the bulk position so we exclude strain and confinement effects. We also identify higher-order LO phonon modes in Fig. 6.2, which indicates that the Raman scattering for the LO phonon involves excitonic states [27].

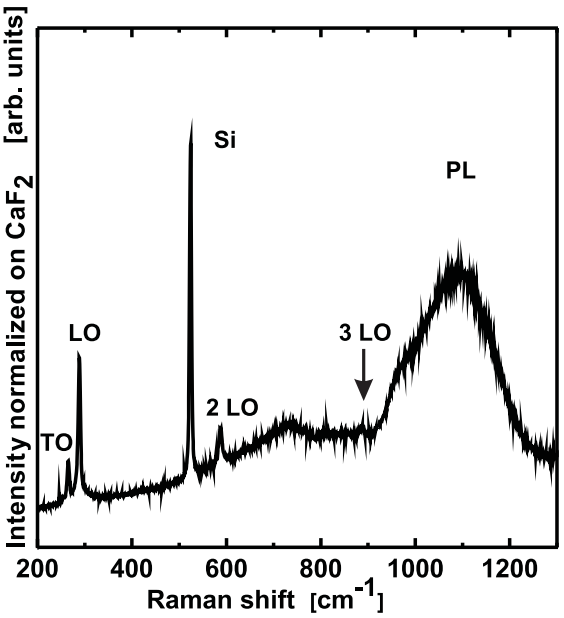

Figure 6.2 Raman spectra of a single WZ GaAs NW with 50 nm diameter and 2.2 μm length at room-temperature at 1.59 eV excitation.

[1]The section is taken from Ref. [74]. I did the measurements and wrote the results and discussion under supervision of S. Breuer, M. Ramsteiner, L. Geelhaar, H. Riechert and S. Reich who co authored the paper

Finally, we observe photoluminescence around 855 nm (1.45 eV). This already points towards the WZ optical gap being larger than the ZB bandgap. To investigate the exact resonance energy, we recorded Raman spectra as a function of excitation energy around 855 nm. In the following, we concentrate on the LO, TO and second-order LO resonance.

In the literature two models for the bandstructure of WZ GaAs nanowires are discussed. The first model shows a splitting of the heavy hole hh (Γ_{9V}) and light hole lh (Γ_{7V}) band, as in Fig. 6.3a [26]. Alternatively discussed are a Γ_{9V} valance band and two conduction bands with Γ_{8C} and Γ_{7C} symmetry [93], see Fig. 6.3b. The transition in Fig. 6.3a between the Γ_{7V} valance band (red arrow) and the

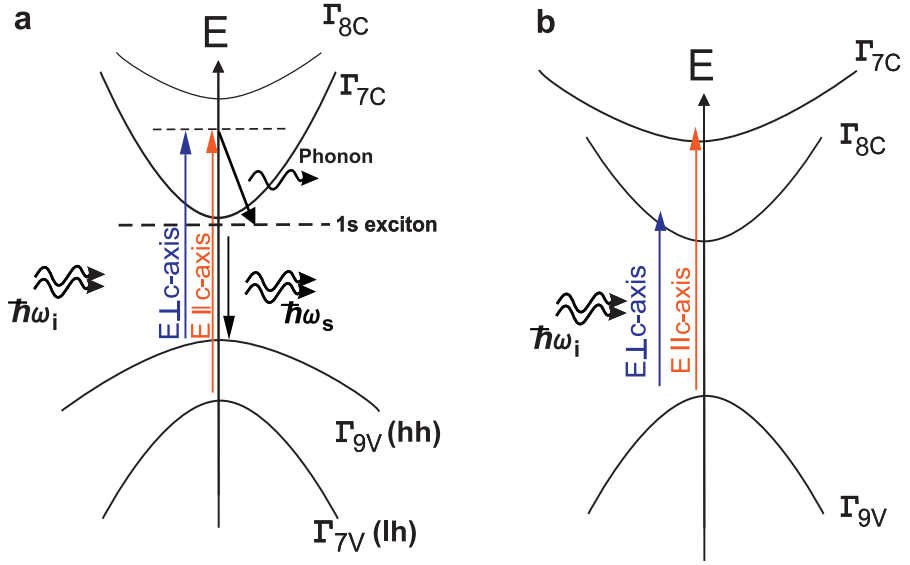

Figure 6.3 Alternative schematic band structure at the Γ point of wurtzite GaAs. (a) The valance bands are formed by the Γ_{9V} heavy hole and the Γ_{7V} light hole states. One of the conduction bands has Γ_{7C} symmetry. The energetic position of the Γ_{8C} conduction band is above the Γ_{7C} conduction band. Optical transitions are allowed for $\Gamma_{9V} \rightarrow \Gamma_{7C}$ under perpendicular and $\Gamma_{7V} \rightarrow \Gamma_{7C}$ under both parallel and perpendicular polarization of the incoming light. (b) The valance band is formed by Γ_{9V} state. the lowest conduction band has Γ_{8C} symmetry.

Γ_{7C} conduction band is allowed for light polarized along and perpendicular to the wire c-axis, the transition between Γ_{9V} valance band and the Γ_{7C} conduction band

(blue arrow in Fig. 6.3a and b) is allowed only for light polarized perpendicular to the wire c-axis [94]. Transition between Γ_{9V} valance band and Γ_{8C} conduction band are allowed only for light polarized perpendicular to the wire axis [94]. The two models differ strongly in the resulting optical selection rules.
In a resonant Raman process the enhancement from the ingoing resonance results when the energy of the incident light matches an allowed optical transition. For outgoing resonance an incoming photon $\hbar\omega_i$ excites an electron to a virtual state (Fig. 6.3a). The state relaxes by inelastic scattering with the lattice. The recombination occurs again between real states and leads then to a Raman scattered photon $\hbar\omega_s$ with a strongly enhanced signal (see Fig. 6.3) [27]. Polarized Raman experiments will allow to distinguish between the band structures and to determine the energetic positions of the bands.

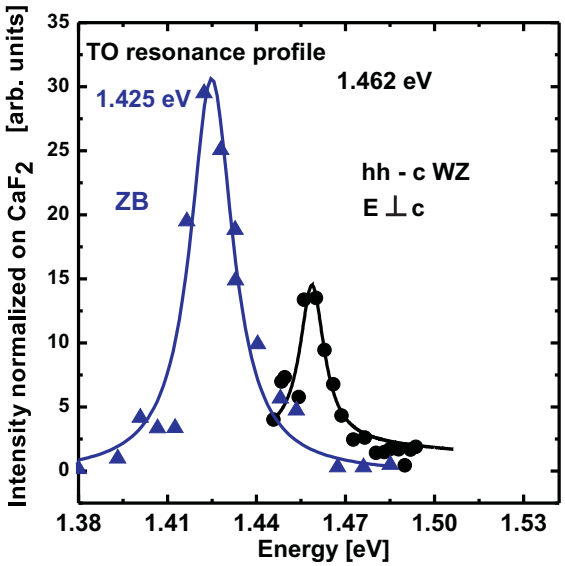

Figure 6.4 Resonant Raman profile of the TO mode from a single wurtzite GaAs nanowire for incident light polarized perpendicular to the NW c-axis (black circles and full line). For comparison the TO resonance profile (blue triangles and full line) for zincblende GaAs NW is shown with light polarized along the wire axis. Both profiles were measured at room temperature.

In Fig. 6.4 we present the resonant Raman intensities of the TO phonon in WZ (circles) and ZB (triangles) GaAs NWs.

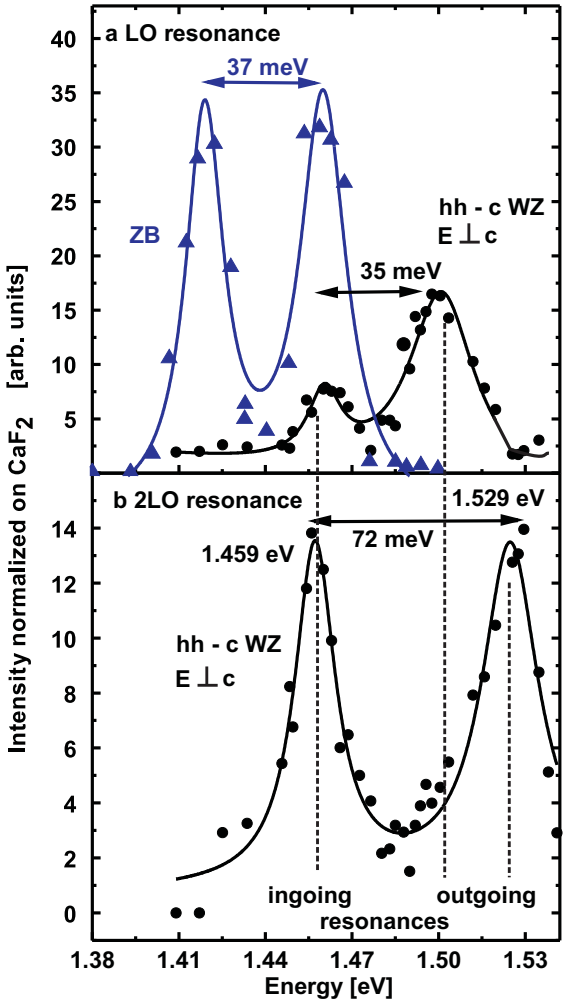

Figure 6.5 a: Resonant Raman profiles of the LO mode (incident light polarized perpendicular to NW c-axis) from a single WZ GaAs NW (black circles and full line) and ZB GaAs reference sample (blue triangles and full line); b: 2 LO resonance profile for incident light polarized perpendicular to the NW c-axis. All profiles were collected at room-temperature.

The TO phonon shows a single, ingoing resonance in ZB GaAs at the gap $E_0^{\mathrm{zb}} = 1.425\,\mathrm{eV}$, due to deformation-potential, which is in excellent agreement with published data. [68] Clearly, the resonance in WZ GaAs is shifted by 35 meV to higher energies. This places $E^{\mathrm{wz}} = 1.462\,\mathrm{eV}$, i.e., higher than in ZB wires. The LO resonance profile for the WZ nanowire (black) and for a ZB reference sample (blue) are displayed in Fig. 6.5a. In contrast to the single resonance of the TO mode, the LO profiles show an ingoing and outgoing resonance with a separation of one LO phonon energy (36 meV, Ref. [68]). Compared to ZB GaAs, the resonances of the WZ GaAs are again blue-shifted by 37 meV. At the ZB GaAs bandgap neither for incident light parallel nor perpendicular to the NW c-axis a resonance maximum occur in the WZ wire.

Fröhlich coupling gives rise to strong multiphonon bands for excitonic resonances, see Fig. 6.2 [68]. Figure 6.5b shows the resonance profile of the second-order LO mode. The separation between ingoing and outgoing resonance is 72 meV, or twice to LO energy, as can be seen in Fig. 6.5b. The ingoing resonance is at 1.459 eV,*i.e.*, the same energy as the LO and close to the TO resonance. The observation of an ingoing and outgoing LO resonance and the TO resonance profile allow us to determine the exact optical gap of WZ GaAs. From the ingoing LO and two LO resonance we estimate an optical bandgap energy of 1.459 eV. The outgoing resonances yield an optical bandgap $E^{WZ} = 1.458\,\mathrm{eV}$. The TO resonance is 1.462 eV directly at the optical bandgap energy, as for ZB GaAs [68]. Combining all these Raman experiments show clearly that the optical WZ bandgap is 1.460eV $\pm$ 3 meV at room-temperature. Moreover the resonances in the range from 1.38 eV to 1.54 eV are strongly polarized perpendicular to the wire axis. They belong to $\Gamma_{9V} \rightarrow \Gamma_{7C}$ or $\Gamma_{9V} \rightarrow \Gamma_{8C}$ transition, see Fig. 6.3. Transitions between Γ_{9V} and Γ_{8C} bands are expected to be very weak [26]. The strong 2LO resonance at 1.46 eV is a clear sign of the $\Gamma_{9V} \rightarrow \Gamma_{7C}$ transition. We also performed Raman experiments with light polarized parallel to the NW c-axis in the energy range between 1.53 and 1.60 eV ($x(z,z)\overline{x}$ configuration). The resonance profiles of the TO and the one and two LO phonon modes in parallel configuration for the wurtzite NW are displayed in Fig. 6.6.

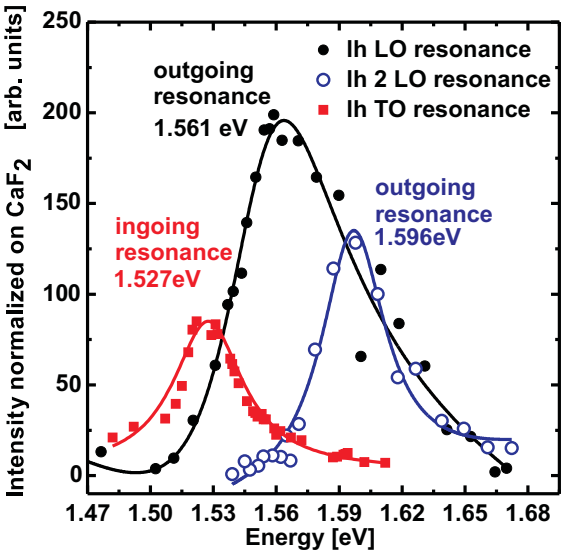

Figure 6.6 lh -c resonance profile from a single WZ GaAs NW at room-temperature for light polarized parallel to the nanowire axis. TO intensity - squares, LO intensity - full circles and 2LO intensity - open circles are reported.

The TO profile shows an ingoing resonance, which is typical for RRS by deformation potential [68]. The LO and 2LO profiles show outgoing resonances, as expected for RRS by Fröhlich coupling [27]. The resonances are strongly polarized parallel to the wire axis, that means that the resonant enhancement of the intensity is now due to the resonant Raman process between Γ_{7C} conduction and Γ_{7V} valance (light hole) band (Fig. 6.3 red arrow) [94]. From the maxima at 1.561eV for the LO phonon, 1.596 eV for the two LO phonon and 1.527 eV for the TO we determine a transition energy $E(\Gamma_{7V} \rightarrow \Gamma_{7C}) = 1.528\,\text{eV} \pm 3\,\text{meV}$. This yields to a splitting between heavy and light hole of $65 \pm 6\,\text{meV}$, much lower then the 103 meV observed by Ketterer *et al.* [26]. Note, however, that the discrepancy is due to the smaller fundamental gap reported in Ref. [26].
From the determined values for $E(\Gamma_9 \rightarrow \Gamma_7)$ and $E(\Gamma_7 \rightarrow \Gamma_7)$ we calculate the crystal field splitting Δ_1. [95].

$$E(\Gamma_{9v}) = E_0 + \Delta_1 + \Delta_2 \tag{6.1}$$

and

$$E(\Gamma_{7v}) = E_0 + \frac{\Delta_1 + \Delta_2}{2} \pm \frac{\sqrt{(\Delta_1 - \Delta_2)^2 + 8\Delta_3^2}}{2}, \tag{6.2}$$

with an average value for the two matrix elements Δ_2 and Δ_3 (required to describe the spin-orbit interaction) of typically 350 meV for wurtzite GaAs. The crystal field splitting energy amounts then to $\Delta_1 \sim 110$ meV. Our calculated value is in excellent agreement with the theoretical prediction $\Delta_1 = 122$ meV by Murayama *et al.* [22]

Our result for the band gap energy of wurtzite GaAs assumes an exciton binding energy (4 meV) as found in zincblende GaAs. The differences in exciton binding between the two crystal structures are expected to be small. Nevertheless, a better knowledge of the excitonic properties of wurtzite GaAs is highly desirable to remove the systematic uncertainty in the reported band gap energies. Note that the heavy-light hole splitting is hardly affected by this uncertainty.

We now compare our resonance profiles and their interpretation to previous work. Peng *et al.* observed a single resonance of the LO phonon at 1.56 eV at room-temperature and under polarization parallel to the wire axis [93]. It corresponds to our resonance profile in Fig. 6.6 with the comparable resonance 1.561 eV for the first-order LO. Ketterer *et al.* [26] found a similar resonance at 1.66 eV; the shift to higher energies is due to the low-temperature (10 K) measurements in Ref. [26]. This resonance was assigned to the $\Gamma_{7V} \rightarrow \Gamma_{7C}$ transition, compare to Fig. 6.3a, in all three studies. We further confirm the $E(\Gamma_{7V} \rightarrow \Gamma_{7C}) = 1.561$ eV transition energy from the 2LO and the TO profile (see Fig. 6.6). Under perpendicular polarization we observe an ingoing and outgoing resonance of the first and second-order LO phonon corresponding to the $\Gamma_{9V} \rightarrow \Gamma_{7C}$ transition at 1.462 eV. In contrast, Ketterer *et al.* [26] found the LO profiles in resonance with ZB transition energies. Unfortunately, they do not show data in the $1.62 - 1.67$ eV energy range where we expect the outgoing WZ $E(\Gamma_{9V} \rightarrow \Gamma_{7C})$ resonance at low-temperatures. The origin of the discrepancy remains unclear. A larger optical gap for WZ GaAs at room-temperature is in excellent agreement with recent luminescence data [19–22]; importantly, cathodoluminescence on similar nanowires found also a larger WZ bandgap [29].

6.3 Influence of Zincblende Insertions on Optical Experiments[2]

Our resonant Raman experiments shows that the bandgap of wurtzite GaAs is 1.46 eV. Still, one question remains: Why there are so many different values for the bandgap of wurtzite GaAs (see Table 1.1)?
An explanation for the varying gap energies in wurtzite GaAs obtained by optical experiments, e.g. photoluminescence and resonant Raman scattering, is the presence of zincblende insertions. Assuming a type-II band alignment, as described by Jahn *et al.* [29] and Spirkoska *et al.* [19] for the WZ/ZB heterostructure, the zincblende insertions form quantum wells in the conduction band. This would lead to the observations of the additional Raman resonances between the zincblende and wurtzite bandgap and various PL transition energies.
In order to investigate the band alignment we combine resonant Raman scattering as well as photoluminescence experiments on a GaAs nanowire that have WZ structure with several ZB insertions. In order to determine the microstructure of the GaAs NWs, the investigation by means of transmission electron microscopy (TEM) was performed on a large number of individual wires. All investigated NWs exhibit similar morphology that is shown on a representative TEM micrographs of a single GaAs nanowires in Fig. 6.7. At the bottom [Figure 6.7(c)] the nanowire have pure wurtzite structure with no or very few isolated stacking faults (SFs). In the middle part [Fig. 6.7(b)] the nanowire have predominantly wurtzite structure, but now zincblende insertions (marked as ZB in the figure) are detected, which consist of nanometer-sized thin segments of zincblende GaAs material. Compared with the bottom part, the number of isolated stacking faults is increased. In the top part [Figure 6.7(a)] we still observe the predominant wurtzite structure, but also a high density of zincblende insertion. The number of zincblende segments is much larger than in the middle part. Additionally some of these segments exhibit twinning and are defective. The extent and the defective condition of the

[2]Parts of the section are taken from Ref. [52], which is submitted and under review in Phys. Rev. B. I did the measurements and write the results and discussion under supervision of E. Grelich, C. Somaschini, E. Luna, M. Ramsteiner, L. Geelhaar, H. Riechert and S. Reich who co authored the paper.

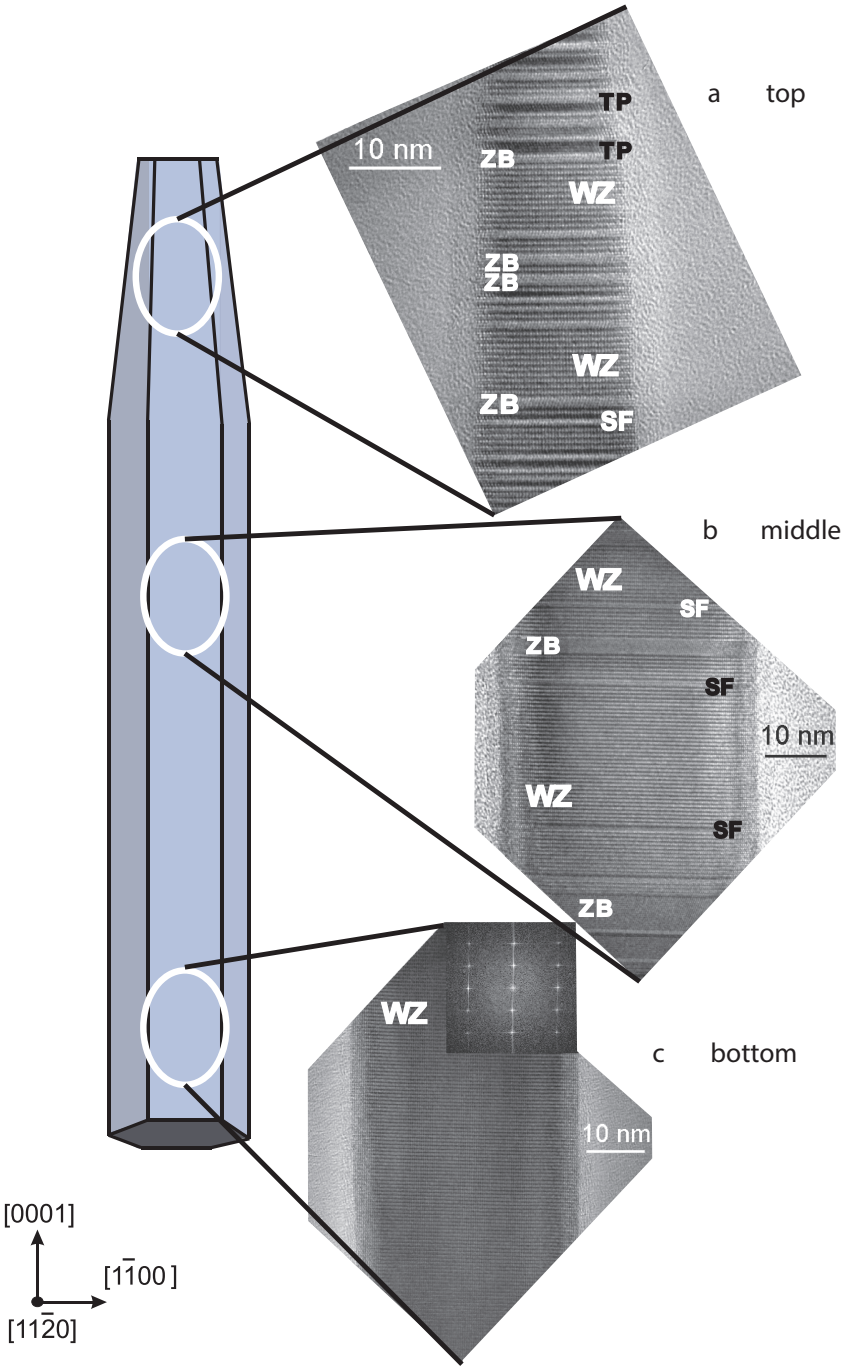

Figure 6.7 TEM images of the top (a), middle (b) and bottom (c) part of single GaAs NWs. ZB marks zincblende segments, SF stacking faults, TP twin planes, WZ marks the predominant wurtzite crystal structure.

zincblende segments at the top part of the nanowire vary slightly from nanowire to nanowire. Due to the different microstructure at the top, middle and bottom part of the nanowire and taking advantage of the high spatial resolution of the Raman scattering technique (about 0.7, μm), we further analyze the properties of all three parts of the NW.

We begin the investigation by position-dependent Raman scattering. Figure 6.8 shows an XY-map of the GaAs LO intensity overlayed with a sketch of the scattering nanowire. The excitation energy is in resonance with the light hole lh ($\Gamma_{7V} \rightarrow \Gamma_{7C}$) transition of wurtzite GaAs ($E(\Gamma_{7V} \rightarrow \Gamma_{7C})$= 1.528 eV) [26, 74]. WZ GaAs has a splitting of the lh and heavy hole hh band at the Γ point of 65 meV shown in Fig. 6.6 [74]. The additional Raman resonance allows us to distinguish between zincblende and wurtzite phases in the wire.

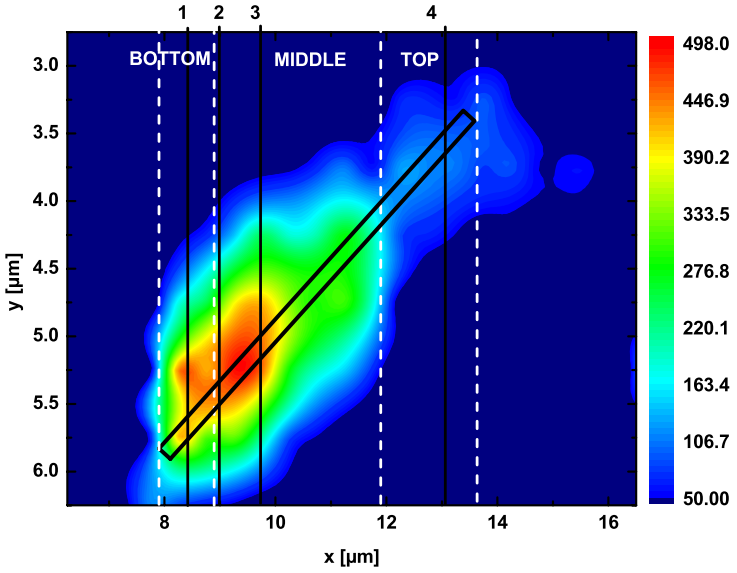

Figure 6.8 Raman map of the LO phonon intensity of a single WZ GaAs NW with 8.5 μm length at room-temperature at 1.59 eV excitation. The square is a sketch of the wire

As can be seen in Fig. 6.8 the bottom and the middle part of the wire have a high Raman intensity corresponding to the wurtzite phase. The low intensity at

the top of the wire shows that the zincblende phase is dominant. From figure 6.8 we extract single Raman spectra (solid lines in Fig. 6.8). The spectra show the Raman peaks, as well as photoluminescence (PL). The combined Raman and PL spectra are shown in Fig. 6.9, recorded at different positions along the axis of a single nanowire. Because of the excitation at a photon energy only 160 meV above the bandgap of zincblende GaAs, the spectra are dominated by broad PL bands with the weaker Raman spectra visible as the superimposed narrow lines. First-order Raman scattering by transversal optical (TO) and longitudinal optical (LO) phonon modes is observed at 267 cm^{-1} and 293 cm^{-1}, respectively. In addition resonant second-order Raman scattering by two zone-center LO phonons (2LO) leads to a line at 585 cm^{-1}.

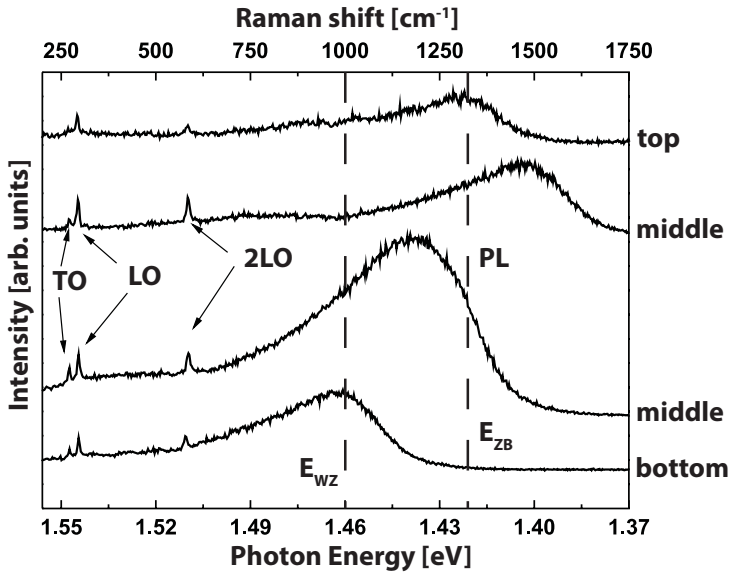

Figure 6.9 Combined PL and Raman spectra recorded at different positions along the growth axis of a GaAs NW for excitation at a photon energy of1.583 eV. The vertical dashed lines indicate the bandgap energies of ZB and WZ GaAs.

The zincblende and wurtzite phase cannot be directly distinguished in the Raman spectra, since the separations between the TO and LO phonon frequencies in both phases are too small to be resolved in the present experiments. Furthermore, the observation of the characteristic E_2 phonon line in wurtzite GaAs is inhibited by the strong dielectric polarization contrast in the range of photon energies used in the present study. [28] Since there is no difference between the measured TO and LO phonon frequencies and those of bulk GaAs, [31] we conclude that the NWs are free of strain. The PL bands are observed at photon energies between 1.40 and 1.46 eV. At the bottom and top of the nanowire, the PL peak energies lie at 1.46 eV and 1.42 eV, respectively (see Fig. 6.9). In these cases very narrow distributions of the PL peak energy are found for excitation at different positions inside the bottom or top region of the nanowire. On the other hand, in the middle part of the nanowire, the PL peak energy depends strongly on the exact position along the nanowire axis.

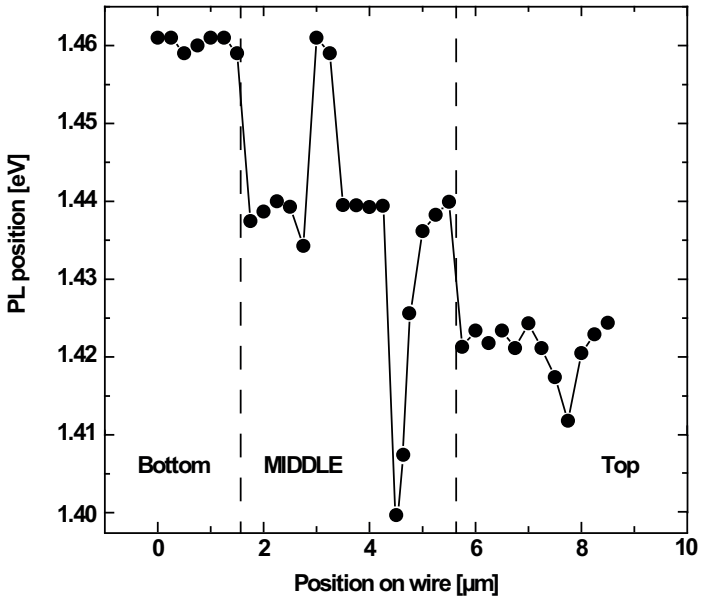

Figure 6.10 PL energy depending on NW position extracted from Fig. 6.8. The label at the axis corresponds to the black lines indicated by markers in Fig. 6.8.

In Fig. 6.9, we show two exemplary spectra from the middle part of the nanowire with PL peak energies at 1.40 and 1.44 eV, corresponding to the observed range of variation. In accordance with our previous work, [74] the PL peak energies at 1.46eV (bottom region) and 1.42 eV (top region) are attributed to band-to-band recombination in zincblende and wurtzite GaAs, respectively. Furthermore, we extract spectra along the entire wire axis (from Fig. 6.8) and estimate the PL peak position dependent of the position on the wire (Fig. 6.10). The changes of the PL peak energy are highlighted again in Fig. 6.10. The sequence of GaAs crystal structures observed in Fig. 6.10 via the PL is in excellent agreement with the TEM images: Regarding the bottom region, our assignment is fully consistent with the TEM analysis (Fig. 6.7) where we have mainly WZ structure and therefore we expect a transition energy of 1.46 eV. The variation of the PL peak energy in a range from below (1.40 eV) to above (1.44eV) in the middle part of the wire can be explained by the capture of electrons in relatively narrow zincblende segments and SFs. The electrons recombine with holes in adjacent wurtzite segments via spatially indirect transitions, [19, 29] in agreement with the structural information obtained by TEM (Fig. 6.7) for the middle part of our nanowires, which leads to the observation of various PL peak energies.

To verify our assignments and to obtain further evidence for the type II band alignment in WZ/ZB heterostructures, we use resonant Raman spectroscopy. The resonance profiles are shown in Fig. 6.11 for different positions along the axis of a single NW. The efficiency of Raman scattering is enhanced when the energy of the incident (incoming resonance) or emitted (outgoing resonance) light matches the energy separation of the valence and conduction band corresponding to an optically allowed direct transition. The resonance profiles for scattering by TO phonons [see Fig. 6.11(a),(c),(e)] exhibit only an incoming resonance maximum which is commonly observed for Raman scattering by the deformation-potential mechanism. [31, 68, 74] The resonance profiles for the LO phonon line [see Fig 6.11(b),(d),(f)], in contrast, reveal both incoming and outgoing resonance enhancements (separated by one LO-phonon energy of 36 meV), as expected for Raman scattering induced by the Fröhlich mechanism. [26, 31, 68, 74]

The resonance profiles from the top part of the NW [Fig. 6.11(a),(b)] exhibit in-

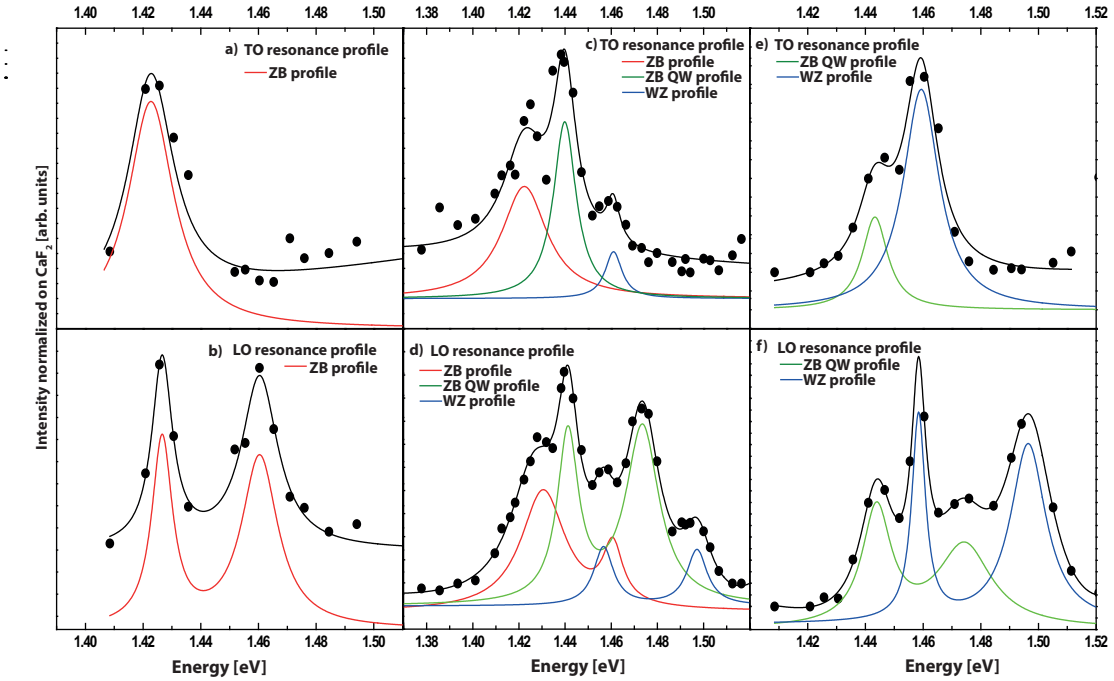

Figure 6.11 Raman intensity as a function of excitation energy for a single GaAs NW recorded at the top (a)-(b), middle (c)-(d), and bottom (e)-(f) part of the NW. The Raman resonance profiles for scattering by TO and LO phonons are shown in the upper and lower panel. The solid lines are shown as a guide to the eye with their colors indicating the the different origins (ZB: wide zincblende segments, WZ: wide wurtzite segments, and ZB QW: thin zincblende segments and/or stacking faults).

coming and outgoing resonance maxima at $1.425 \pm 0.001\,\mathrm{eV}$ (TO and LO) and $1.460\,\mathrm{eV}$ (LO), respectively (see Tab. 6.1). This result can be explained by Raman scattering dominated by the resonance with the fundamental bandgap of ZB GaAs ($E_{ZB} = 1.425\,\mathrm{eV}$), in accordance with our above finding from the PL measurements. The profiles from the bottom of the NW [cf. Fig. 6.11(e),(f)] can be explained by the superposition of resonance enhancements in two different electronic modifications of the NW structure. We assign the stronger component with maxima at $1.459\,\mathrm{eV}$ (incoming: TO and LO) and $1.495\,\mathrm{eV}$ (outgoing: LO) to the fundamental bandgap in wide WZ GaAs segments ($E_{WZ} = 1.460\,\mathrm{eV}$). [74] The weaker component exhibits maxima at $1.443 \pm 0.001\,\mathrm{eV}$ (incoming: TO and LO) and $1.476\,\mathrm{eV}$ (outgoing: LO) and can be explained by Raman scattering in material with an effective bandgap between E_{ZB} and E_{WZ}.

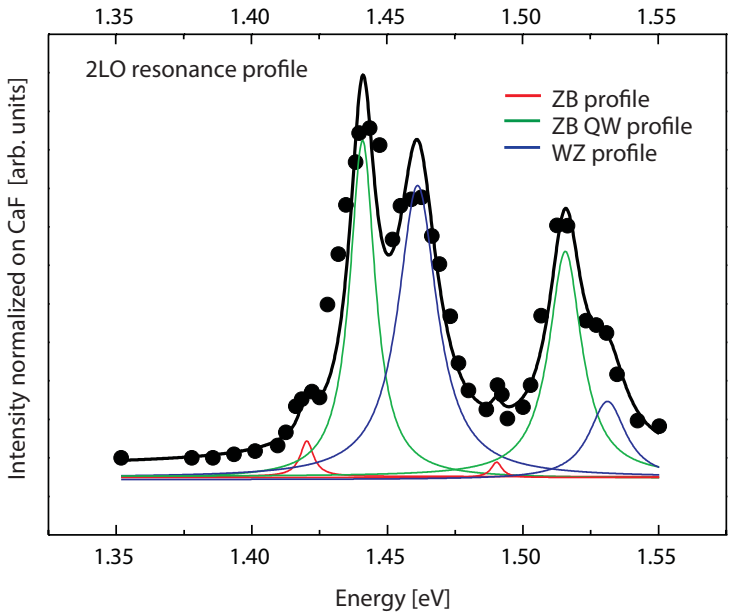

Figure 6.12 2 LO Raman intensity as a function of excitation energy for a single GaAs NW recorded at the middle part of the NW. The solid lines are shown as a guide to the eye with their colors indicating the the different origins (ZB: wide zincblende segments, WZ: wide wurtzite segments, and ZB QW: thin zincblende segments and/or stacking faults).

Additionally, the resonance profile of the 2LO phonon is shown in Fig. 6.12 for the middle part of the wire, which confirm the estimated transition energies from the TO and LO resonance profiles. The measured resonance maxima for ingoing and outgoing resonance are summarized in Tab. 6.1. Resonant Raman measurements on a second position at the middle part of the NW are shown in Fig. 6.13. Again we find resonance maxima at the zincblende (1.425 eV) and wurtzite (1.46 eV) bandgap. Compared with Fig.6.11(c)-(d), now an additional resonance occur at 1.45 eV.

In accordance with the PL results discussed above, we assign the second component in Fig. 6.11(c)-(d) and Fig. 6.13 to narrow ZB segments and/or SFs. The contribution of this component to the PL spectra from the bottom of the NW (see Fig. 6.9) might be suppressed because of the preferential capture of carriers in wider WZ GaAs segments with lower bandgap energy.

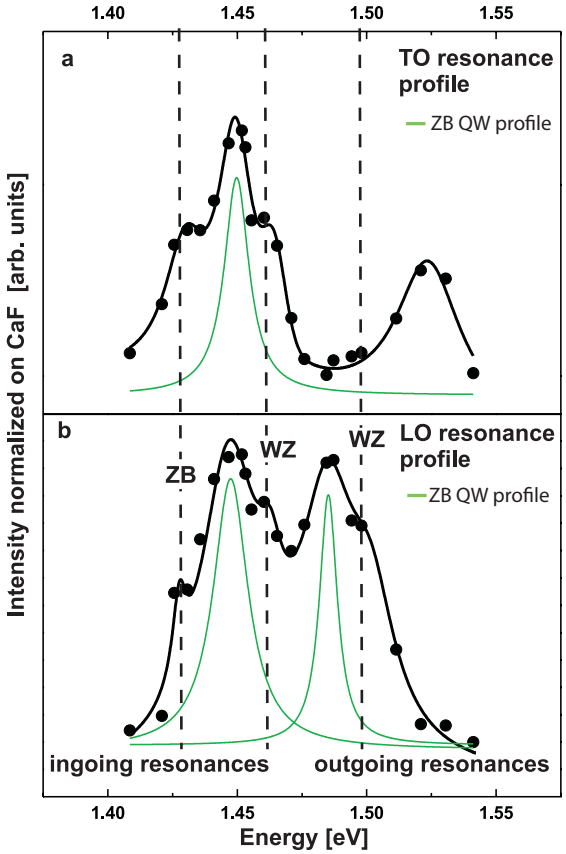

Figure 6.13 Resonant Raman profiles of a single GaAs NW collected at room-temperature at the middle part of the wire. a Resonant Raman profile of the TO mode; b Resonant Raman profile of the LO mode. The position of the zincblende ZB and wurtzite WZ resonances are marked. The green line shows the zincblende insertion resonant Raman profiles.

The resonance profiles from the center of the NW [Fig. 3(c),(d)] can be explained by a superposition of all components observed at the NW's top and bottom with their characteristic energies given in Table 6.1. Here, the contribution of the thin ZB segments and/or SFs is the strongest one, which might be caused by a stronger resonance enhancement induced by electronic confinement. Most importantly, the effective bandgap deduced for thin ZB segments and/or SFs lies always above the fundamental bandgap of ZB GaAs as deduced from several additional resonant Raman profiles recorded at different NW positions. This result contrasts our find-

Table 6.1 Measured Raman resonance energies for TO and LO phonon scattering in wide zincblende (ZB) and wurtzite (WZ) segments as well as thin zincblende segments and/or stacking faults (ZB QW) at different positions along the axis of a GaAs NW. Incoming resonances are observed for both TO and LO phonon scattering, outgoing resonances only for LO phonon scattering.

position	ingoing resonance			outgoing resonance			phonon
on wire	zincblende	wurtzite	ZB QW	zincblende	wurtzite	ZB QW	mode
	1.423 eV	-	-	-	-	-	TO
top	1.426 eV	-	-	1.460 eV	-	-	LO
	1.424 eV	1.459 eV	1.439 eV	-	-	-	TO
middle	1.426 eV	1.458 eV	1.439 eV	1.461 eV	1.494 eV	1.474 eV	LO
	1.423 eV	1.460 eV	1.441 eV	1.495 eV	1.531 eV	1.512 eV	2LO
	-	1.459 eV	1.443 eV	-	-	-	TO
bottom	-	1.459 eV	1.442 eV	-	1.495 eV	1.476 eV	LO

ings from the PL measurements where peak energies below the ZB bandgap can be observed (Fig. 6.9). To understand the different behavior in PL and Raman

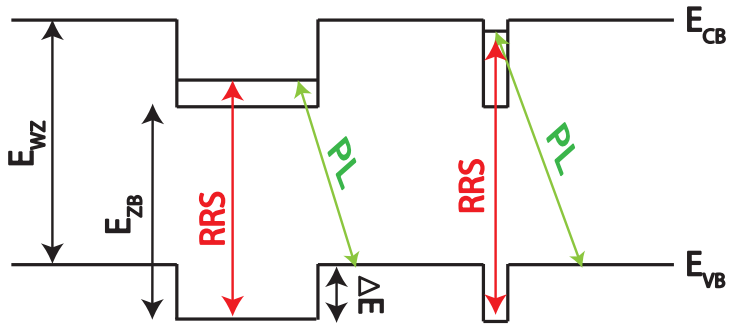

Figure 6.14 Qualitative model for the band-II alignment for ZB insertions in a WZ GaAs nanowire. The red arrow shows direct band to band transitions in a RRS process. The green arrows shows indirect transitions from the ZB insertions to WZ valance band in a PL process.

experiments observed for the local ZB/WZ heterostructure formed by thin ZB segments and SFs in WZ GaAs, we compare the energy ranges of spatially indirect and direct transitions. The corresponding energy diagram is schematically illustrated for a type II band alignment [19, 29]. In this framework SFs are considered

to behave electronically like ultimately narrow ZB segments. [19, 29] For a specific ZB segment or a SF, the energy difference between an indirect PL transition and a direct transition is always given by the energy offset in the valence band (ΔE). The corresponding maximal possible energy ranges for direct and indirect transitions are given by $[E_{ZB}, E_{WZ} + \Delta E]$ and $[E_{ZB} - \Delta E, E_{WZ}]$, respectively. The widths of these energy ranges are determined by the confinement energies in the conduction-band quantum wells (QWs) formed by the ZB segments and SFs (see Fig. 6.14) with the upper (lower) limit approximating the case of SFs (wide ZB segments). The particular peak positions and widths observed in either kind of experiment reflect essentially the distribution of the ZB segment width inside the specific optical probing area. Consequently, the different energy ranges observed for the PL transitions and the Raman resonance maxima are consistent with the type II band alignment proposed previously. [19, 29]

For the sake of completeness one would have to consider in addition the spontaneous-polarization induced electric fields in the local ZB/WZ heterostructures. The most important impact of such finite electric fields would be a downshift of the energy for indirect transitions, [29] but their energy range would still deviate from that of the direct transitions observed by resonant Raman scattering.

Assuming alternatively a type I band alignment, the barrier heights for ZB quantum wells would be very shallow, in the range of about 10 to 30 meV ($E_{WZ} - E_{ZB} = 35$ meV) for both the conduction and valence band. In this case only one confined quantum-well state is expected in both bands and the energy ranges for PL transitions and Raman resonance maxima would be essentially the same, even in the presence of spontaneous-polarization induced electric fields. As a consequence, our combined PL and Raman study provides clear evidence for the type II band alignment in ZB/WZ GaAs heterostructures.

Finally, we compare our resonance profiles and their interpretation to a previous work by Brewster *et al.* [68]. Their 2LO resonance profile showed resonance maxima at 1.425 eV, 1.44 eV, and 1.46 eV very close to this work. The authors suggested an alternative explanation for the resonances based on excitonic resonances and discrete and continuous states. We were able to measure the full TO resonance profile; transversal phonons scatter only by deformation-potential interaction. The TO resonance at 1.44 eV rules out excitonic processes as the origin of this reso-

nance. Our interpretation of a Raman resonance induced by zincblende insertion is further confirmed by the LO profile that shows the same ingoing resonances as 2LO.

7 | Conclusion and Outlook

We investigated the optical gap of wurtzite GaAs nanowires by means of resonant Raman scattering and photoluminescence. From the resonances of the TO, LO and 2LO phonon we determine the optical gap: $E_0^{WZ} = 1.460\,\mathrm{eV} \pm 3\,\mathrm{meV}$ at room-temperature, 35 meV larger than the zincblende band gap. Additionally, the measurements show that the optical gap in wurtzite GaAs is formed by a Γ_9 valance band and a Γ_7 conduction band.
Because in the wurtzite structure the L point is folded onto the Γ point, the conduction band exhibit a splitting into heavy- and light hole band. The energy separation between both bands is 65 meV. For the exact position of the Γ_8 band and thus the exact band gap of wurtzite GaAs non-optical experiments are highly desirable. The resonant Raman scattering on thicker GaAs nanowires confirm the determined optical gap in wurtzite GaAs ($E_0^{WZ} = 1.460\,\mathrm{eV} \pm 3\,\mathrm{meV}$) and the bandstructure described above. The TEM analysis of the second wurtzite nanowires sample shows that the nanowire are at bottom part pure wurtzite and the contribution of the ZB phase increasing towards the top of the nanowires. These is confirmed by position-dependent resonance Raman experiments. Moreover the measurements demonstrate that the wurtzite / zincblende heterostructure forms a type-II band alignment of a predominantly wurtzite type wire. Zincblende insertions forms quantum wells for electrons in the conduction band. The type-II band alignment explains the observation of different transition energies in PL measurements, due to indirect transitions. The experiments show that the possible observable transition energies strongly depend on the width of the zincblende insertion.

The type-II band alignment allows to build new nanowire-based light emitting diodes. The energy of the emitted light could be tuned by varying the width of the zincblende insertion in a wurtzite wire. Additionally, as the zincblende phase forms quantum wells for electrons in the conduction band, nanowires with zincblende insertions could be used for the longtime storage of electrons. Therefore additional Raman and PL experiments on nanowires with well defined zincblende insertion widths, have to be performed.

The zincblende nanowire with a diameter of 50 nm do not follow the Raman selection rules. For that reason polarization-dependent and wavelength-dependent measurements have to be performed with great care. The polarization dependent experiments point out that the highest intensity for the LO and TO phonon appears for incoming and scattered light parallel to the wire axis. This is a result of the one-dimensional geometry of the wire and the dielectric mismatch between wire and environment.

Because the emitted light has a maximum intensity parallel to the wire axis, a further possible application is to use the wires as waveguides for light. For the realization of such devices polarization-dependent Raman scattering has to be performed for wires with different diameters (larger and smaller than 60 nm).

The wavelength dependent Raman experiments demonstrate the quenching of the E_2^h phonon above an excitation wavelength of 600 nm. This is explained by the dielectric polarization contrast for coupling of light into the nanowire axis. This means, that the dielectric polarization contrast have serious effects on light emitting nanowire based devices. Additionally these work show that the combination of Raman, resonant Raman and photoluminescence experiments is an ideal technique to determine the bandgap and allows to investigate the bandstructure of new material semiconductors.

Bibliography

[1] F. Q. dn S. Gradecak, Y. Li, H.-G. Park, Y. Dong, Y. Ding, Z. L. Wang, and C. M. Lieber, "Multi-quantum-well nanowire heterostructures for wavelength-controlled lasers," *Nature Mater.*, vol. 7, p. 701, 2008.

[2] J. Johansson, L. S. Karlsson, C. P. T. Svensson, T. Mrtensson, B. A.Wacaser, K. Deppert, L. Samuelson, and W. Seifert, "Structural properties of (111)B -oriented III-V nanowires," *Nature Mater.*, vol. 5, p. 574, 2006.

[3] M. S. Gudiksen, L. J. Lauhon, J.Wang, D. C. Smith, and C. M. Lieber, "Growth of nanowire superlattice structures for nanoscale photonics and electronics," *Nature*, vol. 415, p. 617, 2002.

[4] Y. Cui and C. M. Lieber, "Functional nanoscale electronic devices assembled using silicon nanowire building blocks," *Science*, vol. 291, p. 851, 2001.

[5] S. Nadj-Pergen, S. Frolov, E. P. A. M. Bakkers, and L. P. Kouwenhoven, "Spin-orbit qubit in a semiconductor nanowire," *Nature*, vol. 7, p. 468, 2010.

[6] M. Tambe, S. Lim, M. Smith, L. Allard, and S. Gradecak, "Realization of defect-free epitaxial core-shell GaAs/AlGaAs nanowire heterostructures," *Appl. Phys. Lett.*, vol. 93, p. 151917, 2008.

[7] C. M. Lieber and Z. L. Wang, "Functional nanowires," *MRS Bulletin*, vol. 32, p. 99, 2007.

[8] R. Agarwal and C. M. Lieber, "Semiconductor nanowires: optics and opto-electronics," *Appl. Phys. A: Mater. Sci. Process*, vol. 85, p. 209, 2006.

[9] C. Thelander, P. Agarwal, S. Brongersma, J. Eymery, L. Feiner, A. Forchel, M. Scheffler, W. Riess, B. Ohlsson, U. Gsele, and L. Samuelson, "Nanowire-based one-dimensional electronics," *Materials Today*, vol. 9, p. 28, 2006.

[10] T. Mimura, S. Hiyamizu, T. Fujii, and K. Nanbu, "A new field-effect transistor with selectively doped GaAs/n-AlxGa1-xAs heterojunctions," *Jpn. J. Appl. Phys*, vol. 19, p. L225, 1980.

[11] K. A. Dick, P. Caroff, J. B. nad M. E. Messing, J. Johansson, K. Deppert, L. R. Wallenberg, and L. Samuelson, "Control of IIIŰV nanowire crystal structure by growth parameter tuning," *Semicond. Sci. Technol.*, vol. 25, p. 024009, 2010.

[12] F. J. Lopez, E. R. Hemesath, and L. J. Lauhon, "Ordered stacking fault arrays in silicon nanowires," *Nano Lett.*, vol. 9, p. 2774, 2009.

[13] A. F. i Morral, J. Arbiol, J. D. Prades, A. Cirera, and J. R.Morante, "Synthesis of silicon nanowires with wurtzite crystalline structure by using standard chemical vapor deposition," *Adv. Mater*, vol. 19, p. 1347, 2007.

[14] P. Caroff, J. Bolionsson, and J. Johansson, "Crystal Phases in III–V Nanowires: From Random Toward Engineered Polytypism," *IEEE J. Sel. Top. Quant. Electron*, vol. 17, pp. 829–846, 2011.

[15] M. Heiss, S. Conesa-Boj, J. Ren, H.-H. Tseng, A. Gali, A. Rudolph, E. Uccelli, F. Peiró, J. Morante, D. Schuh, E. Reiger, E. Kaxiras, J. Arbiol, and A. F. i Morral, "Phonon confinement and plasmon-phonon interaction in nanowire-based quantum wells," *Phys. Rev. B*, vol. 83, p. 045303, 2011.

[16] M. Moewe, L. C. Chuang, S. Crankshaw, C. Chase, and C. Chang-Hasnain, "Atomically sharp catalyst-free wurtzite GaAs? AlGaAs nanoneedles grown on silicon," *Appl. Phys. Lett.*, vol. 93, p. 023116, 2008.

[17] A. De and C. E. Pryor, "Predicted band structures of III-V semiconductors in the wurtzite phase," *Phys. Rev. B*, vol. 81, p. 155210, 2010.

[18] Z. Zanolli, F. Fuchs, J. Furthmüller, U. von Barth, and F. Bechstedt, "Model GW band structure of InAs and GaAs in the wurtzite phase," *Phys. Rev. B*, vol. 75, p. 245121, 2007.

[19] D. Spirkoska, J. Arbiol, A. Gustafsson, S. Conesa-Boj, F. Glas, I. Zardo, M. Heigoldt, M. H. Gass, A. L. Bleloch, S. Estrade, M. Kaniber, J. Rossler, F. Peiro, J. R. Morante, G. Abstreiter, L. Samuelson, and A. F. i Morral, "Structural and optical properties of high quality zinc-blende/wurtzite GaAs nanowire heterostructures," *Phys. Rev. B*, vol. 80, p. 245325, 2009.

[20] T. B. Hoang, A. F. Moses, H. L. Zhou, D. L. Dheeraj, B. O. Fimland, and H. Weman, "Observation of free exciton photoluminescence emission from single wurtzite GaAs nanowires," *Appl. Phys. Lett.*, vol. 94, p. 133105, 2009.

[21] F. Martelli, M. Piccin, G. Bais, F. Jabeen, S. Ambrosini, S. Rubini, and A. Franciosi, "Photoluminescence of Mn-catalyzed GaAs nanowires grown by molecular beam epitaxy," *Nanotechnology.*, vol. 18, p. 125603, 2007.

[22] M. Murayama and T. Nakayama, "Chemical trend of band offsets at wurtzite/zinc-blende heterocrystalline semiconductor interfaces," *Phys. Rev. B*, vol. 49, p. 4710, 1994.

[23] R. Gurwitz, A. Tavor, L. Karpeles, I. Shalish, W. Yi, G. Seryogin, and V. Narayanamurti, "Bandgap and band discontinuity in wurtzite/zincblende GaAs homomaterial heterostructure," *Appl. Phys. Lett.*, vol. 100, p. 191602, 2012.

[24] L. Ahtapodov, J. Todorovic, P. Olk, T. Mjland, P. Slttnes, D. L. Dheeraj, A. T. J. van Helvoort, B.-O. Fimland, and H. Weman, "A story told by a single nanowire: optical properties of wurtzite GaAs," *Nano Lett.*, vol. 12, pp. 6090–6095, 2012.

[25] D. C. Kim, D. L. Dheeraj, B. O. Fimland, and H. Weman, "Polarization dependent photocurrent spectroscopy of single wurtzite GaAs/AlGaAs core-shell nanowires," *Appl. Phys. Lett.*, vol. 102, p. 142107, 2013.

[26] B. Ketterer, M. Heiss, E. Uccelli, J. Arbiol, and A. F. i Morral, "Untangling the electronic band structure of wurtzite GaAs nanowires by resonant Raman spectroscopy," *ACS Nano*, vol. 5, p. 7585, 2011.

[27] M. Cardona and G. Güntherodt, *Light Scattering in Solids II.* Berlin Heidelberg New York: Springer, 1982.

[28] M. Ramsteiner, O. Brandt, P. Kusch, S. Breuer, S. Reich, and l. Geelhaar, "Quenching of the E2 phonon line in the Raman spectra of wurtzite GaAs nanowires caused by the dielectric polarization contrast," *Appl. Phys. Lett.*, vol. 103, p. 043121, 2013.

[29] U. Jahn, J. Lähnemann, C. Pfüller, O. Brandt, S. Breuer, B. Jenichen, M. Ramsteiner, L. Geelhaar, and H. Riechert, "Luminescence of GaAs nanowires consisting of wurtzite and zinc-blende segments," *Phys. Rev. B*, vol. 85, p. 045323, 2012.

[30] A. Belabbes, C. Panse, J. FurthmĺUller, and F. Bechstedt, "Electronic bands of III-V semiconductor polytypes and their alignment," *Phys. Rev. B*, vol. 86, p. 075208, 2012.

[31] P. Yu and M. Cardona, *Fundamentals of Semiconductors.* Berlin Heidelberg New York: Springer, 2005.

[32] M. I.McMahon and R. J. Nelmes, "Observation of a wurtzite form of gallium arsenide," *Phys. Rev. Lett.*, vol. 95, p. 215505, 2005.

[33] W. Martinssen and H. Warlimont, *Springer Handbook of Condensed Matter andMaterials Data.* Berlin: Springer, 2005.

[34] C. Hamaguchi, *Basic Semiconductor Physics.* Berlin, Heidelberg: Springer, 2010.

[35] R. C. Casella, "Toroidal Energy Surfaces in Crystals with Wurtzite Symmetry," *Phys Rev. Lett.*, vol. 5, p. 371, 1960.

[36] L. C. L. Y. Voon, M. Willatzen, M. Cardona, and N. E. Christensen, "Terms linear in k in the band structure of wurtzite-type semiconductors," *Phys. Rev. B*, vol. 53, p. 10703, 1996.

[37] J. L. Birman, "Some Selection Rules for Band-Band Transitions in Wurtzite Structure," *Phys. Rev.*, vol. 114, p. 1490, 1959.

[38] J. J. Hopfield, "Exciton States and Band Structure in CdS and CdSe," *J. Appl. Phys.*, vol. 32, p. 2277, 1961.

[39] S. L. Adler, "Theory of the Valence Band Splittings at k=0 in Zinc-Blende and Wurtzite Structures," *Phys. Rev.*, vol. 126, p. 118, 1962.

[40] K. Hümmer, R. Helbig, and M. Baumgärtner, "Manifestation of k-linear term effects on the Zeeman splitting of the A1-exciton emission lines in ZnO," *Phys Status Solidi B*, vol. 86, p. 527, 1978.

[41] I. Broser and M. Rosenzweig, "A quantitative study of excitonic polariton reflectance in CdS II. B-exciton and ?-linear term," *Phys Status Solidi B*, vol. 95, p. 141, 1979.

[42] E. S. Koteles and G.Winterling, "Direct Measurement of Three-Branch Exciton-Polariton Dispersion in CdS," *Phys Rev. Lett.*, vol. 44, p. 948, 1980.

[43] I. Vurgaftman, J. R.Meyer, and L. R. Ram-Mohan, "Band parameters for iii-v compound semiconductors and their alloys," *J. Appl. Phys.*, vol. 89, p. 5815, 2001.

[44] S. L. Chuang and C. S. Chang, "kp method for strained wurtzite semiconductors," *Phys. Rev. B*, vol. 54, p. 2491, 1996.

[45] J. L. Birman, "Polarization of Fluorescence in CdS and ZnS Single Crystals," *Phys. Rev. Lett*, vol. 2, p. 157, 1959.

[46] A. Einstein, "Emission and absorption of radiation in the quantum theory (in German)," *Verh. Dtsch. Phys. Ges.*, vol. 18, pp. 318–323, 1916.

[47] A. Einstein, "The quantum theory of radiation (in German)," *Phys. Z*, vol. 18, pp. 121–128, 1917.

[48] P. Y. Yu and b. Welber, "High pressure photoluminescence and resonance Raman studies of GaAs.," *Solid State Commun.*, vol. 25, pp. 209–211, 1978.

[49] M. Grundmann, *The Physics of Semiconductors*. Berlin Heidelberg New York: Springer, 2006.

[50] M. Eickhoff, "Gepulste optisch detektierte NMR in GaAs/AlGaAs Quantentĺopfen," dissertation, Universitt Dortmund, 2003.

[51] J. H. Davies, "The physics of low-dimensional semiconductors," *Cambridge University Press*, 1989.

[52] P. Kusch, E. Grelich, C. Somaschini, E. Luna, M. Ramsteiner, L. Geelhaar, H. Riechert, and S. Reich, "Type II band alignment of zincblende and wurtzite segments in GaAs nanowires: a combined photoluminescence and resonant Raman scattering study," *Phys. Rev. B*, vol. 89, p. 045310, 2014.

[53] S. Hunklinger, *Festkrperphysik*. Mnchen Wien: Oldebbourg, 2007.

[54] N. W. Ashcroft, *LinkSolid State Physics*. New York: Rinehart and Winston, 1981.

[55] I. Zardo, S. Conesa-Boj, F. Peiro, J. R. Morante, J. Arbiol, E. Uccelli, G. Abstreiter, and A. F. i Morral, "Raman spectroscopy of wurtzite and zinc-blende GaAs nanowires: Polarization dependence, selection rules, and strain effects," *Phys. Rev. B.*, vol. 80, p. 245324, 2009.

[56] C. A. Arguello, D. L. Rousseau, and S. P. S. Porto, "First-order raman effect in wurtzite type crystals," *Phys. Rev.*, vol. 181, p. 1351, 1969.

[57] C. Raman and K. Krishnan, "A New Type of Secondary Radiation," *Nature*, vol. 121, p. 501, 1928.

[58] C. Raman, "Change of wave-length in light scattering," *Nature*, vol. 121, p. 619, 1928.

[59] H. M. J. Smith, "The Theory of the vibration and the Raman spectrum of the diamond lattice," *Phil. Trans.*, vol. A241, pp. 1105–145, 1948.

[60] W. Richter, *Resonant Raman scattering in semiconductors" in Solid-State Physics*. Berlin Heidelberg: Springer, 1976.

[61] R. Loudon, "The Raman effect in crystals," *Adv. Phys.*, vol. 14, p. 621, 1965.

[62] G. L. Bir and G. E. Pikus, "Effect of deformation on the energy spectrum and electrical properties of semiconductors of the insb type," *Sov. Phys. Solid State*, vol. 2, p. 2039, 1961.

[63] R. Trommer and M. Cardona, "Resonant Raman Scattering in GaAs," *Phys. Rev. B*, vol. 17, p. 1865, 1978.

[64] W. Kauschke and M. Cardona, "Resonant Raman scattering in semiconductors," *Phys. Scr.*., vol. 1989, p. 201, 1989.

[65] W. Heitler, *The Quantum Theory of Radiation*. Oxford: Oxford Univ. Press, 1954.

[66] R. C. C. Leite, J. F. Scott, , and T. C. Damen, "Multiple-phonon resonant Raman scattering in Cds," *Phys. Rev. Lett.*, vol. 22, p. 780, 1969.

[67] A. Garciá-Cristóbal, A. Cantarero, C. Trallero-Giner, and M. Cardona, "Excitonic model for second-order resonant Raman scattering," *Phys. Rev. B*, vol. 49, p. 13430, 1994.

[68] M. Brewster, O. Schimek, S. Reich, and S. Gradecak, "Exciton-phonon coupling in individual GaAs nanowires studied using resonant Raman spectroscopy," *Phys. Rev. B*, vol. 80, p. 201314, 2009.

[69] B. Ketterer, "Raman Spectroscopy of GaAs Nanowires: Doping Mechanisms and Fundamental Properties," dissertation, ECOLE POLYTECHNIQUE FEDERALE DE LAUSANNE, 2011.

[70] B. Ketterer, "Molecular Beam Epitaxy of GaAs Nanowires and their Suitability for Optoelectronic Applications," dissertation, Humboldt Universität, Berlin, 2011.

[71] A. F. i Morral, C. Colombo, J. Arbiol, J. R. Morante, and G. Abstreiter, "Nucleation mechanism of gallium-assisted molecular beam epitaxy growth of gallium arsenide nanowires," *Appl. Phys. Lett.*, vol. 92, p. 063112, 2004.

[72] S. Breuer, C. Pfüller, T. Flissikowski, O. Brandt, H. T. Grahn, L. Geelhaar, and H. Riechert, "Suitability of Au-and self-assisted GaAs nanowires for optoelectronic applications," *Nano Lett.*, vol. 11, pp. 1276–1279, 2011.

[73] S. Breuer, M. Hilse, A. Trampert, L. Geelhaar, and H. Riechert, "Vapor-liquid-solid nucleation of GaAs on Si (111): Growth evolution from traces to nanowires," *Phys. Rev. B*, vol. 82, p. 075406, 2010.

[74] P. Kusch, S. Breuer, M. Ramsteiner, L. Geelhaar, H. Riechert, and S. Reich, "Band gap of wurtzite GaAs: A resonant Raman study," *Phys. Rev. B*, vol. 86, p. 075317, 2012.

[75] P. A. F. nad A. E. Hill, C. W. Peters, and G. Weinreich, "Generation of Optical Harmonics," *Phys. Rev. Lett.*, vol. 7, p. 118, 1961.

[76] J. Wang, M. Gudiksen, X. Duan, Y. Cui, and C. Lieber, "Highly polarized photoluminescence and photodetection from single indium phosphide nanowires," *Science*, vol. 293, p. 1455, 2001.

[77] L. Y.Cao, L. Laim, P. D. Valenzuela, B. Nabet, and J. E. Spanier, "On the Raman scattering from semiconducting nanowires," *J. Raman Spectrosc.*, vol. 38, p. 697, 2007.

[78] T. Livneh, J. P. Zhang, G. S. Cheng, and Moskovits, "Polarized Raman scattering from single GaN nanowires," *Phys. Rev. B*, vol. 74, p. 1098, 2006.

[79] D. Papadimitriou and A. G. Nassiopoulou, "Polarized Raman and photoluminescence study on silicon quantum wires," *J. Appl. Phys.*, vol. 84, p. 1059, 1998.

[80] P. J. Pauzauskie, D. Talaga, K. Seo, P. D. Yang, and F. Lagugne-Labarthet, "Polarized Raman confocal microscopy of single gallium nitride nanowires," *JA. C.S*, vol. 127, p. 17146, 2005.

[81] G. S. D. and.I. Loa, M. Burghard, K. Syassen, and S. Roth, "Polarized Raman Spectroscopy on Isolated Single-Wall Carbon Nanotubes," *Phys. Rev. Lett.*, vol. 85, p. 5437, 2000.

[82] J. Fréchette and C. Carraro, "Diameter-dependent modulation and polarization anisotropy in Raman scattering from individual nanowires," *Phys. Rev. B*, vol. 74, p. 2161404, 2006.

[83] L. Y.Cao, B. Nabet, and J. E. Spanier, "Enhanced Raman scattering from individual semiconductor nanocones and nanowires," *Phys. Rev. Lett.*, vol. 96, p. 157402, 2006.

[84] Q. Xiong, G. Chen, H. R. Gutierrex, and P. Eklund, "Raman scattering studies of individual polar semiconducting nanowires: phonon splitting and antenna effects," *Appl. Phys. Lett.*, vol. 85, p. 299, 2006.

[85] J. Wu, D. Zhang, Q. Lu, H. R. Gutierrez, and P. Eklund, "Polarized Raman scattering from single GaP nanowires," *Phys. Rev. B*, vol. 81, p. 165415, 2010.

[86] T. Li, L. Gao, W. Lei, L. Guo, T. Yang, Y. Cheng, and Z. Wang, "Raman study on zinc-blende single InAs nanowire grown on Si (111) substrate," *Nanoscale Research Letters*, vol. 8, p. 27, 2013.

[87] H. Harima, "Properties of GaN and related compounds studied by means of Raman scattering," *J. Phys.: Condens. Matter*, vol. 14, p. R967, 2002.

[88] R. Ruppin, "Extinction by a circular cylinder in an absorbing medium," *Opt. Commun.*, vol. 211, p. 335, 2002.

[89] J. Giblin, V. Protasenko, and M. Kuno, "Wavelength sensitivity of single nanowire excitation polarization anisotropies explained through a generalized treatment of their linear absorption," *ACS Nano.*, vol. 3, p. 1979, 2009.

[90] C. Pfüller, M. Ramsteiner, O. Brandt, F. Grosse, A. Rathsfeld, G. Schmidt, L. Geelhaar, and H. Riechert, "Raman spectroscopy as a probe for the coupling of light into ensembles of sub-wavelength-sized nanowires," *Appl. Phys. Lett.*, vol. 101, p. 083104, 2012.

[91] S. Lazić, E. Gallardo, J. Calleja, F. Agulló-Rueda, J. Grandal, M. Sánchez-Garcia, E. Calleja, E. Luna, and A. Trampert, "Phonon-plasmon coupling in electron surface accumulation layers in InN nanocolumns," *Phys. Rev. B*, vol. 76, p. 205319, 2007.

[92] T. C. Damen and J. F. Scott, "Antiresonance of Raman cross-sections for nonpolar phonons in CdS," *Solid State Commun.*, vol. 9, p. 383, 1971.

[93] W. Peng, F. Jabeen, B. Jusserand, J. C. Harmand, , and M. Bernard, "Conduction band structure in wurtzite GaAs nanowires: A resonant Raman scattering study," *Appl. Phys. Lett.*, vol. 100, p. 073102, 2012.

[94] P. Tronc, Y. E. Kitaev, G. Wang, M. F. Limonov, A. G. Panfilov, and G. Neu, "Optical Selection Rules for Hexagonal GaN," *Phys. Status Solidi B*, vol. 216, p. 599, 1999.

[95] B. Gil, O. Briot, and R.-L. Aulombard, "Valence-band physics and the optical properties of GaN epilayers grown onto sapphire with wurtzite symmetry," *Phys. Rev. B*, vol. 52, p. 17028, 1995.

Acknowledgements

I thank Prof. Dr. Reich for the opportunity of working in her group and to write this dissertation. It is great to work with Prof. Dr. Reich. She allowed me to find my own way and whenever it is necessary she pointed me in the right direction. It was and is me a pleasure to work in her group.

Thank you to Prof. Dr. Riechert from the Paul-Drude-Institut and the members of the institute for growing and providing the nanowires, especially Dr. Geelhaar, the Head of Department epitaxy for providing nanowires, Dr. Breuer and Somaschini for nanowire growth and explanation concerning the synthesis, Dr. Ramsteiner for helpful discussions and different explanations, Dr. Luna for TEM measurements and Mrs. Bluhm for providing SEM images.

I wish to thank Prof. Dr. Franke for being the second supervisor.

I would like to thank Dr. A Setaro, Dr. I. Firkowska and J. Kavalakkatt for proof-reading.

I thank my group for the support, the scientific discussion and the good working atmosphere. Moreover for the nice conversations during coffee, beer or cigarette brakes.

Last but not least I thank my family: my parents, my brother and my grandparents for their support, but especially my wife Katarzyna and my children Marco and Emilia. You motivate me to write this dissertation.